Universität Stuttgart

Institut für Wasser- und Umweltsystemmodellierung

Mitteilungen

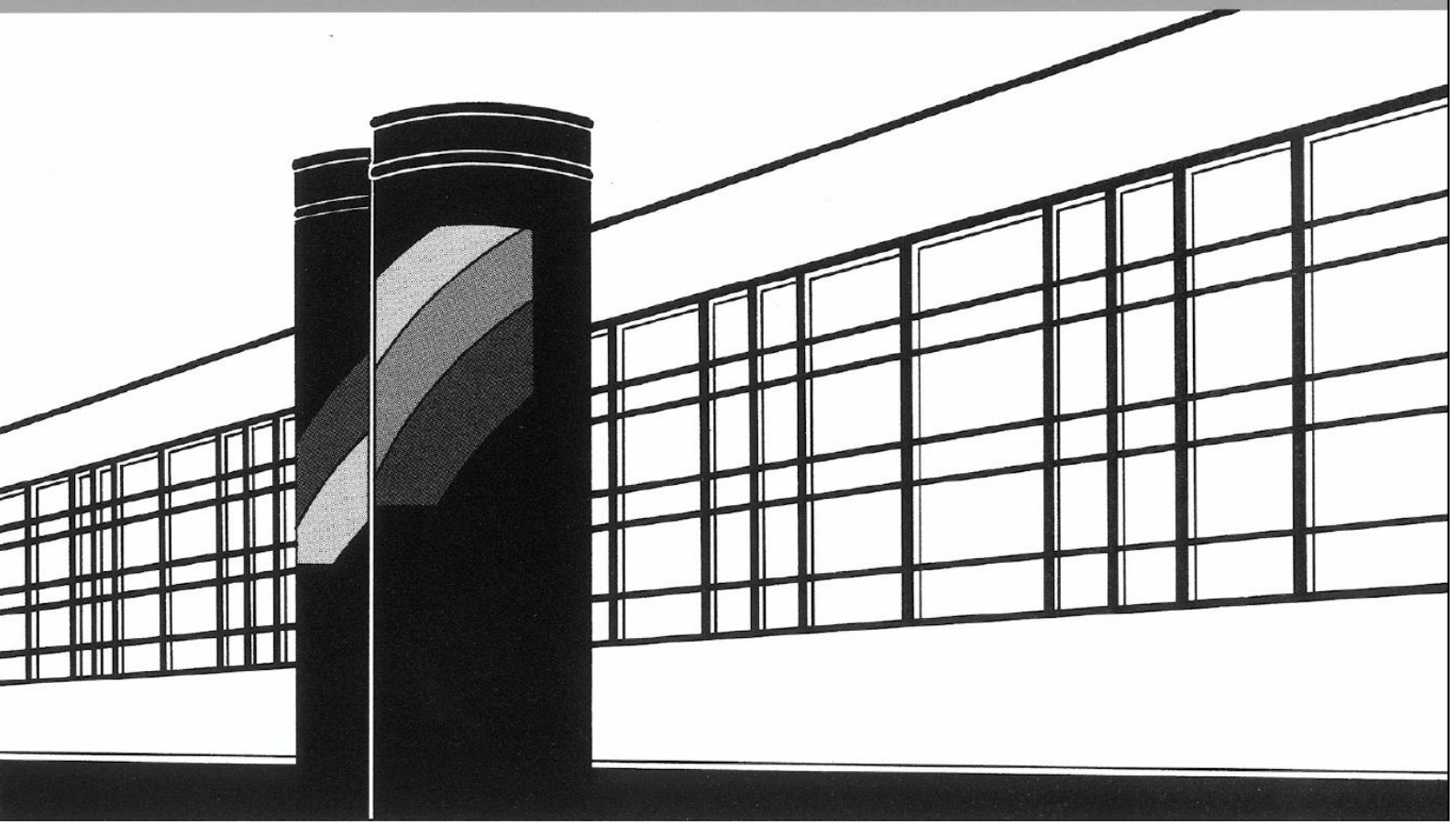

Heft 297 Felix Weinhardt

Porosity and permeability alterations in processes of biomineralization in porous media - microfluidic investigations and their interpretation

Porosity and permeability alterations in processes of biomineralization in porous media - microfluidic investigations and their interpretation

von der Fakultät Bau- und Umweltingenieurwissenschaften
der Universität Stuttgart und dem Stuttgart Center for Simulation Science
zur Erlangung der Würde eines
Doktor-Ingenieurs (Dr.-Ing.) genehmigte Abhandlung

vorgelegt von
Felix Weinhardt
aus Bad Neustadt an der Saale, Deutschland

Hauptberichter:	apl. Prof. Dr.-Ing. Holger Class
Mitberichter:	Prof. Dr. Robin Gerlach
	Prof. Dr.-Ing Holger Steeb
	Prof. Dr. Johan Alexander Huisman

Tag der mündlichen Prüfung: 07. Juli 2022

Institut für Wasser- und Umweltsystemmodellierung
der Universität Stuttgart
2022

Heft 297

Porosity and permeability alterations in processes of biomineralization in porous media - microfluidic investigations and their interpretation

von
Dr.-Ing.
Felix Weinhardt

Eigenverlag des Instituts für Wasser- und Umweltsystemmodellierung
der Universität Stuttgart

D93 Porosity and permeability alterations in processes of biomineralization in porous media - microfluidic investigations and their interpretation

Bibliografische Information der Deutschen Nationalbibliothek
Die Deutsche Nationalbibliothek verzeichnet diese Publikation in der Deutschen Nationalbibliografie; detaillierte bibliografische Daten sind im Internet über http://www.d-nb.de abrufbar

Weinhardt, Felix:
Porosity and permeability alterations in processes of biomineralization in porous media - microfluidic investigations and their interpretation, Universität Stuttgart. - Stuttgart: Institut für Wasser- und Umweltsystemmodellierung, 2022

(Mitteilungen Institut für Wasser- und Umweltsystemmodellierung, Universität Stuttgart: H. 297)
Zugl.: Stuttgart, Univ., Diss., 2022
ISBN 978-3-910293-01-4
NE: Institut für Wasser- und Umweltsystemmodellierung <Stuttgart>: Mitteilungen

Herausgegeben 2022 vom Eigenverlag des Instituts für Wasser- und Umweltsystem-modellierung

Druck: DCC Kästl e.K., Ostfildern

Danksagung

Zu allererst möchte ich mich bei meiner Frau Ezgi, meiner ganzen Familie und meinen Freundinnen und Freunden für die permanente Unterstützung während der letzten Jahre bedanken. Sie haben mich vor allem in den „Durststrecken“ immer wieder motiviert und mir vor allem klargemacht, dass es neben der Promotion auch noch andere spannende Dinge im Leben gibt.

Außerdem geht ein ganz besonderes Dankeschön an meinen Betreuer Holger Class, der mich bereits seit meiner Bachelorarbeit kennt und fördert. Sein immer offenes Ohr, seine fachliche Expertise, sein Blick für das Wesentliche und seine gelassene Art haben mich von Anfang an motiviert und vor allem inspiriert. Unter seiner Betreuung habe ich mich von Anfang an sehr wohl und geschätzt gefühlt, was sicher ausschlaggebend für meine fachliche und persönliche Entwicklung war und immer noch ist. Seine Betreuung war wirklich außergewöhnlich, VIELEN DANK!

Bei Robin Gerlach möchte ich mich für die immer wieder spannenden Diskussionen und Input aus einem anderen Blickwinkel bedanken. Außerdem möchte ich auch seinem ganzen Team für die spannende Zeit in Bozeman an der Montana State University bedanken. Dort habe ich sehr viel Fachliches gelernt, aber auch die wunderschöne Natur genießen können.

Ebenso möchte ich mich bei Holger Steeb für die stete Unterstützung und ergiebigen Gespräche über experimentelle Aufbauten etc. bedanken und natürlich dafür, dass ich im Porous Media Lab arbeiten und es auch mitgestalten durfte! Bei Sander Huisman bedanke ich mich ebenfalls für viele stets spannende Diskussionen während verschiedener Projektmeetings und vor allem dafür, dass er relativ kurzfristig noch als Mitberichter eingesprungen ist.

Herrn Garracht möchte ich für den Prüfungsvorsitz danken und dafür, dass die Atmosphäre während der mündlichen Prüfung den Umständen entsprechend sehr entspannt und angenehm war! Rainer Helmig und Bernd Flemisch waren zwar nicht Teil meines Prüfungsausschusses, aber neben Holger Class, meine beiden weiteren Chefs am LH2. Auch ihnen beiden möchte ich herzlich für die wertvolle Zeit am LH2 danken und vor allem dafür, dass sie mit ihrer Art immer für gute Stimmung und ein konstruktives kollegiales Miteinander im Kollegium sorgen – das ist nicht selbstverständlich und ich weiß es sehr zu schätzen!

Moreover, I would like to thank all my colleagues, including the secretaries, the IT support, the colleagues in the IWS-workshop and of course the colleagues at LH2 for the very nice

and really supporting atmosphere which I really appreciated! Außerdem möchte ich mich nochmal besonders bei Farid für die regelmäßigen Jogging Sessions bedanken. Diese waren der perfekte Ausgleich, vor allem dann, wenn mal im Labor nicht alles so lief wie geplant. Viel Zeit habe ich natürlich auch mit meinem Bürokollegen Johannes Hommel verbracht, der nicht nur beim Thema Biomineralisierung mein erster Ansprechpartner war, sondern z.B. auch in Sachen Gärtnern immer einen guten Rat hatte! Vielen Dank für die tolle Zeit im Büro!

Last but not least I would like to thank also my colleagues at MIB, especially the PML-Crew, which really helped me with the experimental work, and to have fun in the lab. Special thanks goes to Nikos who taught me in the beginning how to ”handle” the lab!

Außerdem danke ich allen Studierenden, die in Form einer Abschlussarbeit und/oder als studentische Mitarbeitende mich bei meiner Arbeit unterstützt haben. Nicht nur ihre Ergebnisse waren äußerst hilfreich, sondern vor allem auch der Teamgeist – den fand ich immer besonders motivierend. Denn zusammen an einem Projekt zu arbeiten, ist immer spannender und meist auch ergiebiger!

Am Schluss möchte ich mich noch bei allen Mitarbeitenden des SFB1313 bedanken. Er bietet ein ausgezeichnetes interdisziplinäres Umfeld. Es hat echt Spaß gemacht, ein Teil davon gewesen zu sein und immer noch sein zu dürfen. Damit geht auch an die DFG für die Finanzierung des SFB's und somit auch meines Teilprojekts ein großer Dank! Alles in allem werde ich immer sehr positiv auf die Zeit meiner Promotion zurückblicken – dies liegt vor allem an den Menschen, mit denen ich zusammenarbeiten durfte. Vielen Dank Euch allen!

Contents

List of Figures

List of Tables

Nomenclature

Selected Acronyms

ACC amorphous calcium carbonate

Da Dahmköhler number

EICP enzymatically induced calcium carbonate precipitation

MICP microbially induced calcium carbonate precipitation

Pe Péclet number

PIV particle image velocimetry

Re Reynold's Number

REV representative elementary volume

XRCT X-ray computed tomography

Greek Letters

μ	dynamic viscosity	[Pa s]
ν	kinematic viscosity	[m^2/s]
ϕ	porosity	[−]
Φ_s	sphericity	[−]

ρ	density	$[\mathrm{kg/m^3}]$

Roman Letters

$\mathbf{g}$	gravitational acceleration	$[\mathrm{m/s^2}]$
D	diffusion coefficient	$[\mathrm{m^2/s}]$
D_p	characteristic pore diameter	$[\mathrm{m}]$
k / $\mathbf{k}$	intrinsic permeability (scalar / tensor)	$[\mathrm{m^2}]$
K_eq	equilibrium constant	unit depends on the reaction
K_m	Michaelis-Menten constant	$[\mathrm{mol/L}]$
k_r	reaction rate coefficient	unit depends on the reaction
K_sp	solubility product	unit depends on the reaction
L	characteristic length	$[\mathrm{m}]$
p	pressure	$[\mathrm{Pa}]$
Q	flow rate	$[\mathrm{m^3/s}]$
Q_r	reaction quotient	unit depends on the reaction
r	reaction rate	$[\mathrm{mol/(L\,s)}]$
r_p	pore radius	$[\mathrm{m}]$
T	temperature	$[\mathrm{K}]$
V	volume	$[\mathrm{m^3}]$
v / $\mathbf{v}$	velocity (scalar / vector)	$[\mathrm{m/s}]$

Abstract

Motivation: Biomineralization refers to microbially induced processes resulting in mineral formations. In addition to complex biomineral structures frequently formed by marine organisms, like corals or mussels, microbial activities may also indirectly induce mineralization. A famous example is the formation of stromatolites, which result from biofilm activities that locally alter the chemical and physical properties of the environment in favor of carbonate precipitation. Recently, biomineralization gained attention as an engineering application. Especially with the background of global warming and the objective to reduce CO_2 emissions, biomineralization offers an innovative and sustainable alternative to the usage of conventional Portland cement, whose production currently contributes significantly to global CO_2 emissions. The most widely used method of biomineralization in engineering applications, is ureolytic calcium carbonate precipitation, which relies on the hydrolysis of urea and the subsequent precipitation of calcium carbonate. The hydrolysis of urea at moderate temperatures is relatively slow and therefore needs to be catalyzed by the enzyme urease to be practical for applications. Urease can be extracted from plants, for example from ground jack beans, and the process is consequently referred to as enzyme-induced calcium carbonate precipitation (ECIP). Another method is microbially induced calcium carbonate precipitation (MICP), which uses ureolytic bacteria that produce the enzyme in situ. EICP and MICP applications allow for producing various construction materials, stabilizing soils, or creating hydraulic barriers in the subsurface. The latter can be used, for example, to remediate leakages at the top layer of gas storage reservoirs, or to contain contaminant plumes in aquifers. Especially when remediating leakages in the subsurface, the most crucial parameter to be controlled is its intrinsic permeability.

A valuable tool for predicting and planning field applications is the use of numerical simulation at the scale of representative elementary volumes (REV). For that, the considered domain is subdivided into several REV's, which do not resolve the pore space in detail, but represent it by averaged parameters, such as the porosity and permeability. The porosity describes the

ratio of the pore space to the considered bulk volume, and the permeability quantifies the ease of fluid flow through a porous medium. A change in porosity generally also affects permeability. Therefore, for REV-scale simulations, constitutive relationships are utilized to describe permeability as a function of porosity. There are several porosity-permeability relationships in the literature, such as the Kozeny-Carman relationship, Verma-Pruess, or simple power-law relationships. These constitutive relationships can describe individual states but usually do not include the underlying processes. Different boundary conditions during biomineralization may influence the course of porosity-permeability relationships. However, these relationships have not yet been adequately addressed.

Pore-scale simulations are, in principle, very well suited to investigate pore space changes and their effects on permeability systematically. However, these simulations also rely on simplifications and assumptions. Therefore, it is essential to conduct experimental studies to investigate the complex processes during calcium carbonate precipitation in detail at the pore scale. Recent studies have shown that microfluidic methods are particularly suitable for this purpose. However, previous microfluidic studies have not explicitly addressed the impact of biomineralization on hydraulic effects. Therefore, this work aims to identify relevant phenomena at the pore scale to conclude on the REV-scale parameters, porosity and permeability, and their relationship.

Contributions: This work comprises three publications. First, a suitable microfluidic setup and workflow were developed in Weinhardt et al. [2021a] to study pore space changes and the associated hydraulic effects reliably. This paper illustrated the benefits and insights of combining optical microscopy and micro X-ray computed tomography (micro XRCT) with hydraulic measurements in microfluidic chips. The elaborated workflow allowed for quantitative analysis of the evolution of calcium carbonate precipitates in terms of their size, shape, and spatial distribution. At the same time, their influence on differential pressure could be observed as a measure of flow resistance. Consequently, porosity and permeability changes could be determined. Along with this paper, we published two data sets [Weinhardt et al., 2021b, Vahid Dastjerdi et al., 2021] and set the basis for two other publications.

In the second publication [von Wolff et al., 2021], the simulation results of a pore-scale numerical model, developed by Lars von Wolff, were compared to the experimental data of the first paper [Weinhardt et al., 2021b]. We observed a good agreement between the experimental data and the model results. The numerical studies complemented the experimental

observations in allowing for accurate analysis of crystal growth as a function of local velocity profiles. In particular, we observed that crystal aggregates tend to grow toward the upstream side, where the supply of reaction products is higher than on the downstream side. Crystal growth during biomineralization under continuous inflow is thus strongly dependent on the locally varying velocities in a porous medium.

In the third publication [Weinhardt et al., 2022a], we conducted further microfluidic experiments based on the experimental setup and workflow of the first contribution and published another data set [Weinhardt et al., 2022b]. We used microfluidic cells with a different, more realistic pore structure and investigated the influence of different injection strategies. We found that the development of preferential flow paths during EICP application may depend on the given boundary conditions. Constant inflow rates can lead to the development of preferential flow paths and keep them open. Gradually reduced inflow rates can mitigate this effect. In addition, we concluded that the coexistence of multiple calcium carbonate polymorphs and their transformations could influence the temporal evolution of porosity-permeability relationships.

Zusammenfassung

Motivation: Biomineralisierung bezeichnet den Prozess, bei dem Minerale durch Aktivitäten lebender Organismen gebildet werden. Neben komplexen biomineralischen Strukturen, wie sie beispielsweise von Meeresorganismen wie Korallen oder Muscheln häufig gebildet werden, können mikrobielle Aktivitäten auch zu einer ungerichteten Mineralisierung führen. Dies ist beispielsweise der Fall bei der Bildung von Stromatolithen, bei der die Aktivitäten von Biofilmen lokal die chemischen und physikalischen Eigenschaften zugunsten der Kalkausfällung verändern. Darüber hinaus gewann Biomineralisierung als ingenieurtechnische Anwendung in den letzten Jahren an Bedeutung. Insbesondere vor dem Hintergrund der globalen Erwärmung und der Zielsetzung, die CO_2-Emissionen zu reduzieren, bietet die Biomineralisierung eine innovative und nachhaltige Alternative zu konventionellem Portlandzement, dessen Herstellung derzeit erheblich zu den globalen CO_2-Emissionen beiträgt. Im Hinblick auf ingenieurtechnische Anwendungen ist die am weitesten verbreitete Methode die ureolytische Calciumcarbonatausfällung. Diese beruht auf der Hydrolyse von Harnstoff und der anschließenden Ausfällung von Calciumcarbonat. Die Hydrolyse von Harnstoff bei moderaten Temperaturen ist relativ langsam, kann aber durch das Enzym Urease katalysiert werden, welches z.B. pflanzenbasiert, in Form von gemahlenen Jack-Bohnen hinzugegeben werden kann. Dies wird als enzymatisch induzierte Calciumcarbonatausfällung (ECIP) bezeichnet. Eine weitere Methode ist die mikrobiell induzierte Calciumcarbonatausfällung (MICP), bei der ureolytische Bakterien zum Einsatz kommen, die das Enzym in situ produzieren. EICP und MICP Anwendungen können unter anderem zur Herstellung von verschiedenen Baumaterialien, zur Stabilisierung von Böden, oder zur Verminderung von Strömungen im Untergrund verwendet werden. Letzteres kann z.B. zur Erhöhung der Dichtigkeit der Deckschicht von Gasspeicherreservoirs oder zur Eindämmung von Schadstofffahnen in Grundwasserleitern eingesetzt werden. Insbesondere bei der Sanierung von Leckagen im Untergrund ist der wichtigste zu kontrollierende Parameter die intrinsische Permeabilität.

Ein nützliches Werkzeug zur Vorhersage und Planung von Feldanwendungen ist die numerische Simulation auf der Skala repräsentativer Elementarvolumina (REV). Um effizient großskalige Anwendungen simulieren zu können, wird deshalb die Porenraumgeometrie nicht im Detail aufgelöst, sondern mit über das REV gemittelten Parametern, wie der Porosität und der Permeabilität beschrieben. Die Porosität beschreibt das Verhältnis von Porenraum zum Gesamtvolumen und die Permeabilität ist ein Maß für die Durchlässigkeit eines porösen Mediums und kann somit als Reziprokwert des Fließwiderstands gesehen werden. Eine Veränderung der Porosität bringt im Allgemeinen auch eine Veränderung der Permeabilität mit sich. Deshalb haben sich für REV-skalige Simulationsanwendungen konstitutive Beziehungen bewährt, mit denen die Permeabilität in Abhängigkeit der Porosität beschrieben werden kann. In der Literatur gibt es verschiedene Porositäts-Permeabilitäts-Beziehungen, wie zum Beispiel die Kozeny-Carman Beziehung, Verma-Pruess, oder einfachere Power-Law Beziehungen. Diese konstitutiven Beziehungen können einzelne Zustände beschreiben, jedoch werden in der Regel die zugrundeliegenden Prozesse nicht mit einbezogen. Beispielsweise können unterschiedliche Randbedingungen während der Biomineralisierung den Verlauf von Porositäts-Permeabilitäts-Beziehungen beeinflussen. Diese Zusammenhänge sind jedoch bisher noch nicht ausreichend untersucht worden.

Porenskalige Simulationen eignen sich grundsätzlich sehr gut, um Porenraumveränderungen und deren Auswirkungen auf die Permeabilität systematisch zu untersuchen. Diese Simulationen beruhen jedoch ebenfalls auf Vereinfachungen und Annahmen. Deshalb ist es unerlässlich, experimentelle Untersuchungen durchzuführen, um die komplexen Prozesse während der Calciumcarbonatausfällung im Detail und auf der Porenskala zu untersuchen. Jüngste Studien haben gezeigt, dass die Methoden der Mikrofluidik hierfür besonders geeignet sind. Die Auswirkungen der Biomineralisierung auf die hydraulischen Auswirkungen sind jedoch in den bisherigen Arbeiten nicht ausreichend berücksichtigt worden. Ziel dieser Arbeit ist es deshalb, relevante Phänomene auf der Porenskala zu identifizieren, um daraus Rückschlüsse auf die REV-skaligen Parameter, Porosität und die Permeabilität, und deren Beziehung ziehen zu können.

Beiträge: Diese Arbeit beinhaltet insgesamt drei Publikationen. Zunächst wurden in Weinhardt et al. [2021a] ein geeigneter mikrofluidischer Aufbau und Arbeitsablauf entwickelt, um die Porenraumveränderung und die damit einhergehenden hydraulischen Auswirkungen zuverlässig untersuchen zu können. In diesem Beitrag wurden die Vorteile und Erkenntnisse verdeutlicht, die durch die Kombination von Lichtmikroskopie und mikro-Röntgencomputer-

tomographie (micro XRCT) mit hydraulischen Messungen in mikrofluidischen Chips entstehen. Dies ermöglicht eine quantitative Analyse der Entwicklung von Calciumcarbonatkristallen in Bezug auf ihre Größe, Form, und räumliche Verteilung, während ihr Einfluss auf den Differenzdruck als Maß des Durchströmungswiderstands beobachtet werden kann. Aus diesen Messdaten wiederum können die Porositäts- und Permeabilätsänderung bestimmt werden. Mit diesem Beitrag wurde der Grundstein für die beiden weiteren Publikationen gelegt sowie zwei Datensätze veröffentlicht [Weinhardt et al., 2021b, Vahid Dastjerdi et al., 2021].

In der zweiten Publikation [von Wolff et al., 2021] wurden die Simulationsergebnisse eines porenskaligen numerischen Modells, entwickelt von Lars von Wolff, mit den experimentellen Daten aus dem ersten Beitrag [Weinhardt et al., 2021b] verglichen. Dabei wurde eine gute Übereinstimmung zwischen den experimentellen Daten und den Modellergebnissen festgestellt. Die numerischen Untersuchungen ergänzten die experimentellen Beobachtungen dahingehend, dass sie genaue Analysen des Kristallwachstums in Abhängigkeit von lokalen Geschwindigkeitsprofilen ermöglichen. Insbesondere beobachteten wir, dass die Kristallaggregate tendenziell zur stromaufwärts gelegenen Seite hin wachsen, wo die Versorgung mit Reaktionsprodukten höher ist, als auf der stromabwärts gelegenen Seite. Das Kristallwachstum während der Biomineralisierung unter kontinuierlichem Zufluss ist also stark von den lokal variierenden Geschwindigkeiten in einem porösen Medium abhängig.

Im Rahmen der dritten Publikation [Weinhardt et al., 2022a] wurden weitere mikrofluidische Experimente basierend auf dem experimentellen Aufbau und Arbeitsablauf des ersten Beitrags durchgeführt und ein weiterer Datensatz veröffentlicht [Weinhardt et al., 2022b]. Dafür wurden mikrofluidische Zellen mit einer anderen, realistischeren Porenstruktur verwendet und der Einfluss unterschiedlicher Injektionsstrategien untersucht. Es hat sich herausgestellt, dass die Entwicklung präferentieller Fließwege während der EICP-Anwendung von den vorgegebenen Randbedingungen abhängt. Konstante Zuflussraten können zur Entwicklung von präferentiellen Fließpfaden führen und diese offen halten. Durch eine schrittweise reduzierte Zuflussrate, kann dieser Effekt abgeschwächt werden. Darüber hinaus wurde festgestellt, dass die Koexistenz von mehreren Calciumcarbonatpolymorphen und deren Transformationen die zeitliche Entwicklung der Porositäts-Permeabilitäts Beziehungen beeinflussen können.

1 Introduction

Biomineralization refers to processes that lead to the formation of minerals generated by living organisms [Ahlstrom, 2011]. The agglomeration of multiple crystals to complex structures is typical for biominerals. Complex biomineral structures are primarily known for oceanic organisms such as corals or shells [Meier, 2017]. In such cases organisms produce minerals as part of their metabolism and control the mineralization process. In other cases, microbial activity can induce mineralization by changing local physical and chemical conditions of the environment. In natural environments, popular examples would be the formation of stromatolites. The activity of biofilms locally alkalinizes the environment and consequently causes the dissolved calcium carbonate to precipitate leading to the genesis of these ancient stromatolites. Also in the human body, microbial activity can induce mineralization which potentially leads to severe diseases like infection- or kidney stones [Hobbs et al., 2018, Espinosa-Ortiz et al., 2019]. As demonstrated, the study of biomineralization is a broad field that draws attention to various scientific disciplines. Besides the occurrence in natural environments, one can also use biomineralization for various civil and environmental engineering applications.

Figure 1.1: Naturally occuring biomineralization: a) and b) scleractinians (stony corals) (reprinted from Drake et al. [2020]); c) stromatolites at Hamelin Pool, Western Australia (reprinted from Allen [2016])

1.1 Biomineralization and its engineering applications

With the background of global warming and the overall aim of reducing CO_2 emissions, biomineralization offers the potential to supplement the use of conventional Portland cement, which currently contributes significantly to the global CO_2 emissions [Nething et al., 2020, Andrew, 2019]. For this purpose, ureolysis-induced calcium carbonate precipitation has been extensively studied and proven to be useful for various engineering applications. It relies on the hydrolysis of urea and the subsequent precipitation of calcium carbonate. The resulting overall reaction equation is given in Equation 1.1, while further details are elaborated in Section 2.3.3:

$$CO(NH_2)_2 + 2H_2O + Ca^{2+} \rightleftharpoons 2NH_4^+ + CaCO_3\downarrow \tag{1.1}$$

The hydrolysis of urea ($CO(NH_2)_2$) at moderate temperatures is relatively slow but can be catalyzed by the enzyme urease. One way to achieve targeted precipitation at desired locations is to use the enzyme urease directly, for example, after extracting it from Jack Bean meal. This is referred to as enzymatically induced calcium carbonate precipitation (EICP). Another technique is to rely on microbes expressing the enzyme urease in situ at the desired locations, which we refer to as microbially induced calcium carbonate precipitation (MICP). The term biomineralization in the context of engineering application in this thesis refers to these two techniques. A short overview of possible applications, categorized into *construction material*, *ground improvements*, *environmental remediation* and *hydraulic control* is presented in the following.

Construction material

Very promising applications of ureolytic biomineralization can be found in the construction sector. For example, it has been successfully applied for the fabrication of construction material and reparation of buildings [Wu et al., 2021]. Research on the so-called bio-bricks is, meanwhile, technically relatively mature. The company Biomason, founded in 2016, focuses on bio-brick research and now offers various types of bio-bricks for the construction industry. In addition, more research has been conducted to improve performance like compressive strength, for instance, by adding fiber supplements [Li et al., 2020]. Other researchers focused on rather unconventional methods to improve cost-effectiveness and environmental impact. For example, Lambert and Randall [2019] grew the world's first bio-brick from

human urine instead of chemical urea in order to reduce the production costs [Wu et al., 2021]. Furthermore, Nething et al. [2020] developed a 3D printing method allowing the manufacturing of more complex spatial structures. For that, sand and urease active powder were selectively deposited within a container. After supplying and draining the mineralization solution, the solidification of the sand was limited to the desired locations resulting in a complex and geometrically stable structure [Nething et al., 2020]. Nevertheless, biomineralization can be applied not only to the fabrication of new building materials but also to repair existing materials, for example, by remediating cracks in concrete. As an alternative to conventional methods of repairing cracks with sealants or adhesive chemicals, biomineralization has shown promising results in improving the durability of cementitious building materials and restoration of stone monuments [Joshi et al., 2017]. An exciting and promising application is the concept of self-healing concrete. Bacterial cells, along with calcium ions, nutrients, and other supplements, are added to the concrete mixture. The spores of the bacteria survive in the solidified concrete and get activated when rainwater enters potential cracks in the concrete. The subsequent biomineralization fills the occurring cracks in the concrete. However, the necessary compounds could diminish the original strength of the material. Therefore more efforts and investigations are needed to employ self-healing concrete commercially [Lee and Park, 2018, Joshi et al., 2017].

Soil stabilization

The increased demand for infrastructure and building land engander suitable soil sites to become increasingly scarce. Biomineralization has become increasingly relevant as a potential alternative to chemical grouting in order to improve the soil strength and other properties [Terzis and Laloui, 2018, Rahman et al., 2020]. Similar to the construction material, in the case of improving the soils for construction, the precipitated calcium carbonate acts as a cement to bond loose material. It can be employed, for example, to mitigate fugitive dust emissions, which is a significant environmental issue in arid or semi-arid environments [Hamdan and Kavazanjian, 2016]. Much effort has also been put into analyzing and optimizing the resulting mechanical properties using column and large-scale experiments [Whiffin et al., 2007, van Paassen et al., 2010, Yasuhara et al., 2012, Al Qabany et al., 2012] and it was reported that mineralogy, particle size distribution, shape, and texture can influence the resulting strength of the treated soils [Umar et al., 2016]. With regards to sustainability and cost efficiency, Rahman et al. [2020] analyzed the use of biomineralization for the applica-

tions in pavement construction. They concluded that MICP at the current stage is neither a cost-effective nor an environmentally friendly alternative to conventional methods, at least for pavement constructions. However, regarding the increased interest in this technology and efforts to improve it, it seems to have potential in their opinion [Rahman et al., 2020].

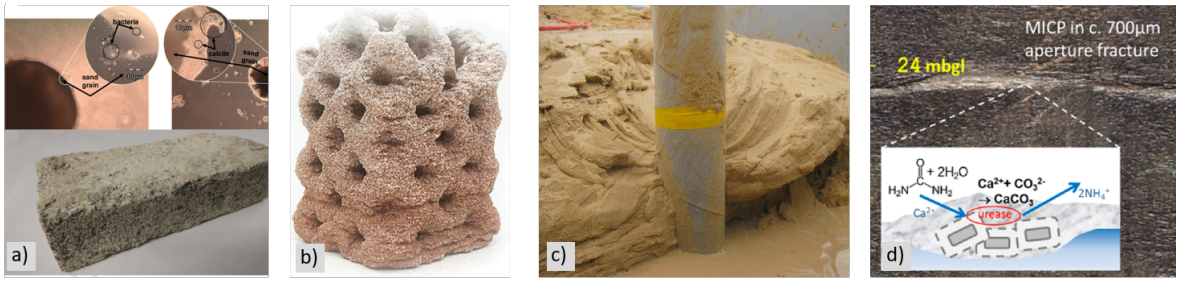

Figure 1.2: Engineering applications of biomineralization: a) Bio-brick made from human urine (reprinted from Lambert and Randall [2019] with permission of Elsevier, copyrigth 2019); b) 3D printed bio-cemented spatial structure (reprinted from Nething et al. [2020]); c) bio-cemented sand (reprinted from van Paassen et al. [2010] with permission of the American Society of Civil Engineers, Copyright 2010); d) Fracture sealing using MICP (reprinted with permission from Cuthbert et al. [2013], Copyright 2013 American Chemical Society)

Environmental remediation

Besides improving the mechanical properties of porous material, biomineralization also offers possibilities for environmental remediation applications, such as the immobilization of radionuclides and metals [Phillips et al., 2013]. A possible alternative to conventional remediation technologies, calcium carbonate-based co-precipitation of radionuclides like strontium or toxic metals like copper and arsenic is an option for a long time immobilization [Dejong et al., 2013, Pacheco et al., 2022, Rajasekar et al., 2021]. Proudfoot et al. [2022] for instance, recently studied the feasibility of MICP treatment in mine waste piles to reduce metals and acid leaching. Their laboratory assessments show the general feasibility of mitigating toxic metal releases into the environment.

Hydraulic control

Another promising application is to locally control and reduce the permeability of porous media. Hydraulic barriers can be created in order to prevent leakages of contaminants into aquifers [Phillips et al., 2013]. Cuthbert et al. [2013] applied MICP in order to reduce the

permeability of fractured rocks. In a field experiment, they achieved a significant reduction in the transmissivity of a single fracture. Moreover, in geologically stored carbon dioxide, mitigation strategies need to be considered to seal high permeable regions of the caprock to ensure the site's long-term safety. Due to the low viscosity of the cementation solutions, E/MICP treatment has the potential to be practical alternatives to conventional sealing technologies. Conventional sealing technologies often imply cement usage, resulting in higher viscosities of the injected fluids. Higher viscosities can prevent adequate penetration of small pore spaces and potentially hinder the proper sealing of microfractures [Phillips et al., 2013, Dejong et al., 2013]. Furthermore, the unconventional oil and gas development implicates the environmental risk of fluid leakage in the near-wellbore environment, where E/MICP could be applied to remediate unintentional leakage pathways [Phillips et al., 2016, Cuthbert et al., 2013]. Recently Kirkland et al. [2021] demonstrated in a field-scale experiment the successful application of MICP to remediate leaky wellbores. However, they pointed out that long-term seal integrity in the context of CO_2 storage scenarios still needs further investigations.

Summary

The effect of the engineering application of biomineralization in porous material can be summarized as follows. The induced calcium carbonate precipitation implies an alteration of the pore space resulting in the bonding of loose material and a reduction of porosity. This consequently affects mechanical and hydraulic properties like the Young modulus, shear modulus, or compressive strength and the permeability of porous media. Obviously, in the application of biomineralization in the construction sector, the mechanical properties are the key parameters to consider and optimize, while it is mainly the permeability for leakage mitigation scenarios. However, when realizing any of those applications, the transport of the reactive cementation solutions is strongly dependent on the changing permeability during the application. Consequently, considering the change of porosity and permeability is crucial when planning and conducting MICP or EICP treatments in any engineering application. Therefore a fundamental process understanding regarding the relationship between porosity and permeability is essential.

1.2 Numerical modeling of biomineralization

Subsurface flow and transport coupled to biogeochemical reactions relates extremely complex processes which are still challenging to model [Koch et al., 2021]. Yet, for tasks like site characterization, improvement of process understanding and sensitivities, feasibility studies, risk assessment, or quantification of uncertainties, numerical modeling is an essential tool for planning and conducting field applications in the subsurface. Large-scale implementation of such projects often imply involvement of different stakeholders and competitive interests, which need to be communicated at the science-policy interface [Scheer et al., 2021]. Recently, much effort has been put into the development of numerical models for calculating and predicting field applications of M/EICP [van Wijngaarden et al., 2011, Ebigbo et al., 2012, Hommel et al., 2015, Nassar et al., 2018, Cunningham et al., 2019]. For that purpose, these models are required to be able to calculate large domains in the range of several meters to kilometers. This implies averaging of pore-scale information into bulk properties, like permeability and porosity described by the concept of a representative elementary volume (REV) (see Section 2.1 for definitions). The focus of improving these REV-scale models has been mainly on the kinetics of the biomineralization processes [Landa-Marbán et al., 2021, Hommel et al., 2015, 2020]. In parallel to the development of the numerical models, numerous experimental studies were performed in order to investigate kinetic parameters under different conditions [Cuthbert et al., 2012, Lauchnor et al., 2015, Mitchell et al., 2019, Feder et al., 2021]. Besides detailed information about chemical reaction kinetics, these REV-scale models inherently rely on upscaled porosity-permeability relationships. Even though several approaches are available in the literature to correlate the change of porosity to a corresponding change of permeability, like Kozeny-Carman, Verma-Pruess, or simple power-law relationships (see Section 2.4 for their definitions), it remains unclear in what way exactly pore space alteration influences the hydraulic response. For example, varying initial and operating conditions could lead to differences in the corresponding relationships. In order to understand and reveal the essential mechanisms leading to such variations, detailed knowledge on the pore-scale is necessary [Hommel et al., 2018]. It is obvious and undeniable that the REV-scale is the appropriate scale to model field-scale applications of MICP or EICP, where computational demands can become a limiting factor. However, it is the pore-scale where the morphological changes occur and from where we, consequently, need to derive new insights.

Also for that purpose, numerical simulation can be valuable. Numerical pore-scale and pore-network models are very useful for a general process understanding in the context of pore

space alterations and the resulting hydraulic effect [Zhang and Klapper, 2014, Qin et al., 2016, Minto et al., 2019, Sabo and Beckingham, 2021, Jung and Meile, 2021]. They allow for a very systematic analysis of specific processes but still imply simplifications and assumptions. Therefore, experimental investigations on the pore-scale are indispensable to enhance our understanding of the relevant processes during biomineralization affecting the porosity and permeability of a porous medium.

1.3 Microfluidic investigations of biomineralization

During the last 35 to 40 years, microfluidics has been increasingly utilized to study the behavior of fluids in porous structures in various research areas, including applications in life science, chemistry, or fluid mechanics, to only name a few [Karadimitriou and Hassanizadeh, 2012]. This short review gives an overview of microfluidic investigations during the past few years that aimed at studying the behavior of biomineralization in the context of engineering applications of EICP and MICP. The following studies were carried out right before or in parallel to our work and used state-of-the-art microfluidic cells either made out of glass or Polydimethylsiloxane (PDMS) (see Section 2.5 for details).

Wang et al. [2019a] showed successfully the use of a microfluidic chip made out of PDMS to improve the understanding of MICP on the pore scale. With optical microscopy, they could observe the bacteria distribution within the pore structure and monitor forming precipitates in narrow pore throats and open pore bodies during a staged injection strategy. In two follow-up studies [Wang et al., 2019b, 2021], they were able to observe the formation of irregularly shaped precipitates which may subsequently dissolve and reprecipitate into regularly shaped precipitates and argued with Ostwald ripening in the context of calcium carbonate precipitation. According to the theory of Ostwald, ACC is the first phase to precipitate but is unstable and consequently transforms into more stable polymorphs like calcite or vaterite (see Section 2.3.2 for details on the chemistry of calcium carbonate). In Wang et al. [2022] they identified the injection strategy to be crucial for the resulting size of the precipitates. Lower injection rates of the cementation solution led to larger crystals and with respect to their motivation, to better soil improvements in terms of soil strength.

In the work of Zambare et al. [2020], the mineralogy of MICP was studied using single-cell drop-based microfluidics. A microfluidic device made of PDMS was used to generate

droplets containing single ureolytically active bacterial cells. Mineral precipitation was studied using Raman spectroscopy to differentiate polymorphs of calcium carbonate. They found that the ratio of ACC to vaterite decreases over time, and from other experimental methods like fluorescence microscopy and dispersive X-ray Spectroscopy (EDX), they inferred the additional presence of calcite. This study generally confirms the hypothesis of Wang et al. [2019b, 2021] that polymorph transitions during MICP occur mainly from ACC to vaterite and calcite.

Xiao et al. [2021] also investigated pore-scale characteristics during the process of MICP using a microfluidic cell with a homogeneous pore structure made out of PDMS. However, in contrast to the studies mentioned above, Xiao et al. [2021] visualized the MICP process under continuous flow conditions. Injecting the bacterial suspension and the cementation solution simultaneously from two separate inlets into the cell, they focused on the transversal mixing of bacteria and chemicals across the pore structure. They found that precipitation started in the lower part of the cell into which bacteria suspension was injected. While precipitation continues and the permeability is reduced locally, the flow direction shifts, and precipitation also occurs in the upper part of the cell. Due to the observation of partial clogging, the formation and shifting of flow channels, they hypothesized that the mixing of the cementation solution and bacterial suspension increases as precipitation continues. Moreover, they observed irregularly shaped, rhombohedral, and spherical precipitates during their experiments. From Raman spectroscopy analysis, they concluded that the irregular-shaped precipitates are ACC, the rhombohedral are calcite, and the spherical ones are in the transition from vaterite to calcite. In a subsequent study, Xiao et al. [2022] additionally studied the influence of the $CaCl_2$ concentration in the cementation solutions on the transversal diffusion at a quiescent state. Instead of the homogeneous pore structure consisting of uniformly distributed pillars used in their previous study, they implemented sand grains into the micromodel this time. They found that lower $CaCl_2$ concentrations led to a more homogeneous distribution of precipitates and concluded that increased $CaCl_2$ hindered the bacterial diffusion. Moreover, their observations indicate that the surface of the sand grain particles does not offer preferential nucleation sites at the quiescent state.

Kim et al. [2020] used micromodels made out of borosilicate to investigate EICP during a sequential injection of the reactive solutions. They analyzed the size distribution of the precipitates intending to estimate kinetic parameters and compared the results to a simplified kinetic model. For that, certain shapes have been assumed to derive the volume of the precipitates based on their 2D projections, captured during optical microscopy imaging. They

showed that their comparison between the experimental results and their kinetic model was significantly affected by the assumed shape approximation of the precipitates.

In summary, there have been various studies regarding pore-scale phenomena of biomineralization (MICP and EICP). The research goals range from fundamental process understanding, kinetic aspects of the precipitation process, and mixing of the reactive solutions to the optimization of injection strategies concerning the enhancement of soil strength. One crucial aspect that has been addressed in almost all these studies is the importance of the polymorphous nature of calcium carbonate, or more precisely, the coexistence of ACC, vaterite, and calcite and their transformation from one into the other. However, none of these recent experimental studies explicitly focused on the impacts on the hydraulic responses, more precisely on the REV-scale parameter permeability. Therefore, the pore-scale effects of biomineralization leading to a change of the REV-scale properties porosity and permeability are still not fully understood yet.

1.4 Objective and structure of the thesis

From the previously described engineering applications of biomineralization, ranging from construction material and soil stabilization to hydraulic control and environmental remediation, porosity and permeability alteration during the treatment is crucial to consider. While REV-scale models are essential tools to support field applications, they rely on porosity-permeability relationships. Recent studies have shown that microfluidics is a suitable experimental technique for exploring pore-scale characteristics during the biomineralization process. However, the effect of biomineralization on the hydraulic responses has still not yet been fully understood. This current lack of knowledge motivated our work on porosity and permeability alterations during biomineralization in porous media. Therefore, we aim to observe and interpret phenomena on the pore-scale during mineral precipitation to conclude on the REV-scale properties, porosity, and permeability.

In Chapter 2, the theoretical background for this work is outlined. This includes general definitions of the considered scales in porous media, the fundamentals of flow and transport phenomena, and geochemical reactions. Moreover, various concepts for determining the permeability of a porous medium are outlined, and an overview of microfluidic methods is given. Furthermore, the three contributions and their objectives are summarized in Chapter 3.

The corresponding publications are provided in Appendix A-C. Finally, in Chapter 4, we present our conclusions, limitations and perspectives for possible further research.

2 Theoretical background

This chapter provides an overview of the fundamentals for this work and serves as a general theoretical framework, providing the relevant terms and definitions. This chapter is subdivided into four sections: At first, porous media are defined, and the considered spatial scales in the context of subsurface processes are given in Section 2.1. Secondly, Section 2.2 describes the background of flow and transport in porous media, including the pertinent properties of a porous medium, the pore- and REV-scale description of flow, and the relevant transport mechanisms. Thirdly, geochemical fundamentals in the context of biomineralization are given in Section 2.3. These include some basic terms and definitions of chemical reactions, the chemistry of calcium carbonate, and the mechanisms of induced calcium carbonate precipitation. Subsequently, in Section 2.4, various approaches to determine the permeability are outlined, ranging from the original experiments of Henry Darcy and classical constitutive relationships and finally to porosity-permeability relationships for altered porous media. Finally, in Section 2.5, the background of microfluidics as the science for investigating fluid interactions in microchannels is provided, by giving an overview of different micromodel fabrication methods and of measurement and visualization techniques.

2.1 Porous media and their scales of consideration

A porous medium is a solid material that includes void space. This is probably the most intuitive and general definition of a porous medium and would include things like a hollow cylinder or a solid block with a few isolated pores. In this work and field of research, we want to define a porous medium related to fluids flowing through it. For that, a better definition would be to describe it as a solid matrix with connected void space (pore space) inside and a relatively high specific surface [Bear, 1972]. Examples are filter paper, sand filters, sponges, diapers, and even the canvases of oil paintings, to only name a few. The research presented

here focuses on the geoengineering application of biomineralization which can be employed but is not limited to subsurface processes, e.g., in soils, aquifers, or other geological formations. Such subsurface processes can be observed and studied on different spatial scales at different levels of detail.

For geoengineering applications in the subsurface, we can categorize spatial scales into the following categories [Hommel et al., 2018]:

- **molecular scale**: Pico- to nanometers
- **pore scale**: Micro- to millimeters
- **REV scale** (representative elementary volume-scale): Millimeters to meters
- **field scale**: Meters to kilometers

The most appropriate scale for analyzing processes is a matter of the necessary level of detail and, consequently, depends on the process itself. However, there is always a trade-off between the level of detail and the size of the considered system. Figure 2.1 gives an overview of the different spatial scales in the context of engineered biomineralization in porous media, ranging from pikometer (10^{-12}m) to kilometer (10^{3}m). Individual molecules and their interactions can be described in exact detail on the **molecular scale**. Theoretically, most of the relevant processes, like biomineralization or fluid flow, can be explained and described by molecular interactions. However, it is not expedient to describe such processes on the molecular scale for most engineering applications. It is often more feasible to average over a sufficient number of similar molecules to analyze a more extensive system, assuming matter is continuous in space and time. With this continuum approach, averaged quantities, like temperature or density, can be defined. In the case of a porous medium, the pore geometry is described by differentiating the solid matrix and the void space while resolving the exact pore geometry. This microscopic consideration is referred to as the **pore scale**. When using the example of biomineralization, one can still describe the chemical reaction and the corresponding pore space alteration, even though the molecules themself are averaged as a continuum. The continuum description, of course, needs upscaling assumptions and consequently reduces the level of detail. The next step would be to average over several pores and solids within a porous medium, defined as a representative elementary volume (REV). On the **REV scale** the pore-scale properties, like the exact pore geometry, are represented by average quantities of an REV, such as porosity and permeability (also see Section 2.2.1). When it comes to geoengineering applications, for example, the remediation of leakages in

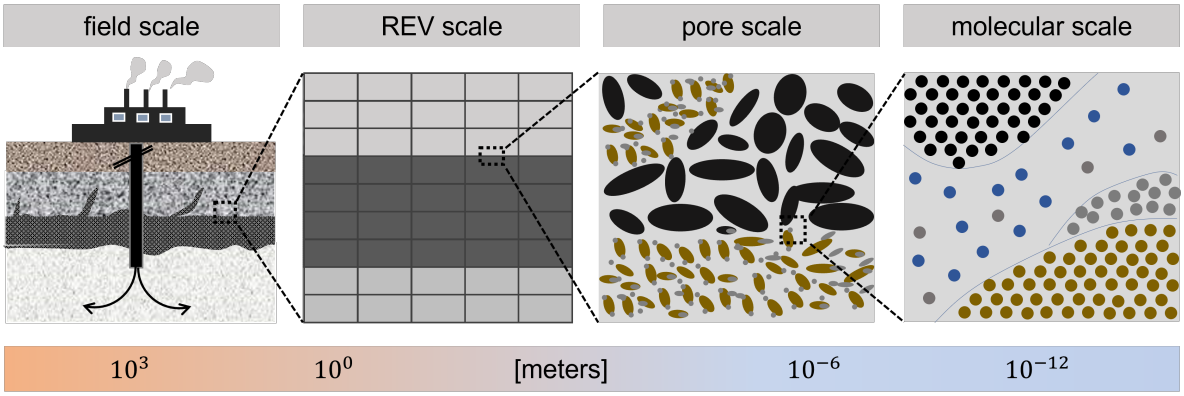

Figure 2.1: Relevant scales in the context of engineered biomineralization in porous media. From left to right: CO_2 injection into the subsurface with biomineralized caprock (field scale); domain discretized into REV's with averaged quantities (REV scale); fully resolved pore geometry including various grains and biominerals (pore scale); individual molecules representing precipitation and dissolution (molecular scale). The scaling bar on the bottom roughly maps the unit of length to the categorized spatial scales.

the subsurface, the considered spatial domain comprises several meters or kilometers. In order to describe these applications on the **field scale**, we can use numerical simulation tools representing the subsurface subdivided into multiple REV's, as illustrated in Figure 2.1.

We have to keep in mind that choosing the spatial dimension of a scale is often an arbitrary decision, and the transition between scales is fluent [Weishaupt, 2020]. However, this categorization of scales is essential when describing relevant processes - either resolve them in detail or average them to effective quantities concomitant with a loss of accuracy. In this work, we look at the pore scale, intending to draw conclusions for the description on the REV scale.

2.2 Flow and transport in porous media

In this section, flow and transport mechanisms in porous media are explained. At first, we describe the relevant properties of a porous medium before outlining the pore- and REV-scale descriptions of flow in porous media and their mathematical formulations. Furthermore, transport processes, namely diffusion, advection, and dispersion, are defined.

2.2.1 Porous medium properties

As described in the previous section, the focus of this work is related to subsurface processes where examples of porous media are soils, aquifers, or other geological formations. In the context of biomineralization, we want to focus on the alternating pore space and the corresponding flow resistance of the porous medium. In terms of REV-scale parameters, this refers to porosity and permeability. In Figure 2.2 a porous medium is schematically illustrated on the pore and the REV scale: At the pore scale, the shapes of the grains and pores are fully resolved. The calcium carbonate precipitates evolve during the treatment of biomineralization and thus lead to a change of the solid matrix and consequently reduce the pore space.

Considering a porous medium as an REV requires averaging of pore-scale characteristics over a sufficiently large domain and introducing averaged properties like porosity and permeability. The correct size of the REV depends on the considered property. The size of an REV should, on one hand, be large enough to average out microscopic inhomogeneities, and on the other hand, be small enough to represent macroscopic inhomogeneities. In other words, the REV should be homogeneous concerning the characteristic quantities, which should not change significantly when changing the size of the considered domain, as illustrated in Figure 2.2 on the right [Helmig, 1997]. One crucial quantity is the porosity ϕ which is a dimensionless number and defined as the fraction of volume of the pores V_{pore} to the total volume V_{total} of an REV:

$$\phi = \frac{V_{\text{pore}}}{V_{\text{total}}} \tag{2.1}$$

Another important REV-scale property of a porous medium is the intrinsic permeability. It is a measure of the ease of fluid flowing through a porous medium or the reciprocal of the resistance of a porous medium to fluid flow. In Darcy's law, permeability relates the pressure gradient to the flow velocity, which is more precisely described in the next section.

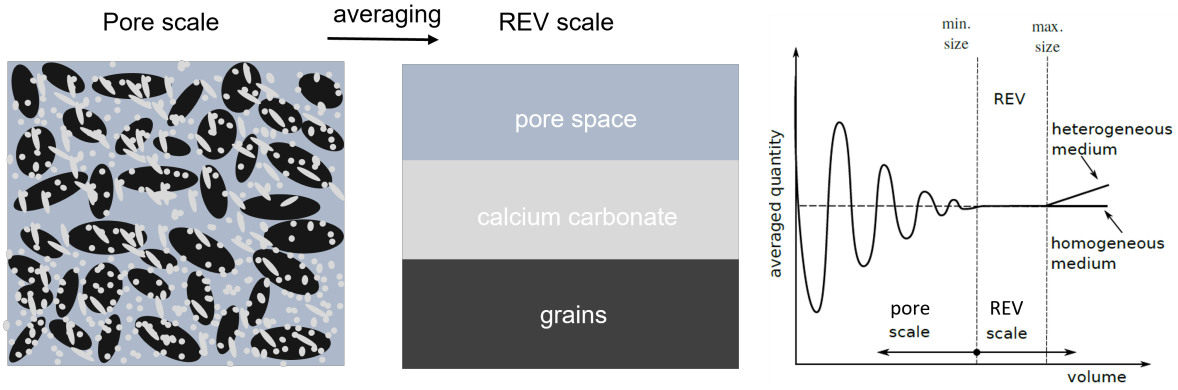

Figure 2.2: REV concept on the example of calcium carbonate precipitataion in porous media. Right: REV size, for an exemplary averaged quantity (after Weishaupt [2020] and Helmig [1997]).

2.2.2 Pore- and REV-scale description of flow in porous media

Reynold's Number

An important dimensionless number for describing the flow regime in porous media is the Reynold's number (Re) which is defined as:

$$\mathrm{Re} = \frac{\text{inertial forces}}{\text{viscous forces}} = \frac{v \cdot L}{\nu}, \tag{2.2}$$

with the velocity, v, the characteristic length, L, and the kinematic viscosity of the fluid, ν. High Re's indicate turbulent flow conditions, while lower Re's specify laminar flow regimes. Re's tend to be very small in typical subsurface applications, meaning that viscous forces dominate over inertial forces. Under creeping flow conditions ($\mathrm{Re} < 1$), the inertial forces can be neglected.

Pore-scale description (Navier-stokes-equations)

The flow through a porous medium can be described mathematically on the pore scale or on the REV scale based on mass and momentum balance equations. Fluid flow on the pore scale can be formulated with the Navier Stokes equations. Assuming an incompressible and newtonian fluid, the continuity equation (Equation 2.3) and the momentum balance (Equation

2.4) can be formulated as the following:

$$\nabla \cdot (\mathbf{v}) = 0 \tag{2.3}$$

$$\frac{\partial \mathbf{v}}{\partial t} + \nabla \cdot (\mathbf{v}\mathbf{v}^{\mathrm{T}}) = -\frac{1}{\rho}\nabla p + \nu \nabla^2 \mathbf{v} + \mathbf{f} \tag{2.4}$$

The continuity equation implies the conservation of mass, meaning that mass can neither vanish nor be produced. For an incompressible fluid, the continuity equation results in the divergence of the velocity being equal to zero within one control volume. The momentum equation consists of the advective term $\nabla \cdot (\mathbf{v}\mathbf{v}^{\mathrm{T}})$, the pressure term $-\frac{1}{\rho}\nabla p$ and the shear term $\nu \nabla^2 \mathbf{v}$, while $(\frac{\partial \mathbf{v}}{\partial t})$ depicts the change of the velocity in time. The advective term can be neglected under the assumption of creeping flow conditions ($\mathrm{Re} < 1$), which is often referred to as the Stokes equations. $\mathbf{f}$ represents an additional volume force which could be gravity or an additional drag term.

The 3D domain could be simplified as quasi-two-dimensional when describing flow in microfluidic cells with a high aspect ratio between the width w and the height h. We can account for the friction caused by the upper and lower wall with an additional drag term, $\mathbf{f}_{\mathrm{drag}}$ assuming a parabolic velocity profile between the walls. The additional drag term can be formulated as [Weishaupt, 2020]:

$$\mathbf{f}_{\mathrm{drag}} = -\left(12\mu/h^2\right)\mathbf{v}_{\mathrm{2D}}, \tag{2.5}$$

for $\mathbf{v}_{\mathrm{2D}}$ representing the height averaged velocity.

With the Navier-stokes-equations, the exact flow field can be described, while no-slip conditions at the wall of the pores define the boundary conditions. In the case of precipitation, the pore morphology changes. Consequently, the local boundary conditions on the pore walls alter such that the local velocity profile changes.

REV-scale description of flow (Darcy's law)

When giving up on precisely describing local pore geometries, a porous medium can be described using an REV approach, assumed that the size of the considered REV is sufficiently large so that the characteristic quantities do not change when changing the size of the averaging volume (see Section 2.2.1). If that is the case, flow through a porous medium can

mathematically be described by Darcy's Law, which is a simplified momentum balance valid under creeping flow conditions (Re < 1) and can be formulated as:

$$\mathbf{v} = -\frac{\mathbf{k}}{\mu}(\nabla p - \rho \mathbf{g}), \tag{2.6}$$

with μ and ρ being the dynamic viscosity and the density of the fluid. The intrinsic permeability, $\mathbf{k}$, relates the potential gradient $(\nabla p - \rho \mathbf{g})$ and the resulting Darcy-velocity $\mathbf{v}$. In some cases, the gravity term can be neglected, for instance, when applying Darcy's Law in microfluidics, where the flow is usually horizontal, and volumes and dimensions are tiny. There are different possibilities to determine the intrinsic permeability of a porous medium. Experimental methods and constitutive relationships exist to determine the permeability of a porous medium. Some of them are summarized in Section 2.4.

2.2.3 Transport processes in porous media

When discussing transport processes in porous media, we again need to clarify on which scale we describe the phenomena. In our case, we look at the pore and REV scale as defined in Section 2.1. On the pore scale, solute transport can be described by advection and diffusion, while additionally, dispersion needs to be considered for the description on the REV scale.

Diffusion

Molecular diffusion refers to the random thermal motion of molecules. For example, when the concentration of solutes within a liquid is unevenly distributed, statistically, more molecules move from locations with high concentrations to regions with low concentrations. At the pore scale, where the liquid phase is considered to be a continuum and solutes are described with the concept of concentrations, this leads to the transport of solutes driven by a concentration gradient (∇c). Mathematically, the diffusive flux can be described by Fick's Law:

$$\mathbf{j} = -D\nabla c \tag{2.7}$$

The molecular diffusion coefficient (D) strongly depends on the type of solute and the temperature.

Advection

Another transport process contributes when the liquid phase moves relative to the reference system, namely advection. It refers to the transport of a solute by the bulk movement of the fluid phase.

$$\mathbf{j} = c\,\mathbf{v} \tag{2.8}$$

Dispersion

Since the exact pore geometry is not resolved on the REV scale, the concept of dispersion needs to be introduced. Fluctuations of the velocity field due to the heterogeneous nature of a porous medium on the pore scale lead to dispersion. It is a scale-dependent process describing the solute spreading in the lateral and longitudinal direction of the averaged fluid flow. Phenomenologically it is similar to diffusion, and thus, for REV-scale modeling, often incorporated into the diffusion coefficient.

Péclet number

In order to characterize transport processes, the dimensionless Péclet number (Pe) can be used. It is defined as the ratio of the advective to the diffusive transport rate.

$$\mathrm{Pe} = \frac{\text{advective transport rate}}{\text{diffusive transport rate}} = \frac{v\,L}{D}, \tag{2.9}$$

with the bulk velocity, v, the diffusion coefficient, D, and the characteristic length, L. For low Pe's ($\mathrm{Pe} < 1$), the solute transport is diffusion-dominated, and for high Pe's ($\mathrm{Pe} > 1$), it is advection-dominated.

2.3 Geochemical reactions

This section presents the theoretical background regarding the relevant mechanisms in geochemistry. First, we explain general terms and definitions of chemical reactions and the chemistry of calcium carbonate before discussing the reactions and processes involved during induced calcium carbonate precipitation.

2.3.1 Terms and definitions of chemical reactions

Mass action law and dynamic equilibrium

Chemical reactions are, in general, initiated by the accidental collision of molecules that have the potential to react. Each chemical reaction tends to reach equilibrium. Depending on the considered time scale, some reactions reach a dynamic equilibrium very fast and, therefore, can be assumed to be equilibrium reactions. The dynamic equilibrium describes the state during a reversible reaction where reactants and products transition at the same rates. Consequently, the resulting activities of reactants and products stay constant. Equation 2.10 illustrates such an exemplary chemical reaction, where A_i represents the reactants, B_j the products and $k_{-/+}$ the rate constants of the partial processes [Möller, 2015].

$$\nu_1 A_1 + \nu_2 A_2 + ... \nu_m A_m \underset{k_-}{\overset{k_+}{\rightleftharpoons}} \nu_{m+1} B_1 + \nu_{m+2} B_2 + ... \tag{2.10}$$

The law of mass action describes the relationship between the activities of the reactants and the products during a dynamic equilibrium. The equilibrium constant K_{eq} is defined as:

$$K_{eq} = \frac{[B_1]^{\nu_{m+1}} [B_2]^{\nu_{m+2}} ...}{[A_1]^{\nu_1} [A_2]^{\nu_2} ...} \tag{2.11}$$

while the brackets denote the corresponding activities, meaning the effective-reactive concentrations of a substance. In ideal systems, activities can be simplified to the concentrations of the reactants and products, respectively. For simplicity, we refer to concentrations instead of activities in the following. The equilibrium constant depends on various factors, like phase composition, temperature, or pH value. Phase equilibrium can often occur in nature, for instance, in evaporation-condensation, adsorption-desorption, or dissolution-precipitation reactions [Möller, 2015].

Solubility and precipitation

Precipitation can be defined as the process when solutes in a solution solidify. A standard method to induce precipitation is to mix two solutions of soluble salts that react, and one or more of the products is a precipitate. Since dissolution-precipitation reactions can generally be considered as equilibrium reactions [Möller, 2015], an exemplary reaction equation

is given in 2.12, where $A_\alpha B_\beta(s)$ describes the solid substance, $A(aq)$ and $B(aq)$ indicate the solutes respectively. The equilibrium constant K_{eq} in Equation 2.13 can be formulated analogously to Equation 2.11. Since the term $[A_\alpha B_\alpha(s)]$ denotes the concentration of AB in the pure substance AB, it is constant and the solubility product can therefore be defined as in Equation 2.14. For very sparingly soluble salts, the equilibrium concentrations of salt in a solution can be calculated from the solubility product as described in Equation 2.15.

$$A_\alpha B_\beta(s) \rightleftharpoons \alpha A(aq) + \beta B(aq) \tag{2.12}$$

$$K_{eq} = \frac{[A]^\alpha [B]^\alpha}{[A_\alpha B_\alpha(s)]} \tag{2.13}$$

$$K_{sp} = [A]^\alpha [B]^\alpha = K_{eq}[A_\alpha B_\alpha(s)] \tag{2.14}$$

$$c_{eq} = \left(\frac{K_{sp}}{\alpha^\alpha \beta^\beta}\right)^{1/(\alpha+\beta)} \tag{2.15}$$

According to Mullin [1993] precipitation very often refers to fast crystallization. Precipitation processes are widely used as laboratory techniques and are prevalent for industrial and geoengineering applications. Besides the three basic steps of crystallization processes, namely supersaturation, nucleation, and crystal growth, precipitation includes two essential subsequent steps: agglomeration and ageing.

Supersaturation, nucleation and growth:
As mentioned precipitation-dissolution reactions can often be assumed to be in equilibrium, however, this depends on the time and spatial scales that are considered. The equilibrium concentration of a salt in aqueous solution could be exceeded without directly causing precipitation. This consequently results supersaturation of the solution which is often defined as the ratio of the concentration in a solution, c to the equilibrium concentration c_{eq}:

$$S = \frac{c}{c_{eq}} \tag{2.16}$$

Supersaturation describes a non-equilibrium, and thus, a metastable state, and is a measure for the driving force to cause nucleation. We can differentiate between two different types of nucleation: homogeneous and heterogeneous nucleation. Homogeneous nucleation describes how small nuclei form directly out of the solution without any initial nucleation seeds. This requires generally higher supersaturation states compared to heterogeneous nucleation. Heterogeneous nucleation, in contrast, is defined as the nucleation at an interface with another phase, like the surface of dust, bubbles, grains, or other particles suspended in the solution

[Nebel, 2008]. Once there are nuclei of the considered substance present, these crystals can grow during the state of supersaturation. The growth of the crystals in aqueous solutions strongly depends on the availability of preexisting crystals, the concentrations, the temperature, and the agitation of the system [Mullin, 1993].

Agglomeration and aging:
Since precipitation usually refers to a relatively fast crystallization of the solutes, agglomeration and aging play an important role, especially for induced calcium carbonate precipitation. Tiny particles in liquid suspension tend to cluster together since interparticle collision may result in a permanent attachment if the particles are small enough. This results in agglomerations of small particles [Mullin, 1993]. Aging processes during and after the precipitation can occur, while we consider ripening and phase transformation as relevant during biomineralization. Ostwald ripening in the context of precipitation refers to the process where larger particles grow at the expense of small particles. This process can be explained by the tendency of the solid phase to adjust itself to achieve a minimum total surface free energy. Besides ripening, phase transformation can also occur within time. Minerals might be polymorphous, meaning that different polymorphs of the same mineral exist. A substance capable of exhibiting crystallinity sometimes precipitates as a metastable, possibly amorphous form. According to Ostwald's rule of stages, the initial precipitation as a metastable phase is followed by a phase transformation to other more stable polymorphs of the considered substance. Calcium carbonate can occur as different polymorphs, which is further described in Section 2.3.2. Phase transformation during engineered biomineralization can be an essential aspect to consider.

Chemical reaction kinetics

In the context of biomineralization, as we employ it, besides precipitation, also the hydrolysis of urea plays an essential role. The hydrolysis of molecules is a chemical reaction where water breaks down chemical bonds. The urea hydrolysis can be considered a relatively slow reaction at moderate temperatures. However, the enzyme urease can catalyze the reaction increasing the reaction rate by several orders of magnitude. Still, in contrast to equilibrium reactions where the reaction takes place relatively fast, for the hydrolysis of urea, kinetics need to be considered, which are explained in the following, categorized into *general kinetics*, *temperature dependency* and *enzyme kinetics*.

General kinetics:
As an example of a chemical reaction where kinetics need to be considered, an arbitrary dissociation reaction is given in Equation 2.17 where a substance AB dissociates into A and B. The right arrow indicates that the reaction mainly occurs in one direction, and a corresponding reaction quotient, Q_r, can be defined as in Equation 2.18. In contrast to the definition of the equilibrium constant, K_eq in Equation 2.11, the concentrations of A, B and AB are not expressed as equilibrium concentrations. Q_r describes the state of the chemical reaction, and in case the chemical reaction reaches equilibrium, the reaction quotient is equal to the equilibrium constant ($Q_\mathrm{r} = K_\mathrm{eq}$) [Möller, 2015].

$$\mathrm{AB} \longrightarrow \mathrm{A} + \mathrm{B} \tag{2.17}$$

$$Q_\mathrm{r} = \frac{[\mathrm{A}][\mathrm{B}]}{[\mathrm{AB}]} \tag{2.18}$$

The reaction order of a chemical reaction is determined by the number of reactants whose concentrations affect the reaction rate. In this exemplary simple case, the rate law can be written as:

$$-\frac{d[\mathrm{AB}]}{dt} = \frac{d[\mathrm{A}]}{dt} = \frac{d[\mathrm{B}]}{dt} = k_r[\mathrm{AB}] = r, \tag{2.19}$$

with k_r being the rate coefficient and r being the reaction rate. Since the reaction rate only depends on the concentration of AB to the power of one ($[AB]^1$), the example reaction is a first-order reaction. The integration of such a first-order reaction over time is relatively simple and the concentrations of the reactants and the reaction rates can be determined explicitly for a given reaction rate coefficient:

$$\int_{[\mathrm{AB}_0]}^{[\mathrm{AB}]} \frac{1}{[\mathrm{AB}]} d[\mathrm{AB}] = k \int_{[\mathrm{A}_0]}^{[\mathrm{A}]} dt \tag{2.20}$$

$$[\mathrm{A}] = [\mathrm{A}]_0 \, e^{-kt} \tag{2.21}$$

Temperature dependency (Arrhenius equation):
Chemical processes are generally temperature-dependent and usually faster at higher temperatures. The Arrhenius equation describes quantitatively the relation between the reaction rate coefficient, k_r, and the temperature, T:

$$k_\mathrm{r} = a_0 e^{\left(-\frac{E_\mathrm{A}}{RT}\right)}, \tag{2.22}$$

with E_A being the activation energy, R the molar gas constant, and a_0 a pre-exponential

factor, representing the probability of a chemical reaction [Bisswanger, 2017]. However, when deriving empirical relations from experimental observations, the parameter a_0 and E_A are often fitted to the experimental data by lumping the activation energy and the gas constant together as one parameter.

Enzyme kinetics (Michaelis-Menten theory):
In biochemistry, catalytic reactions play a crucial role. Enzymes are proteins that act as catalysts, which accelerate chemical reactions without undergoing any changes themselves. The Michaelis-Menten mechanism can describe a typical enzymatically induced reaction. The reaction steps can be described in their most simple steps as the following:

$$\mathrm{E} + \mathrm{S} \rightleftharpoons \mathrm{ES} \longrightarrow \mathrm{E} + \mathrm{P}, \tag{2.23}$$

with E being the enzyme, S the substrate, and P the product of the overall reaction. In the first step, the substrate, S, forms with the enzyme, E, an enzyme-substrate-complex, ES. Consequently, the reaction product, P, is formed, and the enzyme is released without being modified. Assuming steady-state condition regarding the formation and break down of the enzyme-substrate-complex ($d[\mathrm{ES}]/dt = 0$), the reaction rate can be defined as the following according to the Michaelis-Menten theory:

$$r = \frac{r_{\max}[\mathrm{S}]}{K_\mathrm{m} + [\mathrm{S}]} \tag{2.24}$$

with r being the reaction rate, r_{max} the maximum reaction rate, and K_m the Michaelis constant, indicating the substrate concentration at which half of the maximum reaction rate is reached. Figure 2.3 shows exemplarily the reaction rate over the substrate concentration according to Equation 2.24. In case the substrate concentration is much larger than the Michaelis-Menten constant ($[\mathrm{S}] >> K_\mathrm{m}$), the reaction can be approximated to be zero-order, meaning that the reaction rate is independent of the substrate concentration. In the case that the substrate concentration is smaller than the Michaelis-Menten constant ($[\mathrm{S}] << K_\mathrm{m}$), the reaction can be approximated to be first-order. Additional mechanisms during enzyme reactions, like product inhibition, inactivation of enzymes, etc., could also affect the kinetics, complicating the reaction rates' mathematical descriptions. However, these cases go beyond the scope of this dissertation. In the presented work, the conditions allow for describing the hydrolysis of urea as a first-order reaction.

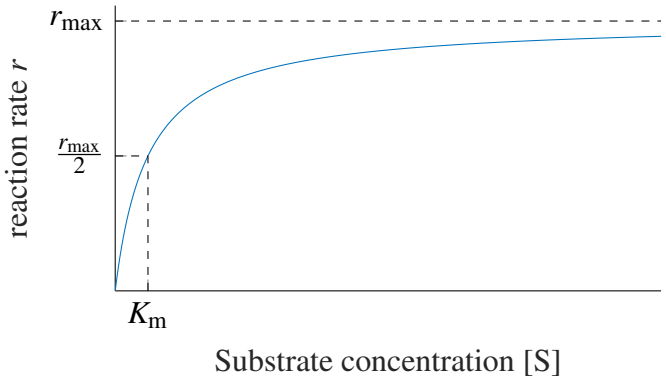

Figure 2.3: Examplary plot according to the Michaelis-Menten equation (Equation 2.24)

Dahmköhler Number

Geochemical reactions in the subsurface often occur in aqueous, flowing solutions. Reactive transport describes processes where solutes are transported with the flow and simultaneously react. In such cases, the dimensionless Damköhler numbers are essential to characterize the importance of each mechanism by relating the reaction rates to the transport processes of the solutes. Two separate Dahmköhler numbers exist, one regarding advective and one regarding diffusive transport:

$$\mathrm{Da_I} = \frac{\text{reaction rate}}{\text{advective mass transport rate}} = \frac{k_\mathrm{r} L c_0^{n-1}}{v} \tag{2.25}$$

$$\mathrm{Da_{II}} = \frac{\text{reaction rate}}{\text{diffusive mass transport rate}} = \frac{k_\mathrm{r} L^2 c_0^{n-1}}{D} \tag{2.26}$$

Here, k_r is the reaction rate coefficient, L is the characteristic length scale, D is the binary diffusion coefficient, c_0 is the initial concentration, and n indicates the reaction order. In the case $\mathrm{Da_I} < 1$, the chemical reaction is slower than the advective transport, meaning that the reaction controls the system. This is referred to as reaction-controlled. In contrast for $\mathrm{Da_I} > 1$, the system can be considered as transport-controlled [Hommel et al., 2018].

2.3.2 Chemistry of calcium carbonate

Two essential aspects of calcium carbonate need to be considered in biomineralization: Calcium carbonate is the calcium salt of the carbonic acid, and it occurs as different polymorphs.

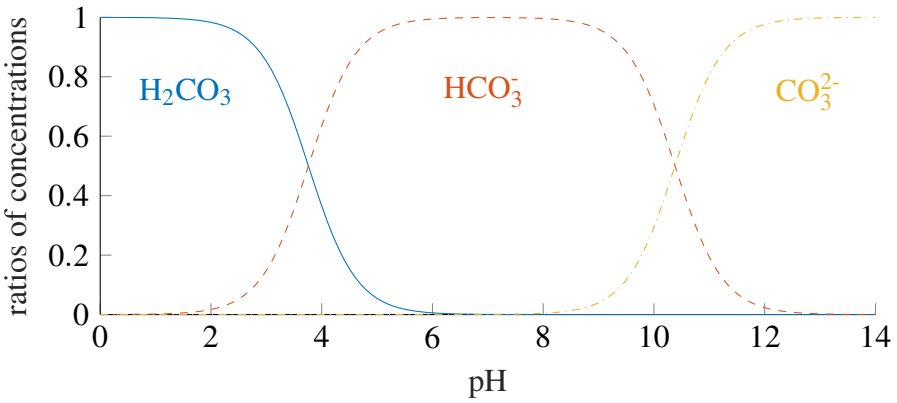

Figure 2.4: Bjerrum plot of the diprotic carbonic acid; $pK_{a,1} = 3.76$ and $pK_{a,2} = 10.38$

Both of these aspects are discussed in the following.

Carbonic acid is a weak diprotic acid and consequently dissociates from H_2CO_3 into HCO_3^- and CO_3^{2-} depending on the pH value. The two dissociation steps with their corresponding logarithmic acid constants $pK_{a,1}$ and $pK_{a,2}$ are shown in the following two equations [Möller, 2015]:

$$H_2CO_3 + H_2O \rightleftharpoons HCO_3^- + H_3O^+ \qquad pK_{a,1} = 3.76 \tag{2.27}$$

$$HCO_3^- + H_2O \rightleftharpoons CO_3^{2-} + H_3O^+ \qquad pK_{a,2} = 10.38 \tag{2.28}$$

The logarithmic acid constants are defined as the negative decadic logarithm of the dissociation constant ($pK_a = -\log_{10} K_a$). Figure 2.4 illustrates the equilibria of the carbonic acid in a diluted aqueous solution. The concentration ratios of the three compounds at equilibrium are plotted over the pH value of the solution for the given pK_a values. The pK_a values correspond to the pH value where the concentrations of the corresponding compound are equal. It is of particular importance that at low pH values, nearly no CO_3^{2-} is present in the solution. Since the presence of carbonate ions (CO_3^{2-}) is essential for calcium carbonate to precipitate, the pH value of the solution can be important to consider in processes of biomineralization.

Six different polymorphs of calcium carbonate exist: calcite, aragonite, vaterite, monohydrocalcite, ikaite, and amorphous calcium carbonate (ACC). The thermodynamical stability increases from ACC to calcite [El-Sheikh et al., 2013]. Three are anhydrous crystalline polymorphs: calcite, aragonite, and vaterite. Another phase is ACC, which is, according to the theory of Ostwald, the first phase to crystallize [Nebel, 2008], while Rodriguez-Blanco et al. [2011] claimed that the formation of crystalline calcium carbonate polymorphs during

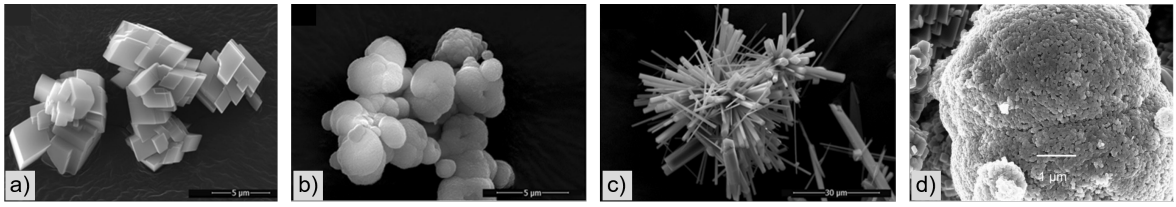

Figure 2.5: SEM images of calcium carbonate polymorphs: a) calcite; b) vaterite; c) aragonite; d) amorphous calcium carbonate (ACC). a)-c) Reprinted from Ševčík et al. [2018] with permission from Springer Nature, Copyright (2018). d) Reprinted from McDonald et al. [2022] with permission from Elsevier, Copyright (2022)

biomineralization often occurs via ACC, as a meta-stable precursor. Two main difference between the polymorphous phases of calcium carbonate are their crystal shapes and density, which are listed in Table 2.1 for calcite, aragonite, vaterite and ACC respectively.

Table 2.1: Calcium carbonate polymorphs

mineral	calcite	aragonite	vaterite	ACC
crystal shapes	rhombohedral	acicular	spherical	irregular
density [g/cm^3]	2.71	2.93	2.65	2.18

2.3.3 Induced calcium carbonate precipitation

As described in Chapter 1, biomineralization occurs in natural systems but can also be used as an engineering option with various objectives. Within the scope of this work, we focus on geoengineering applications relying on induced calcium carbonate precipitation (ICP). The driving process for ICP is the hydrolysis of urea. This irreversible and slow reaction can be enhanced by temperature and is referred to as thermally induced calcium carbonate precipitation (TICP). Moreover, urea hydrolysis can be catalyzed by the enzyme urease, which occurs in different plants [Krajewska, 2009]. Using plant-based urease - in this case, from jack beans - is referred to as enzymatically induced calcium carbonate precipitation (EICP). Other than plant-based urease, ureolytic bacteria, like *Sporosarcina pasteurii*, can also express the enzyme urease. ICP by ureolysis through urease produced by living bacteria is referred to as microbially induced calcium carbonate precipitation (MICP). In the work presented here, the focus is mainly on EICP. Urea ($CO(NH_2)_2$) reacts with water to form ammonia (NH_3) and inorganic carbon (Equation 2.29). Depending on the pH value, inorganic carbon dissolved in water occurs as carbonic acid (H_2CO_3), bicarbonate (HCO_3^-) and carbonate (CO_3^{2-}) (see

Equations 2.30, 2.27 and 2.28). Ammonia in aqueous solutions acts as a weak base by taking up a proton and producing hydroxide (Equation 2.31). In circumneutral environments, ammonium (NH_4^+) and bicarbonate are the dominant products of the hydrolysis [Mitchell et al., 2019]. Produced hydroxide (OH^-) increases the pH value and shifts the equilibrium towards carbonate ions. The additional presence of calcium ions allows calcium carbonate to precipitate (Equation 2.32). The overall reaction, including the hydrolysis of urea and calcium carbonate precipitation, is summarized in Equation 2.33.

$$CO(NH_2)_2 + 2\,H_2O \xrightarrow{\text{urease}} 2\,NH_3 + H_2CO_3 \tag{2.29}$$

$$H_2CO_3 \rightleftharpoons HCO_3^- + H^+ \rightleftharpoons {CO_3}^{2-} + 2\,H^+ \tag{2.30}$$

$$NH_3 + H_2O \rightleftharpoons NH_4^+ + OH^- \tag{2.31}$$

$$Ca^{2+} + CO_3^{2-} \rightleftharpoons CaCO_3\downarrow \tag{2.32}$$

$$CO(NH_2)_2 + 2\,H_2O + Ca^{2+} \rightleftharpoons 2\,NH_4^+ + CaCO_3 \tag{2.33}$$

Various factors can affect the reaction rate of ureolysis. For example, besides the activity of the urease enzyme and the concentration of urea, the pH value, the temperature, or the ammonium concentration (product) can influence the reaction. As described earlier, enzyme-catalyzed reactions can, in general, be described by the Michaelis-Menten equation (Equation 2.24), which describes the correlation of the reaction rate to the substrate (urea) concentration, dependent on the maximum reaction rate and the Michaelis-Menten constant. The maximum reaction rate and the Michaelis-Menten constant can depend, for instance, on enzyme activity, temperature, and pH value. These dependencies can be determined experimentally with batch experiments as, for example, done in Lauchnor et al. [2015]. The results of Lauchnor et al. [2015] indicated only a slight pH dependency using suspended bacterial cells as the source for urease. They concluded that neither the pH value in the range between 6-9 nor the ammonium concentration up to 0.19 mol/L significantly affect the ureolysis rate.

Feder et al. [2021] investigated the effect of temperature on the enzyme activity of plant-based urease in the range between 20°C and 80°C. On the one hand, increased temperatures usually accelerate the chemical reaction. However, on the other hand, elevated temperatures inactivate the enzyme urease. With a combined first-order urea hydrolysis and first-order enzyme inactivation model, they were able to describe the temperature dependency of the ureolysis. Hommel et al. [2020] successfully employed this first-order kinetic reaction model by implementing an Arrhenius-type equation in a numerical REV-scale model for EICP ap-

plications. The first-order reaction kinetics has also been used in this work to determine the reaction rate depending on the concentration of Jack Bean meal, the concentration of urea, and the temperature.

2.4 Determining permeability of porous media

Henry Darcy, a French engineer, published his most famous contribution in 1856. It includes the well-known law named after him, Darcy's law, already described in Section 2.2.2. Darcy's law can be demonstrated with a constant-head permeameter experiment, as illustrated in Figure 2.6. A column packed with a porous material, like sand, is connected to an inlet and outlet reservoir with constant hydraulic heads. The difference between the hydraulic head of the inlet and outlet, Δh, induce flow through the column. As already observed by Darcy [1856], under creeping flow conditions ($Re < 1$), the darcy velocity, v_f is proportional to the gradient of the hydraulic heads, approximated by $\frac{\Delta h}{\Delta s}$ and the proportionality constant can be defined as the hydraulic conductivity, k_f. With that, Darcy's Law can be formulated in its original form as:

$$v_\mathrm{f} = -k_\mathrm{f}\frac{\Delta h}{\Delta s}. \tag{2.34}$$

The hydraulic conductivity depends on the properties of the porous medium and of the fluid. In order to solely describe the property of the porous medium, the intrinsic permeability, k was introduced, which is defined as:

$$k = k_\mathrm{f}\frac{\mu}{\rho g}, \tag{2.35}$$

with the dynamic viscosity μ and the fluid density ρ. With that, the intrinsic permeability can be determined experimentally using a permeameter, as firstly described by Henry Darcy. For convenience we refer in the following to the intrinsic permeability simply as *the permeability*. Since the permeability is a proportionality constant, it can also be determined the other way around by applying a constant flow and measuring the gradient of the hydraulic head. Further experimental methods to determine the permeability exist, such as the falling-head method, where the hydraulic head of the inlet reservoir decreases over time. The sample's permeability can be calculated by relating the hydraulic head to the elapsed time. Directly in the field, the permeability can be estimated with pumping tests: A well extracts water at a controlled rate while the water tables in one or more observation wells are

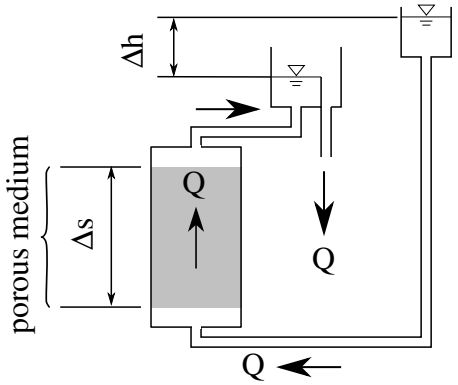

Figure 2.6: Schematic sketch of a permeameter experiment with a constant head and upwards flow

monitored. One can differentiate between long-term pumping tests, where stationary conditions are reached, and short-term tests, where instationary draw-downs of the water tables are evaluated. Besides these rather laborious determinations of the permeability, constitutive relationships exist, which allow deriving the permeability based on other quantities that are easier to determine.

2.4.1 Classical constitutive relationships for permeability

Generally, the exact pore geometry governs the permeability of a porous medium which is usually challenging and not practical to determine. Therefore, more accessible quantities, such as the characteristic grain sizes, porosity, or representative pore geometries, have been used to determine the permeability [Hommel et al., 2018]. In the following, we give a short overview of important constitutive relationships regarding the determination of the permeability, namely the relationship after *Hazen*, *Kozeny-Carman*, *Hagen-Poisseuille* and the *Cubic Law*.

Hazen:
Hazen [1892] proposed one of the first relationships to derive the hydraulic conductivity k_f of sand from the characteristic particle diameter d_{10} and an empirical constant c_H. The particle diameter, d_{10}, refers to the maximum diameter of the finest 10% of the grains in the considered sand.

$$k_\mathrm{f} = c_\mathrm{H} d_{10}^2 \tag{2.36}$$

Kozeny-Carman:
The porosity of a porous medium is relatively easy to determine and therefore used very

often to determine the permeability, especially in numerical REV-scale models. One of the most common porosity-permeability relationships is the Kozeney-Carman equation. It was originally published by Kozeny and modified by Carman [Kozeny, 1927, Carman, 1937]. Applying Darcy's law, the original equation can be reformulated to estimate permeability directly. In that case, the permeability k is a function of the characteristic particle diameter D_p, the sphericity Φ_s and the porosity ϕ (Equation 2.37). Equation 2.38 expresses the permeability with the tortuosity τ and the specific surface area S, instead of Φ_s and D_p [Hommel et al., 2018]:

$$k = \frac{\Phi_\mathrm{s}^2 D_\mathrm{p}^2}{180} \frac{\phi^3}{(1-\phi)^2} \tag{2.37}$$

$$k = \frac{\phi^3}{\tau(1-\phi)^2 S^2} \tag{2.38}$$

Hagen-Poisseuille:
Another method of estimating permeability is based on Hagen-Poisseuille's law. This law is valid for flow in small tubes and is often used to estimate the flow through individual pore throats in a network of pores. By assuming constant fluid density and a cylindrical geometry, Hagen-Poiseuille's law can be derived from the Stokes equation and relates the pore radius, r, the dynamic viscosity, μ, and pressure gradient, approximated by $\Delta p/L$, to the flow rate, Q. Consequently, the permeability of a capillary can be determined by additionally using Darcy's law and assuming a circular cross-sectional area, πr^2 [Hommel et al., 2018]:

$$Q = \frac{\pi r^4 \Delta p}{8\mu L} \quad \Rightarrow \quad k = \frac{r^2}{8}. \tag{2.39}$$

Cubic law:
Analogously to Hagen-Poisseuilles' law, the Cubic law can be derived from the Stokes equations for laminar flow between two plates with the width, w and the distance between the plates, h. Consequently, a representative permeability can be defined accordingly (Equation 2.40). The cubic law is commonly used to estimate permeabilities in fractured systems with highly conductive fractures [Hommel et al., 2018]:

$$Q = \frac{w h^3 \Delta p}{12\mu L} \quad \Rightarrow \quad k = \frac{h^2}{12} \tag{2.40}$$

2.4.2 Porosity-permeability relationships for altered porous media

Pore space alteration of porous media, as occurring during EICP or MICP, are usually concomitant with permeability alterations. For describing such processes, porosity-permeability relationships have proven to be practical for applying them in numerical REV-scale simulations. These relationships consequently follow the general equation:

$$\frac{k}{k_0} = f(\phi, \phi_0). \tag{2.41}$$

The alternating permeability, k normalized to its initial value, k_0 can be expressed as a function of the alternating porosity ϕ and its initial value, ϕ_0. A great variety of such relationships exist, which are summarized and evaluated in Hommel et al. [2018]. In the following, only a few of them, namely those of *Kozeny-Carman*, *Verma-Pruess* and the *power law* are presented which are considered to be the most relevant in terms of REV-scale modeling of EICP and MICP.

Kozeny-Carman type:
As described previously, the Kozeny-Carman equation was initially proposed for porous media of rigid and unchanged geometries and generally does not consider alterations of porosity due to precipitation. However, this relationship is frequently used to describe evolving pore spaces and permeabilities. The following equation can be derived to relate the alternating permeability to changes in the porosity, assuming the sphericity and characteristic particle diameter in Equation 2.37 to remain constant:

$$\frac{k}{k_0} = \frac{\phi^3(1-\phi_0)^2}{\phi_0^3(1-\phi)^2}, \tag{2.42}$$

Verma-Pruess type:
A slightly different approach has been proposed by Verma and Pruess [1988] which has been employed in numerical REV-scale modeling of MICP, for instance, in Ebigbo et al. [2012] and Hommel et al. [2016]. In this equation, the empirical parameter, critical porosity ϕ_{crit}, is introduced, which refers to the complete clogging of the porous medium below a specific porosity. It assumes that below a critical porosity, the remaining pores are not connected anymore, leading to the impermeability of the porous medium ($k = 0$). The exponent η is

another empirical parameter that, for instance, can be fitted to experimental data.

$$\frac{k}{k_0} = \begin{cases} \left(\frac{\phi-\phi_{\text{crit}}}{\phi_0-\phi_{\text{crit}}}\right)^{\eta} & \text{if } \phi > \phi_{\text{crit}} \\ 0 & \text{otherwise} \end{cases} \tag{2.43}$$

Power Law:
Another popular, relatively simple approach is the power-law relationship. It can be seen as a degenerated case of the Verma-Pruess type with a critical porosity of zero. According to Hommel et al. [2018] it can be considered as a default first choice when modeling transport through an evolving porous medium. Since it only has one parameter, η, that can be fitted to observations, it makes the resulting porosity-permeability relationships easily comparable to other studies. Despite its advantage, the power law is often criticized for not accurately representing complex processes that change the pore structures and necessarily remains overly simplistic.

$$\frac{k}{k_0} = \left(\frac{\phi}{\phi_0}\right)^{\eta} \tag{2.44}$$

2.5 Microfluidics

Microfluidics can be defined as the science investigating fluid interactions in microchannels and also refers to the technology to fabricate the corresponding flow cells, named micromodels or microfluidic cells. Micromodels generally have very small features, ranging from tens to hundreds of micrometers, thus, in the context of porous media, allowing for investigations on the pore scale (also see Section 2.1). Microfluidics provides an ideal platform for studying fundamental processes in various research fields, ranging from subsurface engineering applications to biological engineering technologies [Gerami et al., 2019, Karadimitriou and Hassanizadeh, 2012]. According to Gerami et al. [2019], the interest in microfluidics has been dated since the 1950s, while the publications on microfluidics in the last 30 years have rapidly increased. With increasing interest, the experimental setups and fabrication methods are continuously evolving. Some of the recent fabrication and visualization techniques are described in the following.

2.5.1 Fabrication of microfluidic cells

One of the first micromodels was reported by Chatenever and Calhoun [1952] who used two parallel transparent glass plates with a single layer of glass beads in between, shaping the pore space. Since then, the manufacturing processes of micromodels have been continuously improving. Materials for modern fabrications of micromodels mainly include silicon, glass, and polymeric materials using various manufacturing techniques, which are, for example, summarized in Karadimitriou and Hassanizadeh [2012] and Gerami et al. [2019]. In the following, a short overview of the ones considered the most relevant for this work, namely *optical lithography*, *wet etching* and *soft lithography* is given, while recent developments regarding the manufacturing of microfluidic devices that include *geomaterials* are presented.

Optical lithography:
Optical lithography, also known as photo-lithography, is a process mainly known from the semiconductor industry [Thompson, 1983], but also used for the fabrication of microfluidic cells regarding porous media research. The first step in a possible protocol for using optical lithography, as we have employed it, is to print the designed pore structure on a transparency referred to as the ”photomask”. Consequently, a silicon wafer coated with a thin photoresist layer is covered with this transparency before exposing it to UV light. The photomask only allows the UV light to interact with the transparent locations. Consequently, the photoresist reacts with the UV light and becomes insoluble when exposed to the appropriate developing agent. Therefore, the subsequent exposure to the developing agent dissolves the parts of the photoresist which were not exposed to UV light. As a result, the desired features of the pore structure remain. The completed wafer could either be used as a micromodel itself by covering it with a glass slide or could be used as a master mold for the production process of soft lithography.

Wet etching:
Wet etching is often used to fabricate micromodels made out of glass or other hard materials by etching the pore structure directly into the material. Photolithography can be used to cover the glass surface with a photoresist to establish a protective layer acting as a mask and limit etching to the desired locations. In the case of chemical, or wet etching in glass, an acid can be used as the etchant. The area covered with photoresist remains unaffected while the uncovered areas are etched during an acidic bath. During this process, the time of the bath determines the depth of the micromodel. Again, as a final step, a second glass slide with holes for the inlet and outlet is used to seal the micromodel.

Soft lithography:
Soft lithography is commonly used for the fabrication of polymer-based micromodels via replica molding [Xia and Whitesides, 1998, Duffy et al., 1998]. At first, a master mold needs to be created following the workflow of optical lithography, typically on a silicon wafer. From the resulting master mold, multiple micromodels can be fabricated out of various polymers. Poly-Di-Methyl-Siloxane (PDMS) is the most common polymer used in soft lithography, which requires the following manufacturing steps: The silicon wafer is put into a petri dish, and PDMS mixed with a curing agent is poured over it to create the PDMS slab with the pore structure. After degassing and thermal curing, the PDMS slide is gently removed from the wafer, and holes for the inlets and outlets are punched at the desired locations. Finally, the PDMS slide can be covered either by a PDMS slab or a glass slide. Soft lithography is a very cheap and convenient method since it allows to produce quickly, with little equipment, many replicates from one master mold. Especially for precipitation experiments, this is very useful since removing existing precipitates in such small micromodels can be very time-consuming or even impossible and therefore limits the reusability of a micromodel. Moreover, PDMS is transparent and therefore allows for easy visualization. Due to these advantages, it became prevalent in many disciplines, including the pore-scale study of biomineralization as reviewed in Section 1.3.

In this work, we utilized optical lithography to prepare the master mold and, consequently, soft lithography to prepare our micromodels. Additionally, we used glass micromodels from the company Micronit© which were manufactured by a wet etching process. Micromodels that include geomaterials have not been employed in this work. However, they might be of interest for future investigation. Therefore, some examples are summarized in the following.

Geomaterials:
Especially in the fields of hydrogeology and petroleum engineering, where surface chemistry becomes relevant, geomaterial microfluidics lately received increased attention [Gerami et al., 2019]. For example, some studies used natural materials, like coal or limestones, and applied laser etching on the surface to generate a fracture network [Gerami et al., 2017, Jiménez-Martínez et al., 2020]. Another interesting fabrication method was developed by Song et al. [2014]. They cut a calcite crystal into a thin wafer and coated it with beeswax. Subsequently, the desired pore structure was laser-etched into the wax before exposing the wafer to hydrochloric acid to etch the desired pore network into the calcite wafer. Another possibility for mimicking natural surface properties in artificially created porous media is functionalizing the surfaces. Wang et al. [2017] for example, coated the surface of a simple

glass micromodel with a layer of calcium carbonate by introducing silane to subsequently bind Ca^{2+} and CO_3^{2-} ions to the surface. Their method resulted in a uniform layer of $CaCO_3$ nanocrystals on the surface. Besides glass, also PDMS surfaces have been successfully functionalized with natural rock materials. Alzahid et al. [2018] developed a fabrication process to attach sandstone and carbonate onto the PDMS surface. Their method includes plasma treatment followed by the exposure of the mineral solution to bond the corresponding minerals to the PDMS surface. Nevertheless, all these described fabrication methods for geomaterial micromodels might still lead to discrepancies compared to natural systems, for example, regarding the surface roughness. However, these innovative methods still offer the possibility of generating micromodels representing natural surfaces more realistic than purely artificially created ones.

2.5.2 Measurements and visualization

Microfluidics inherently implies using tiny volumes, which require exact fluid control systems and very accurate measurement and detection devices. In some applications, pressure measurements are a crucial aspect to consider. On the one hand, some experiments require elevated pressures of several bars, for instance, to study supercritical CO_2. In such cases, the microfluidic setup needs to be capable of withstanding such high pressures. On the other hand, the precision of the sensors is essential to measure tiny pressure differences reliably, for example, to monitor permeability changes during pore space alterations. However, the corresponding experimental setup can be modified to accommodate the specific needs of the desired applications [Karadimitriou and Hassanizadeh, 2012]. A significant advantage in microfluidics is the possibility of highly time-resolved imaging during the experiments. Since micromodels are usually transparent, microfluidics provides an ideal platform for visual observation of flow at high temporal and spatial resolution [Gerami et al., 2019]. Some imaging techniques are shortly described in the following, including *transmitted and reflected light microscopy*, *confocal microscopy*, *micro particle image velocimetry* and *micro XRCT*.

Transmitted and reflected light microscopy:
Transmitted and reflected light microscopy are very often employed in microfluidics. In the case of partially transparent micromodels, where one side of them is opaque, imaging can only be done by reflection, thus reflected microscopy is commonly applied. For fully transparent micromodels, both the reflected as well as the transmitted light microscopy can

be employed [Gerami et al., 2019]. Besides standard, commercially available microscopes, Karadimitriou et al. [2012] built a customized optical setup, utilizing a beam splitter to enable the capturing of images with several cameras in order to visualize an elongated micromodel at a relatively high resolution. We have also used a slightly modified version of this setup in this work, as described in Weinhardt et al. [2021a].

Confocal and fluorescent microscopy:
Confocal microscopy can be used for 3D visualization of microfluidic experiments and allows for very high resolutions ($< 1\mu\text{m/pixel}$) [Gerami et al., 2019]. For example Datta et al. [2013] used confocal microscopy for a 3D visualization of a micromodel packed with glass beads. Especially regarding microbiological investigations, confocal laser scanning microscopy is relatively popular since it allows for example to visualize a green fluorescent protein, expressed by engineered bacteria, as described in Connolly et al. [2013]. A similar method has also been applied in the work of Zambare et al. [2020] to identify fluorescent calcite crystals during biomineralization.

Micro particle image velocimetry (micro PIV):
Micro PIV is an optical diagnostic technique to derive velocity fields by tagging the fluid with tracer particles. A particle's average displacement during a given time interval is obtained by the cross-correlation between two image frames. For applying PIV in microfluidics usually fluorescent particles are used, which are excited by a pulsed laser that delivers an intense illumination over a very short duration [Gerami et al., 2019]. de Winter et al. [2021] for example, used confocal laser scanning microscopy to obtain the three-dimensional velocity profile within a PDMS micromodel.

Micro X-ray computer tomography (micro XRCT):
Another non-destructive imaging technique is micro XRCT which allows 3D visualization of micromodels using X-rays. In contrast to confocal microscopy, for example, the medium does not necessarily need to be transparent to visible light. Therefore, in the case of biomineralization, micro XRCT allows for a 3D visualization of calcium carbonate precipitates. However, acquiring three-dimensional images of reasonable quality requires relatively long scanning times which limits temporal resolution. In our work, we used three-dimensional images of a microfluidic cell, which was scanned after the precipitation process, using the micro X-ray computed tomography device developed by Ruf and Steeb [2020].

3 Objectives and Summaries of the Contributions

In this chapter, the overall research goal is presented and the three contributions are summarized. Figure 3.1 illustrates the context of this work, including the motivation, the research goal, and the link between the individual contributions. As outlined in Chapter 1, the overarching goal of this work is mainly aimed at geotechnical applications of biomineralization where REV-scale modeling is an essential tool to assist, plan and optimize engineering field-scale projects of EICP and MICP. These REV-scale models inherently rely on porosity-permeability relationships for predicting and assessing the performance of applications. Both, the porosity and the permeability are averaged quantities representing pore morphology alteration and their hydraulic effects on the REV-scale. However, it is the pore-scale where processes occur and from where we expect to derive new insights relevant for REV-scale modeling. Therefore, we can formulate the overarching goal as the following:

Research goal:

Identification of pore-scale characteristics during EICP treatment, that are important to consider when modeling on the REV scale, with the focus on porosity and permeability.

In order to achieve this goal, we identified microfluidics as a very promising experimental technique. Therefore, as the first step, a solid experimental setup and procedure needed to be elaborated, which we addressed in the first contribution. Reliable pressure measurements synchronized with optical microscopy and their 3D interpretations are the key points we considered. The elaborated workflow and generated data consequently set the basis for the other two contributions. In the second contribution, we analyzed experimental data obtained from the first contribution concerning crystal growth and its interaction with flow and transport. In a combined experimental and numerical study together with Lars von Wolff, who developed

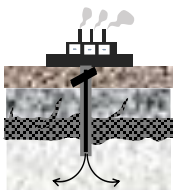

REV-scale modeling as an important tool for assisting and planning of field applications of biomineralization

porosity-permeability relationships as an inevitable, but not yet fully understood constitutive relation for REV-scale models

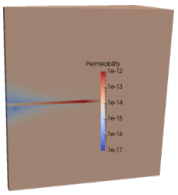

Remaining uncertainty for the description of porosity and permeability alterations

Contribution 1:
Experimental Methods and Imaging for Enzymatically Induced Calcite Precipitation in a microfluidic cell

Contribution 2:
Investigation of Crystal Growth in Enzymatically Induced Calcite Precipitation by Micro-Fluidic Experimental Methods and Comparison

Contribution 3
Spatio-temporal distribution of precipitates and mineral phase transition during biomineralization

Figure 3.1: Structure and objectives of this dissertation.

a mathematical model for EICP on the pore-scale, we drew essential conclusions regarding the growth of individual precipitates during constant flow conditions. Finally, further experiments have been performed with another, more realistic pore structure and varying injection scenarios in the third contribution. We identified further processes during biomineralization that affect the development of permeability due to the change in pore morphology. The objectives and findings of the individual contributions are summarized more comprehensively in the following.

Contribution 1: Experimental Methods and Imaging for Enzymatically Induced Calcite Precipitation in a microfluidic cell

Microfluidic experiments have become increasingly popular lately for investigating various aspects of biomineralization (also see Section 1.3). Wang et al. [2019a], Zambare et al. [2020]

and Kim et al. [2020] showed successfully the use of transparent microfluidic chips made out of Polydimethylsiloxane (PDMS) or glass to characterize the precipitation behavior on the pore-scale for MICP and EICP, respectively. These pioneering studies proved the general applicability of using microfluidics to provide insights into the bacterial distribution, the kinetics of precipitation, and the time-dependent mineralogy of calcium carbonate. However, since their work did not focus on quantifying the hydraulic changes due to the precipitation, there was no need for pressure monitoring in their experimental setups. Furthermore, in a prior study, we demonstrated that determining the permeability for microfluidic experiments is not trivial. Comparing experimental results to various pore-scale simulations, we demonstrated that the effect of the inlet and outlet channels could not be neglected [Wagner et al., 2021]. This bias would become even more dominant during precipitation. Pursuing our overall goal, we need to consider this when elaborating a new experimental setup and workflow that enables us to reliably monitor and quantify the pore space alterations and the corresponding hydraulic responses. So in Weinhardt et al. [2021a], we present experimental methods for investigating the time-resolved effects of growing precipitates on porosity and permeability on the pore-scale using microfluidic flow cells made out of PDMS. Two datasets were published along with this contribution: Weinhardt et al. [2021b] includes the images obtained from optical microscopy, synchronized with pressure measurements, and Vahid Dastjerdi et al. [2021] contains the micro XRCT scan of one micromodel at its final state, after the precipitation process. The experimental workflow includes the design and manufacturing process of the PDMS-based microfluidic cells, a suitable injection strategy, and appropriate imaging techniques.

First of all, the microfluidic cell was designed to measure the pressure drop across the porous domain of the flow cell without being influenced by precipitation in the inlet and outlet distribution channels. We implemented two additional pressure channels, one located directly at the beginning of the porous domain and one on the outlet, respectively. During a continuous injection of the reactive solutions, we can reliably measure the pressure drop across the porous domain without being strongly influenced by precipitates before or after the domain. The design of the pore structure itself was kept very simple: four pore bodies connected by pore throats. Thus, it is not very representative for a porous medium but optimal for demonstrating and validating the workflow, which consists of three stages: a) an initial permeability measurement with deionized water at various flow rates, b) a continuous coinjection of the reaction solutions to induce precipitation and c) a final permeability measurement again with deionized water. Despite minor deviations due to a temporal shift between stage b) and

c) where precipitation could continue, we could ”validate” our temporal pressure measurements and the resulting permeability estimations. Regarding the observation of pore space alteration, we used two imaging techniques, namely optical microscopy and subsequent micro XRCT for a 3D visualization of the precipitates at the final stage of the experiment. Optical microscopy is an inexpensive method that allows for high temporal resolutions, though it only captures the 2D projections of the three-dimensional precipitates. However, the 3D scan of the precipitates at their final state allows us to find appropriate shape assumptions to derive volume changes from 2D projections.

In brief, the elaborated workflow enables us to monitor and evaluate both the porosity and permeability - highly time-resolved and reliably during the process of EICP.

Contribution 2: Investigation of Crystal Growth in Enzymatically Induced Calcite Precipitation by Micro-Fluidic Experimental Methods and Comparison with Mathematical Modeling

The successful application of EICP relies on the complex interplay between solute transport, ureolysis, and precipitation. The flow conditions determine the transport of chemical substances. The continuous precipitation reaction associated with a change in pore morphology, in turn, changes the local flow field. Therefore, biomineralization during a continuous inflow of reactants is a strongly coupled process which we address in our second contribution by combining microfluidic experiments and numerical pore-scale simulation. In microfluidic experiments, measuring local concentrations of solutes is highly challenging due to the tiny dimensions and minuscule volumes, at least with conventional methods. Therefore, the second contribution is joint work with Lars von Wolff, who developed a phase-field approach for modeling crystal growth on the pore-scale. It couples the Navier-Stokes equations and the solute transport equation with the Cahn-Hillard evolution. The numerical model allows incorporating conceptual ideas for processes and mechanisms to improve process understanding of the complex interactions of flow, transport, and pore space alteration due to precipitation. Complementing experimental microfluidic investigations with numerical simulations allows us to draw significant conclusions. In von Wolff et al. [2021], we address how the transport processes, determined by fluid dynamics and the chemical reactions, influence crystal growth during EICP. We used the experimental data obtained from the first contribution [Weinhardt et al., 2021b] and analyzed the growth of the individual precipitates dependent on their location within the pore structure.

We found that the growth is strongly dependent on the local concentrations, determined by the local flow conditions. We observed during constant flow boundaries in both, the experiments and the simulation results that the precipitates tend to grow towards the upstream side, where the supply of reactants is higher than on the downstream side of the precipitate. The exact pore geometry determines flow in porous media, thus resulting in locally varying velocities. In our simplified geometry, consisting of four pore bodies connected by pore throats, velocities are higher in the throats compared to the bodies. We noted that the lower velocity in the pore bodies led to a less pronounced growth towards the upstream direction compared to crystals within the throats. We concluded that the interplay between the advective transport around the individual aggregates and the diffusion towards the surface of existing precipitates governs the growth of the precipitates. Moreover, we found a correlation between the growth rate and the magnitude of the flow velocities. At high velocities, the growth is faster, leading to increased growth in the pore throats and towards the center of the cell.

In brief, we identified mechanisms in the EICP-related growth of precipitates within this combined experimental and numerical approach. This work contributes to a better understanding of the processes on the pore-scale, and we demonstrated that locally varying flow velocities, not resolved on the REV-scale, affect the precipitation behavior.

Contribution 3: Spatio-temporal distribution of precipitates and mineral phase transition during biomineralization affect porosity-permeability relationships

Calcium carbonate precipitation is a complex combination of nucleation, crystal growth, and polymorphic transformations. Depending on the inflow conditions and the initial pore structure, we expect, besides the mineral phase transition also, variations in the spatial distribution of the precipitates. Mineral phase transition and varying spatial distributions of precipitates can affect the hydraulic responses or, in terms of the REV-scale parameters, the permeability. However, it is the pore-scale where we need to investigate these phenomena to conclude on REV-scale properties. The third contribution [Weinhardt et al., 2022a] builds on the first contribution. We used the existing datasets and employed the established workflow to perform further experiments with a more realistic pore structure. The third contribution comprehends the analysis of microfluidic experiments using two different pore structures, a simple *quasi-1D-structure* and a more complex *quasi-2D-structure* and two different injection strategies, a constant and a step-wise reduced inflow condition. We were able to

identify relevant mechanisms during the EICP-treatment and drew meaningful conclusions about porosity-permeability relationships.

In the *quasi-1D-structure*, consisting of linearly aligned pore bodies connected by pore throats, the change of permeability is dominated by the location of the precipitates rather than by the overall porosity reduction. Consequently, when trying to match porosity-permeability data to a power-law relationship, the exponents are very high (30-100) and difficult to determine reliably. In contrast, for the *quasi-2D-structure* this local effect of a single pore-throat clogging seems to have less pronounced effects on the overall permeability, which results in smoother relationships and smaller exponents when fitted to a power-law (3-7). Furthermore, at the beginning of the precipitation process, mainly small irregularly shaped precipitates (hypothesized as ACC) formed and are likely to be transported with the flow. They temporally clog pathways resulting in a high permeability reduction at early times and power-law exponents of around 10. In later stages, ACC seems to transform to vaterite or calcite. Consequently, the resulting slope of the porosity-permeability relationship reduces, leading to fitted exponents of the power-law between 3 and 5. Interestingly, preferential flow paths can form and appear to persist under continuous flow conditions, while step-wise decreased flow boundary conditions can mitigate this effect. However, preferential flow paths result in a heterogeneous precipitation pattern identified on the pore-scale, leading to difficulties for the correct definition of an REV. In this case, dual-porosity concepts could be justified when modeling on the REV-scale.

To sum up, in this contribution, we identified that the initial pore structure, the imposed boundary condition, and mineral phase transition could affect the spatial and temporal distribution of the precipitates, which can lead to difficulties describing their effects on the REV-scale by porosity-permeability relationships.

4 Conclusions, Limitations and Outlook

This chapter presents the main conclusions of this work and consequently the limitations of our methods. Finally, possible perspectives for future investigations are presented.

Conclusions

This dissertation addresses the current gap of knowledge regarding the hydraulic effects of pore space alterations during biomineralization in porous media. We enhanced the process understanding of EICP treatment by identifying important pore-scale characteristics focusing on REV-scale porosity-permeability relationships. Here, we want to emphasize the evolution and persistence of preferential flow paths and their relevance for the permeability evolution during EICP treatment. As presented in Weinhardt et al. [2022a], the applied boundary conditions seem to play a crucial role in the development of preferential flow paths. Such paths directly impact the permeability and its temporal evolution, which, based on our observations, are also related to the polymorphous nature of calcium carbonate. Amorphous calcium carbonate (ACC) has been reported to be a precursor during calcium carbonate precipitation and will eventually, as time passes, be transformed into more stable crystalline phases like vaterite or calcite. Particularly in the early stages of the precipitation process, we observed mainly small, irregularly shaped precipitates, which were likely to be transported with the flow. We assume them to be ACC implying that they have a lower density than vaterite and calcite. The transport of these precipitates may lead to temporary clogging of pathways and, depending on the boundary condition, may lead to the evolution of preferential flow paths. Our presented work concludes that a boundary-dependent evolution of preferential flow paths concomitant with polymorphous transformations can influence the REV-scale porosity-permeability relationships during EICP treatment. From a modeler's perspective, this may raise concerns

regarding the applicability of conventional porosity-permeability relationships, above all, the simple power-law relationship. According to Hommel et al. [2018], power-law relationships are a default first choice in REV-scale modeling approaches and more complex laws are only justified where detailed process knowledge is available. Therefore, the question arises, whether or not our results provide the necessary detailed process knowledge to justify and derive more complex approaches.

The answer to that question is *Yes* and *No*: First, the time-dependence and the resulting heterogeneous precipitation pattern as a function of the boundary conditions complicate the derivation of representative porosity-permeability relationships. One possible way to incorporate the evolution of preferential flow paths in REV-scale descriptions would imply the use of dual-porosity approaches, as exemplary demonstrated in [Weinhardt et al., 2022a]. However, at the current state of research, we cannot claim that we will be capable of deriving definite concepts with the presented approach since it is not yet clear to what extent the preferential flow paths are attributed to the inherent bias of the quasi-2D setup. Clarifying that would require additional experiments with higher spatial complexities, for example, in larger, more realistic porous media, like sand or glass bead columns. These limitations regarding the microfluidic experiments and their applicability to realistic field applications are discussed more comprehensively in the following.

Limitations

As presented in this work, with microfluidics and their numerical interpretation we could draw essential conclusions on the relevant mechanisms. However, microfluidics as we employed it might raise concerns regarding the applicability of the findings to real engineering applications. The artificially created porous media have two essential differences compared to realistic porous media, thus implicitly causing limitations. The most significant differences are related to the *surface properties* (glass/PDMS vs. natural rocks or soils) and the reduced *hydrodynamic complexity* (quasi-2D vs. actual 3D). These limitations are discussed in the following.

Surface Properties:
Microfluidics generally requires transparent flow cells to visualize the experiments with optical microscopy, which is why microfluidic cells made of glass or PDMS are by now prevalent. The artificially created microfluidic cells usually consist of one type of material with

homogeneous surface properties. On the one hand, this is an essential feature of microfluidic investigations since it generally allows for systematic studies under well-controlled conditions without being heavily influenced by uncontrolled and unknown local variations. On the other hand, the surface properties of natural porous media may differ from artificially created porous media and might likely be rather heterogeneous.

Hydrodynamic complexity:
The other substantial difference between the artificially created and natural porous media is the hydrodynamic complexity governed by the pore geometry. Again, for visualization purposes, the quasi-2D artificially created porous media in microfluidics are optimal but represent a simplified system compared to actual natural porous media. Even though we compared pore structures of different complexities in the third contribution, the bias caused by the bottom and top surface of the micromodels remains, regardless of the actual complexity of the internal design. The additional surfaces of the bottom and top layer of the micromodel potentially provide additional nucleation sites where precipitates can start growing, leading to a typical and unavoidable artifact in microfluidics regarding precipitation experiments. Moreover, the bottom and top surfaces of the microfluidic cells restrict the flow to a quasi-2D geometry and introduce additional resistance to the flow. In pore-scale modeling, the additional friction can be accounted for by introducing an additional drag term. However, natural porous media usually show a more complex pore morphology due to their additional dimension. Especially with regards to deriving porosity-permeability relationships, these, up to now, unavoidable differences between natural and artificial porous media need to be considered when concluding from microfluidic experiments to actual applications in the field.

In summary, on the one hand, we are convinced that the increased complexity of a realistic porous medium concerning hydrodynamic effects and varying surface properties will qualitatively not lead to fundamental differences. Therefore, from the perspective of a fundamental process understanding, we identified and quantified relevant mechanisms that are also relevant to consider in realistic porous media. However, on the other hand, we cannot claim that we will be capable of deriving functional and all-encompassing porosity-permeability relationships with microfluidic investigations. It is even questionable if such a ”magical formula” actually exists since local pore space alteration may depend on various factors which are hard to quantify and control. However, to deliver process understanding and to better explain observations in the field, with this elaborated workflow, we have been and will be able to shed light onto processes on the pore-scale leading to variations of average quantities in macroscopic considerations. Therefore, this work builds the basis for further investigations

to better understand the relevant mechanisms regarding porosity and permeability alterations by induced calcium carbonate precipitation.

Outlook

Potential perspectives include further pore-scale simulations based on the comprehensive datasets generated during this work, the extension of the established workflow with additional experimental techniques, and more complex pore structures using microfluidic chips (quasi-2D) or column (3D) experiments. Moreover, extending the work from EICP to MICP experiments can be an exciting perspective for future work since, in contrast to EICP, MICP additionally involves bacterial activity during the experiments.

Pore-scale simulations based on the provided datasets:
The central part of this work are the microfluidic experiments and their interpretations. Besides the presented scientific articles, the comprehensive experimental datasets which were published and well documented in DaRUS, the data repository of the University of Stuttgart, are essential contributions to the scientific community [Weinhardt et al., 2021b, 2022b, Vahid Dastjerdi et al., 2021]. In von Wolff et al. [2021], we showed the enormous benefit of combining experimental and numerical investigations, as described in the previous chapter. Since Weinhardt et al. [2022a] was a purely experimental study, additional numerical analysis based on the published datasets could provide new insights. Different modeling approaches could be compared and validated with the experimental datasets. The dataset [Weinhardt et al., 2022b] allows for studying various pore space configurations by providing time-resolved optical microscopy images along with differential pressure measurements during an evolving pore morphology. In addition, the processed images, which can directly be used to generate suitable computational grids for different simulation approaches, are given in the dataset. On the one hand, relatively simple steady-state approaches of single-phase flow could be employed to calculate the velocity distribution inside the pore structure, similar to what we did in Wagner et al. [2021] for one homogeneous geometry. A promising approach to efficiently simulating microfluidic experiments is the pseudo-3D approach, described in Section 2.2.2, which accounts for the friction caused by the bottom and top of the cell by implementing an additional drag term dependent on the aperture. This approach could be compared to fully 3D resolved Stokes simulations concerning the accuracy and computational effort for the case that the apertures in the domain vary locally depending on the volume of the precipitates. On the other hand, more complex approaches, like reactive transport models that allow for

a changing pore morphology, can be applied analogously to what we did in von Wolff et al. [2021]. Due to the larger domain, this would require highly efficient and parallelized solution strategies to be capable of modeling the entire domain.

Extensions of the experimental methods:
A reasonable extension to the presented workflow could be using micro particle image velocimetry (micro PIV) to resolve the local velocity field inside the pore structure. Although this seems to be a promising technique, especially when comparing experimental results to numerical pore-scale simulations, this method comes with an inherent challenge for applying it to EICP or MICP experiments. It requires injecting fluorescent particles into the micromodel. These particles could act as nucleation sites or could attach to existing precipitates and therefore introduce bias to the system. Furthermore, calcite's autofluorescent nature could also interfere with the micro PIV measurements. On the contrary, one could take advantage of the fluorescent signal of calcite to differentiate it from other, non-fluorescent polymorphs, like ACC. Regarding the differentiation and identification of the various polymorphs, one could additionally apply Raman spectroscopy to differentiate them.

More complex pore structures and surface properties:
As discussed earlier, the artificially created porous media we used are quasi-2D media with relatively homogeneous pore structures and surface properties. This limited hydrodynamic complexity and the homogenous surface of the microfluidic cells can be seen as a weak point concerning the comparability to realistic porous media. However, the surface of PDMS for instance can be modified (see Section 2.5). Also, the placing of sand particles into a microfluidic cell has been lately tested [Xiao et al., 2022]. Incorporating these innovative techniques into the existing workflow would allow studying the influence of different and locally varying surface properties on biomineralization in porous media. Furthermore, the system's hydrodynamic complexity could be increased by designing and employing different pore structures such as fractured porous media. Fractured porous media could be exciting to study, especially with the background of applying EICP or MICP for leakage remediation since preferential flow paths, in the form of fractures would very likely already exist. The imposed boundary conditions could then be evaluated regarding their optimization to seal fractures. For studying the sealing of fractures in cases where the interaction between the fractures and the porous medium does not play a significant role, the quasi-2D nature of the microfluidic cells is ideal. However, in other cases regarding biomineralization in porous media, the bias due to the top and bottom surfaces remains. To overcome the bias of the micromodels, we would need to change from quasi-2D to actual 3D samples. As a first step,

sintered glass beads columns seem to be promising. Sintered glass beads can ensure a rigid solid matrix that will not change during the precipitation. This allows for systematic analysis when performing time-resolved tomographic imaging techniques, like nuclear magnetic resonance or micro XRCT measurements. Another step towards realistic porous media could potentially be the use of sand columns or sandstone cores with either homogeneous or heterogeneous characteristics, possibly with fractures. These options would add complexity to the system and be closer to real applications. However, we have to be aware that the additional complexity of the experiments inherently limits the precision and reproducibility of data acquisition and complicates the interpretations of the obtained data. Therefore, in our opinion, more complex column experiments do not replace microfluidic experiments, as we have employed them, but complement them.

MICP experiments:
This work focused on EICP, and we extracted the urease enzyme from Jack Bean meal prior to the microfluidic experiments. In contrast, MICP also includes bacterial activity during the treatment, leading to potential differences, as bacteria could serve as additional nucleation sites during the calcium carbonate precipitation. The established experimental workflow could also be employed to study MICP. With that, potential differences between these techniques could be identified. This opens the door for understanding similarities as well as describing effects of MICP and EICP on the pore-scale geometry and on upscaled REV-scale parameters.

Bibliography

J. D. Ahlstrom. Chapter 1 - Molecular Organization of Cells. In *Principles of Regenerative Medicine*, pages 3–18. Academic Press, San Diego, 2nd edition, 2011. ISBN 978-0-12-381422-7. doi: 10.1016/B978-0-12-381422-7.10001-X.

A. Al Qabany, K. Soga, and C. Santamarina. Factors Affecting Efficiency of Microbially Induced Calcite Precipitation. *Journal of Geotechnical and Geoenvironmental Engineering*, 138(8):992–1001, 2012. doi: 10.1061/(asce)gt.1943-5606.0000666.

J. F. Allen. A proposal for formation of Archaean stromatolites before the advent of oxygenic photosynthesis. *Frontiers in Microbiology*, 7:1784, 2016. doi: 10.3389/fmicb.2016.01784.

Y. A. Alzahid, P. Mostaghimi, A. Gerami, A. Singh, K. Privat, T. Amirian, and R. T. Armstrong. Functionalisation of Polydimethylsiloxane (PDMS)- Microfluidic Devices coated with Rock Minerals. *Scientific Reports*, 8:15518, 2018. doi: 10.1038/s41598-018-33495-8.

R. M. Andrew. Global CO_2 emissions from cement production, 1928–2018. *Earth System Science Data*, 11(4):1675–1710, 2019. doi: 10.5194/essd-11-1675-2019.

J. Bear. *Dynamics of fluids in porous media*. American Elsevier Publications, New York, 1972. ISBN 0486656756.

H. Bisswanger. *Enzyme kinetics: principles and methods*. Wiley-VCH, Weinheim, 3rd edition, 2017. ISBN 9783527342518.

P. C. Carman. Fluid Flow through Granular Beds. *Transactions of the Institution of Chemical Engineers*, 15:150–166, 1937.

A. Chatenever and J. C. Calhoun. Visual Examinations of Fluid Behavior in Porous Media - Part I. *Journal of Petroleum Technology*, 4(6):149–156, 1952. doi: 10.2118/135-g.

J. Connolly, M. Kaufman, A. Rothman, R. Gupta, G. Redden, M. Schuster, F. Colwell, and R. Gerlach. Construction of two ureolytic model organisms for the study of microbially induced calcium carbonate precipitation. *Journal of Microbiological Methods*, 94(3):290–299, 2013. doi: 10.1016/j.mimet.2013.06.028.

A. B. Cunningham, H. Class, A. Ebigbo, R. Gerlach, A. J. Phillips, and J. Hommel. Field-scale modeling of microbially induced calcite precipitation. *Computational Geosciences*, 23(2):399–414, 2019. doi: 10.1007/s10596-018-9797-6.

M. O. Cuthbert, M. S. Riley, S. Handley-Sidhu, J. C. Renshaw, D. J. Tobler, V. R. Phoenix, and R. Mackay. Controls on the rate of ureolysis and the morphology of carbonate precipitated by S. Pasteurii biofilms and limits due to bacterial encapsulation. *Ecological Engineering*, 41:32–40, 2012. doi: 10.1016/j.ecoleng.2012.01.008.

M. O. Cuthbert, L. A. McMillan, S. Handley-Sidhu, M. S. Riley, D. J. Tobler, and V. R. Phoenix. A field and modeling study of fractured rock permeability reduction using microbially induced calcite precipitation. *Environmental Science and Technology*, 47(23): 13637–13643, 2013. doi: 10.1021/es402601g.

H. P. G. Darcy. *Les Fontaines publiques de la ville de Dijon: Exposition et application des principes 'a suivre et des formules 'a employer dans les questions de distribution d'eau, etc*. V. Dalmont, Paris, 1856.

S. S. Datta, H. Chiang, T. S. Ramakrishnan, and D. A. Weitz. Spatial fluctuations of fluid velocities in flow through a three-dimensional porous medium. *Physical Review Letters*, 111(6):064501, 2013. doi: 10.1103/PhysRevLett.111.064501.

D. A. de Winter, K. Weishaupt, S. Scheller, S. Frey, A. Raoof, S. M. Hassanizadeh, and R. Helmig. The Complexity of Porous Media Flow Characterized in a Microfluidic Model Based on Confocal Laser Scanning Microscopy and Micro-PIV. *Transport in Porous Media*, 136(1):343–367, 2021. doi: 10.1007/s11242-020-01515-9.

J. T. Dejong, K. Soga, E. Kavazanjian, S. Burns, L. A. Van Paassen, A. Al Qabany, A. Aydilek, S. S. Bang, M. Burbank, L. F. Caslake, C. Y. Chen, X. Cheng, J. Chu, S. Ciurli, A. Esnault-Filet, S. Fauriel, N. Hamdan, T. Hata, Y. Inagaki, S. Jefferis, M. Kuo, L. Laloui, J. Larrahondo, D. A. Manning, B. Martinez, B. M. Montoya, D. C. Nelson, A. Palomino, P. Renforth, J. C. Santamarina, E. A. Seagren, B. Tanyu, M. Tsesarsky, and T. Weaver. Bio-

geochemical processes and geotechnical applications: Progress, opportunities and challenges. *Geotechnique*, 63(4):143–157, 2013. doi: 10.1680/bcmpge.60531.014.

J. L. Drake, T. Mass, J. Stolarski, S. Von Euw, B. van de Schootbrugge, and P. G. Falkowski. How corals made rocks through the ages. *Global Change Biology*, 26(1):31–53, 2020. doi: 10.1111/gcb.14912.

D. C. Duffy, J. C. McDonald, O. J. Schueller, and G. M. Whitesides. Rapid prototyping of microfluidic systems in poly(dimethylsiloxane). *Analytical Chemistry*, 70(23):4974–4984, 1998. doi: 10.1021/ac980656z.

A. Ebigbo, A. Phillips, R. Gerlach, R. Helmig, A. B. Cunningham, H. Class, and L. H. Spangler. Darcy-scale modeling of microbially induced carbonate mineral precipitation in sand columns. *Water Resources Research*, 48:W07519, 2012. doi: 10.1029/2011WR011714.

S. M. El-Sheikh, S. El-Sherbiny, A. Barhoum, and Y. Deng. Effects of cationic surfactant during the precipitation of calcium carbonate nano-particles on their size, morphology, and other characteristics. *Colloids and Surfaces A: Physicochemical and Engineering Aspects*, 422:44–49, 2013. doi: 10.1016/j.colsurfa.2013.01.020.

E. J. Espinosa-Ortiz, B. H. Eisner, D. Lange, and R. Gerlach. Current insights into the mechanisms and management of infection stones. *Nature Reviews Urology*, 16(1):35–53, 2019. doi: 10.1038/s41585-018-0120-z.

M. J. Feder, A. Akyel, V. J. Morasko, R. Gerlach, and A. J. Phillips. Temperature-dependent inactivation and catalysis rates of plant-based ureases for engineered biomineralization. *Engineering Reports*, 3:e12299, 2021. doi: 10.1002/eng2.12299.

A. Gerami, R. T. Armstrong, B. Johnston, M. E. Warkiani, N. Mosavat, and P. Mostaghimi. Coal-on-a-Chip: Visualizing Flow in Coal Fractures. *Energy and Fuels*, 31(10):10393–10403, 2017. doi: 10.1021/acs.energyfuels.7b01046.

A. Gerami, Y. Alzahid, P. Mostaghimi, N. Kashaninejad, F. Kazemifar, T. Amirian, N. Mosavat, M. Ebrahimi Warkiani, and R. T. Armstrong. Microfluidics for Porous Systems: Fabrication, Microscopy and Applications. *Transport in Porous Media*, 130(1):277–304, 2019. doi: 10.1007/s11242-018-1202-3.

N. Hamdan and E. Kavazanjian. Enzyme-induced carbonate mineral precipitation for fugitive dust control. *Geotechnique*, 66(7):546–555, 2016. doi: 10.1680/jgeot.15.P.168.

A. Hazen. Some physical properties of sands and gravels, with special reference to their use in filtration. In *24th Annual Rep, Massachusetts State Board of Health Pub. Doc. No. 34:539556*, 1892.

R. Helmig. *Multiphase flow and transport processes in the subsurface : a contribution to the modeling of hydrosysteme*. Springer, Heidelberg, 1997. ISBN 3540627030.

T. Hobbs, L. N. Schultz, E. G. Lauchnor, R. Gerlach, and D. Lange. Evaluation of Biofilm Induced Urinary Infection Stone Formation in a Novel Laboratory Model System. *Journal of Urology*, 199(1):178–185, 2018. doi: 10.1016/j.juro.2017.08.083.

J. Hommel, E. Lauchnor, A. Phillips, R. Gerlach, A. B. Cunningham, R. Helmig, A. Ebigbo, and H. Class. A revised model for microbially induced calcite precipitation: Improvements and new insights based on recent experiments. *Water Resources Research*, 51(5):3695–3715, 2015. doi: 10.1002/2014WR016503.

J. Hommel, E. Lauchnor, R. Gerlach, A. B. Cunningham, A. Ebigbo, R. Helmig, and H. Class. Investigating the Influence of the Initial Biomass Distribution and Injection Strategies on Biofilm-Mediated Calcite Precipitation in Porous Media. *Transport in Porous Media*, 114(2):557–579, 2016. doi: 10.1007/s11242-015-0617-3.

J. Hommel, E. Coltman, and H. Class. Porosity-Permeability Relations for Evolving Pore Space: A Review with a Focus on (Bio-)geochemically Altered Porous Media. *Transport in Porous Media*, 124(2):589–629, 2018. doi: 10.1007/s11242-018-1086-2.

J. Hommel, A. Akyel, Z. Frieling, A. J. Phillips, R. Gerlach, A. B. Cunningham, and H. Class. A numerical model for enzymatically induced calcium carbonate precipitation. *Applied Sciences*, 10(13):4538, 2020. doi: 10.3390/app10134538.

J. Jiménez-Martínez, J. D. Hyman, Y. Chen, J. W. Carey, M. L. Porter, Q. Kang, G. Guthrie, and H. S. Viswanathan. Homogenization of Dissolution and Enhanced Precipitation Induced by Bubbles in Multiphase Flow Systems. *Geophysical Research Letters*, 47: e2020GL087163, 2020. doi: 10.1029/2020GL087163.

S. Joshi, S. Goyal, A. Mukherjee, and M. S. Reddy. Microbial healing of cracks in concrete: a review. *Journal of Industrial Microbiology and Biotechnology*, 44(11):1511–1525, 2017. doi: 10.1007/s10295-017-1978-0.

H. Jung and C. Meile. Pore-Scale Numerical Investigation of Evolving Porosity and Permeability Driven by Biofilm Growth. *Transport in Porous Media*, 139(2):203–221, 2021. doi: 10.1007/s11242-021-01654-7.

N. K. Karadimitriou and S. M. Hassanizadeh. A Review of Micromodels and Their Use in Two-Phase Flow Studies. *Vadose Zone Journal*, 11:vzj2011.0072, 2012. doi: 10.2136/vzj2011.0072.

N. K. Karadimitriou, V. Joekar-Niasar, S. M. Hassanizadeh, P. J. Kleingeld, and L. J. Pyrak-Nolte. A novel deep reactive ion etched (DRIE) glass micro-model for two-phase flow experiments. *Lab on a Chip*, 12(18):3413–3418, 2012. doi: 10.1039/c2lc40530j.

D. H. Kim, N. Mahabadi, J. Jang, and L. A. van Paassen. Assessing the Kinetics and Pore-Scale Characteristics of Biological Calcium Carbonate Precipitation in Porous Media using a Microfluidic Chip Experiment. *Water Resources Research*, 56:e2019WR025420, 2020. doi: 10.1029/2019WR025420.

C. M. Kirkland, A. Akyel, R. Hiebert, J. McCloskey, J. Kirksey, A. B. Cunningham, R. Gerlach, L. Spangler, and A. J. Phillips. Ureolysis-induced calcium carbonate precipitation (UICP) in the presence of CO_2-affected brine: A field demonstration. *International Journal of Greenhouse Gas Control*, 109:103391, 2021. doi: 10.1016/j.ijggc.2021.103391.

T. Koch, D. Gläser, K. Weishaupt, S. Ackermann, M. Beck, B. Becker, S. Burbulla, H. Class, E. Coltman, S. Emmert, T. Fetzer, C. Grüninger, K. Heck, J. Hommel, T. Kurz, M. Lipp, F. Mohammadi, S. Scherrer, M. Schneider, G. Seitz, L. Stadler, M. Utz, F. Weinhardt, and B. Flemisch. DuMux 3 - an open-source simulator for solving flow and transport problems in porous media with a focus on model coupling. *Computers and Mathematics with Applications*, 81:423–443, 2021. doi: 10.1016/j.camwa.2020.02.012.

J. A. Kozeny. Über kapillare Leitung des Wassers im Boden. *Royal Academy of Science, Vienna, Proc. Class I*, 136:271–306, 1927.

B. Krajewska. Ureases I. Functional, catalytic and kinetic properties: A review. *Journal of Molecular Catalysis B: Enzymatic*, 59:9–21, 2009. doi: 10.1016/j.molcatb.2009.01.003.

S. E. Lambert and D. G. Randall. Manufacturing bio-bricks using microbial induced calcium carbonate precipitation and human urine. *Water Research*, 160:158–166, 2019. doi: 10.1016/j.watres.2019.05.069.

D. Landa-Marbán, S. Tveit, K. Kumar, and S. E. Gasda. Practical approaches to study microbially induced calcite precipitation at the field scale. *International Journal of Greenhouse Gas Control*, 106:103256, 2021. doi: 10.1016/j.ijggc.2021.103256.

E. G. Lauchnor, D. M. Topp, A. E. Parker, and R. Gerlach. Whole cell kinetics of ureolysis by Sporosarcina pasteurii. *Journal of Applied Microbiology*, 118(6):1321–1332, 2015. doi: 10.1111/jam.12804.

Y. S. Lee and W. Park. Current challenges and future directions for bacterial self-healing concrete. *Applied Microbiology and Biotechnology*, 102(7):3059–3070, 2018. doi: 10.1007/s00253-018-8830-y.

Y. Li, K. Wen, L. Li, W. Huang, C. Bu, and F. Amini. Experimental investigation on compression resistance of bio-bricks. *Construction and Building Materials*, 265:120751, 2020. doi: 10.1016/j.conbuildmat.2020.120751.

L. J. McDonald, W. Afzal, and F. P. Glasser. Evidence of scawtite and tilleyite formation at ambient conditions in hydrated Portland cement blended with freshly-precipitated nano-size calcium carbonate to reduce greenhouse gas emissions. *Journal of Building Engineering*, 48:103906, 2022. doi: 10.1016/j.jobe.2021.103906.

A. Meier. *Mineralization and dissolution of calcium carbonate by microbial activities*. PhD thesis, Friedrich-Schiller-Universität Jena, 2017.

J. M. Minto, R. J. Lunn, and G. El Mountassir. Development of a Reactive Transport Model for Field-Scale Simulation of Microbially Induced Carbonate Precipitation. *Water Resources Research*, 55(8):7229–7245, 2019. doi: 10.1029/2019WR025153.

A. C. Mitchell, E. J. Espinosa-Ortiz, S. L. Parks, A. J. Phillips, A. B. Cunningham, and R. Gerlach. Kinetics of calcite precipitation by ureolytic bacteria under aerobic and anaerobic conditions. *Biogeosciences*, 16(10):2147–2161, 2019. doi: 10.5194/bg-16-2147-2019.

D. Möller. *Chemistry for environmental scientists*. de Gruyter, Berlin, 2015. ISBN 9783110409994.

J. W. Mullin. *Crystallization*. Butterworth-Heinemann, Oxford, 3rd edition, 1993. ISBN 0750611294.

M. K. Nassar, D. Gurung, M. Bastani, T. R. Ginn, B. Shafei, M. G. Gomez, C. M. Graddy, D. C. Nelson, and J. T. DeJong. Large-Scale Experiments in Microbially Induced Calcite Precipitation (MICP): Reactive Transport Model Development and Prediction. *Water Resources Research*, 54(1):480–500, 2018. doi: 10.1002/2017WR021488.

H. Nebel. *Kontrollierte Fällung von CaCO3 in einem modular aufgebauten Kristallisationsreaktor*. PhD thesis, University of Duisburg-Essen, Essen, 2008.

C. Nething, M. Smirnova, J. A. Gröning, W. Haase, A. Stolz, and W. Sobek. A method for 3D printing bio-cemented spatial structures using sand and urease active calcium carbonate powder. *Materials and Design*, 195:109032, 2020. doi: 10.1016/j.matdes.2020.109032.

V. L. Pacheco, L. Bragagnolo, C. Reginatto, and A. Thomé. Microbially Induced Calcite Precipitation (MICP): Review from an Engineering Perspective. *Geotechnical and Geological Engineering*, 2022. doi: 10.1007/s10706-021-02041-1.

A. J. Phillips, R. Gerlach, E. Lauchnor, A. C. Mitchell, A. B. Cunningham, and L. Spangler. Engineered applications of ureolytic biomineralization: A review. *Biofouling*, 29(6):715–733, 2013. doi: 10.1080/08927014.2013.796550.

A. J. Phillips, A. B. Cunningham, R. Gerlach, R. Hiebert, C. Hwang, B. P. Lomans, J. Westrich, C. Mantilla, J. Kirksey, R. Esposito, and L. Spangler. Fracture Sealing with Microbially-Induced Calcium Carbonate Precipitation: A Field Study. *Environmental Science and Technology*, 50(7):4111–4117, 2016. doi: 10.1021/acs.est.5b05559.

D. Proudfoot, L. Brooks, C. H. Gammons, E. Barth, D. Bless, R. M. Nagisetty, and E. G. Lauchnor. Investigating the potential for microbially induced carbonate precipitation to treat mine waste. *Journal of Hazardous Materials*, 424:127490, 2022. doi: https://doi.org/10.1016/j.jhazmat.2021.127490.

C.-Z. Qin, S. M. Hassanizadeh, and A. Ebigbo. Pore-scale network modeling of microbially induced calcium carbonate precipitation: Insight into scale dependence of biogeochemical reaction rates. *Water Resources Research*, 52(11):8794–8810, 2016. doi: 10.1002/2016WR019128.

M. Rahman, R. N. Hora, I. Ahenkorah, and S. Beecham. State-of-the-Art Review of Microbial-Induced Calcite Precipitation and Its Sustainability in Engineering Applications. *Sustainability*, 12(15):6281, 2020. doi: 10.3390/su12156281.

A. Rajasekar, S. Wilkinson, and C. K. Moy. MICP as a potential sustainable technique to treat or entrap contaminants in the natural environment: A review. *Environmental Science and Ecotechnology*, 6:100096, 2021. doi: 10.1016/j.ese.2021.100096.

J. D. Rodriguez-Blanco, S. Shaw, and L. G. Benning. The kinetics and mechanisms of amorphous calcium carbonate (ACC) crystallization to calcite, via vaterite. *Nanoscale*, 3 (1):265–271, 2011. doi: 10.1039/c0nr00589d.

M. Ruf and H. Steeb. An open, modular, and flexible micro X-ray computed tomography system for research. *Review of Scientific Instruments*, 91:113102, 2020. doi: 10.1063/5.0019541.

M. S. Sabo and L. E. Beckingham. Porosity-Permeability Evolution During Simultaneous Mineral Dissolution and Precipitation. *Water Resources Research*, 57:e2020WR029072, 2021. doi: 10.1029/2020WR029072.

D. Scheer, H. Class, and B. Flemisch. *Subsurface environmental modelling between science and policy*. Springer International Publishing, Cham, 2021. ISBN 978-3-030-51178-4. doi: 10.1007/978-3-030-51178-4.

R. Ševčík, P. Šašek, and A. Viani. Physical and nanomechanical properties of the synthetic anhydrous crystalline CaCO3 polymorphs: vaterite, aragonite and calcite. *Journal of Materials Science*, 53(6):4022–4033, 2018. doi: 10.1007/s10853-017-1884-x.

W. Song, T. W. De Haas, H. Fadaei, and D. Sinton. Chip-off-the-old-rock: The study of reservoir-relevant geological processes with real-rock micromodels. *Lab on a Chip*, 14 (22):4382–4390, 2014. doi: 10.1039/c4lc00608a.

D. Terzis and L. Laloui. 3-D micro-architecture and mechanical response of soil cemented via microbial-induced calcite precipitation. *Scientific Reports*, 8:1416, 2018. doi: 10.1038/s41598-018-19895-w.

L. F. Thompson. *An introduction to lithography*. ACS Publications, Washington, 1983. ISBN 9780841210400. doi: 10.1021/bk-1983-0219.

M. Umar, K. A. Kassim, and K. T. Ping Chiet. Biological process of soil improvement in civil engineering: A review. *Journal of Rock Mechanics and Geotechnical Engineering*, 8 (5):767–774, 2016. doi: 10.1016/j.jrmge.2016.02.004.

S. Vahid Dastjerdi, H. Steeb, M. Ruf, D. Lee, F. Weinhardt, N. Karadimitriou, and H. Class. *micro-XRCT dataset of Enzymatically Induced Calcite Precipitation (EICP) in a microfluidic cell*. DaRUS, V1, 2021. doi: 10.18419/darus-866.

L. A. van Paassen, R. Ghose, T. J. van der Linden, W. R. van der Star, and M. C. van Loosdrecht. Quantifying biomediated ground improvement by ureolysis: Large-scale biogrout experiment. *Journal of Geotechnical and Geoenvironmental Engineering*, 136(12):1721–1728, 2010. doi: 10.1061/(ASCE)GT.1943-5606.0000382.

W. K. van Wijngaarden, F. J. Vermolen, G. A. van Meurs, and C. Vuik. Modelling Biogrout: A New Ground Improvement Method Based on Microbial-Induced Carbonate Precipitation. *Transport in Porous Media*, 87(2):397–420, 2011. doi: 10.1007/s11242-010-9691-8.

A. Verma and K. Pruess. Thermohydrological conditions and silica redistribution near high-level nuclear wastes emplaced in saturated geological formations. *Journal of Geophysical Research*, 93(B2):1159–1173, 1988. doi: 10.1029/JB093iB02p01159.

L. von Wolff, F. Weinhardt, H. Class, J. Hommel, and C. Rohde. Investigation of Crystal Growth in Enzymatically Induced Calcite Precipitation by Micro-Fluidic Experimental Methods and Comparison with Mathematical Modeling. *Transport in Porous Media*, 137 (2):327–343, 2021. doi: 10.1007/s11242-021-01560-y.

A. Wagner, E. Eggenweiler, F. Weinhardt, Z. Trivedi, D. Krach, C. Lohrmann, K. Jain, N. Karadimitriou, C. Bringedal, P. Voland, C. Holm, H. Class, H. Steeb, and I. Rybak. Permeability Estimation of Regular Porous Structures: A Benchmark for Comparison of Methods. *Transport in Porous Media*, 138:1–23, 2021. doi: 10.1007/s11242-021-01586-2.

W. Wang, S. Chang, and A. Gizzatov. Toward Reservoir-on-a-Chip: Fabricating Reservoir Micromodels by in Situ Growing Calcium Carbonate Nanocrystals in Microfluidic Channels. *ACS Applied Materials and Interfaces*, 9(34):29380–29386, 2017. doi: 10.1021/acsami.7b10746.

Y. Wang, K. Soga, J. T. Dejong, and A. J. Kabla. A microfluidic chip and its use in characterising the particle-scale behaviour of microbial-induced calcium carbonate precipitation (MICP). *Geotechnique*, 69(12):1086–1094, 2019a. doi: 10.1680/jgeot.18.P.031.

Y. Wang, K. Soga, J. T. DeJong, and A. J. Kabla. Microscale Visualization of Microbial-Induced Calcium Carbonate Precipitation Processes. *Journal of Geotechnical and Geoen-*

vironmental Engineering, 145(9):04019045, 2019b. doi: 10.1061/(asce)gt.1943-5606.0002079.

Y. Wang, K. Soga, J. T. DeJong, and A. J. Kabla. Effects of Bacterial Density on Growth Rate and Characteristics of Microbial-Induced CaCO3 Precipitates: Particle-Scale Experimental Study. *Journal of Geotechnical and Geoenvironmental Engineering*, 147(6):04021036, 2021. doi: 10.1061/(asce)gt.1943-5606.0002509.

Y. Wang, C. Konstantinou, K. Soga, G. Biscontin, and A. J. Kabla. Use of microfluidic experiments to optimize MICP treatment protocols for effective strength enhancement of MICP-treated sandy soils. *Acta Geotechnica*, 9:1–22, 2022. doi: 10.1007/s11440-022-01478-9.

F. Weinhardt, H. Class, S. Vahid Dastjerdi, N. Karadimitriou, D. Lee, and H. Steeb. Experimental Methods and Imaging for Enzymatically Induced Calcite Precipitation in a Microfluidic Cell. *Water Resources Research*, 57:e2020WR029361, 2021a. doi: 10.1029/2020WR029361.

F. Weinhardt, H. Class, S. Vahid Dastjerdi, N. Karadimitriou, D. Lee, and H. Steeb. *Optical Microscopy and pressure measurements of Enzymatically Induced Calcite Precipitation (EICP) in a microfluidic cell*. DaRUS, V1, 2021b. doi: 10.18419/darus-818.

F. Weinhardt, J. Deng, J. Hommel, S. Vahid Dastjerdi, H. Steeb, and H. Class. Spatiotemporal Distribution of Precipitates and Mineral Phase Transition During Biomineralization Affect Porosity-Permeability Relationships. *Transport in Porous Media*, 2022a. doi: 10.1007/s11242-022-01782-8.

F. Weinhardt, J. Deng, H. Steeb, and H. Class. *Optical Microscopy and log data of Enzymatically Induced Calcite Precipitation (EICP) in microfluidic cells (Quasi-2D-structure)*. DaRUS, V1, 2022b. doi: 10.18419/darus-1799.

K. Weishaupt. *Model Concepts for Coupling Free Flow with Porous Medium Flow at the Pore-Network Scale: From Single-Phase Flow to Compositional Non-Isothermal Two-Phase Flow*. PhD thesis, University of Stuttgart, Stuttgart, 2020.

V. S. Whiffin, L. A. van Paassen, and M. P. Harkes. Microbial carbonate precipitation as a soil improvement technique. *Geomicrobiology Journal*, 24(5):417–423, 2007. doi: 10.1080/01490450701436505.

Y. Wu, H. Li, and Y. Li. Biomineralization induced by cells of sporosarcina pasteurii: Mechanisms, applications and challenges. *Microorganisms*, 9:2396, 2021. doi: 10.3390/microorganisms9112396.

Y. Xia and G. M. Whitesides. Soft Lithography. *Angewandte Chemie International Edition*, 37(5):550–575, 1998. doi: 10.1002/(sici)1521-3773(19980316)37:5⟨550::aid-anie550⟩3.0.co;2-g.

Y. Xiao, X. He, W. Wu, A. W. Stuedlein, T. M. Evans, J. Chu, H. Liu, L. A. van Paassen, and H. Wu. Kinetic biomineralization through microfluidic chip tests. *Acta Geotechnica*, 16 (10):3229–3237, 2021. doi: 10.1007/s11440-021-01205-w.

Y. Xiao, X. He, A. W. Stuedlein, J. Chu, T. Matthew Evans, and L. A. van Paassen. Crystal Growth of MICP through Microfluidic Chip Tests. *Journal of Geotechnical and Geoenvironmental Engineering*, 148(5):06022002, 2022. doi: 10.1061/(asce)gt.1943-5606.0002756.

H. Yasuhara, D. Neupane, K. Hayashi, and M. Okamura. Experiments and predictions of physical properties of sand cemented by enzymatically-induced carbonate precipitation. *Soils and Foundations*, 52(3):539–549, 2012. doi: 10.1016/j.sandf.2012.05.011.

N. M. Zambare, N. Y. Naser, R. Gerlach, and C. B. Chang. Mineralogy of microbially induced calcium carbonate precipitates formed using single cell drop-based microfluidics. *Scientific Reports*, 10:17535, 2020. doi: 10.1038/s41598-020-73870-y.

T. Zhang and I. Klapper. Critical occlusion via biofilm induced calcite precipitation in porous media. *New Journal of Physics*, 16:055009, 2014. doi: 10.1088/1367-2630/16/5/055009.

A Publications

A.1 Contribution 1: Experimental Methods and Imaging for Enzymatically Induced Calcite Precipitation in a microfluidic cell

Title	Experimental Methods and Imaging for Enzymatically Induced Calcite Precipitation in a Microfluidic Cell
Authors	**Felix Weinhardt** , Holger Class , Samaneh Vahid Dastjerdi, Nikolaos Karadimitriou , Dongwon Lee , and Holger Steeb
Journal	Water Resources Research
Publication status	published: February, 03, 2021 (accepted manuscript online); March, 11, 2021 (issue online)
copyright	open access (creative common)
DOI	https://doi.org/10.1029/2020WR029361
Dataset(s)	https://doi.org/10.18419/darus-818 https://doi.org/10.18419/darus-866

Table A.1: Metadata of contribution I

AGU ADVANCING EARTH AND SPACE SCIENCE

Water Resources Research

TECHNICAL REPORTS: METHODS

10.1029/2020WR029361

Experimental Methods and Imaging for Enzymatically Induced Calcite Precipitation in a Microfluidic Cell

Felix Weinhardt[1], Holger Class[1], Samaneh Vahid Dastjerdi[2], Nikolaos Karadimitriou[2], Dongwon Lee[2], and Holger Steeb[2,3]

[1]Department of Hydromechanics and Modelling of Hydrosystems, University of Stuttgart, Stuttgart, Germany, [2]Institute of Applied Mechanics, University of Stuttgart, Stuttgart, Germany, [3]SC SimTech, University of Stuttgart, Stuttgart, Germany

Key Points:

- An experimental set-up for reliable pressure measurement in microfluidic cells during continuous enzyme-induced calcite precipitation
- Synchronized time-resolved optical microscopy with pressure measurements allows for correlating the pore space alteration with permeability
- X-ray microcomputed tomography complements optical microscopy for estimating volume changes

Supporting Information:

- Supporting Information S1

Correspondence to:

F. Weinhardt,
felix.weinhardt@iws.uni-stuttgart.de

Citation:

Weinhardt, F., Class, H., Vahid Dastjerdi, S., Karadimitriou, N., Lee, D., & Steeb, H. (2021). Experimental methods and imaging for enzymatically induced calcite precipitation in a microfluidic cell. *Water Resources Research*, *57*, e2020WR029361. https://doi.org/10.1029/2020WR029361

Received 21 DEC 2020
Accepted 29 JAN 2021

Abstract Enzymatically induced calcite precipitation (EICP) in porous media can be used as an engineering option to achieve precipitation in the pore space, for example, aiming at a targeted sealing of existing flow paths. This is accomplished through a porosity and consequent permeability alteration. A major source of uncertainty in modeling EICP is in the quantitative description of permeability alteration due to precipitation. This report presents methods for investigating experimentally the time-resolved effects of growing precipitates on porosity and permeability on the pore scale, in a poly-di-methyl-siloxane microfluidic flow cell. These methods include the design and production of the microfluidic cells, the preparation and usage of the chemical solutions, the injection strategy, and the monitoring of pressure drops for given fluxes for the determination of permeability. EICP imaging methods are explained, including optical microscopy and X-ray microcomputed tomography (XRCT), and the corresponding image processing and analysis. We present and discuss a new experimental procedure using a microfluidic cell, as well as the general perspectives for further experimental and numerical simulation studies on induced calcite precipitation. The results of this study show the enormous benefits and insights achieved by combining both light microscopy and XRCT with hydraulic measurements in microfluidic chips. This allows for a quantitative analysis of the evolution of precipitates with respect to their size and shape, while monitoring their influence on permeability. We consider this to be an improvement of the existing methods in the literature regarding the interpretation of recorded data (pressure, flux, and visualization) during pore morphology alteration.

1. Introduction

Induced calcite precipitation is an engineering option which can be employed for a targeted sealing of flow paths in the subsurface as it might be necessary in geological gas storage in the presence of conductive faults (Ebigbo et al., 2010; Hommel et al., 2013; Phillips, Gerlach, et al., 2013; Phillips, Lauchnor, et al., 2013), for creating barriers for groundwater and containment of subsurface contamination (Cuthbert et al., 2013), and for soil stabilization and improvement of the mechanical soil properties (Hamdan & Kavazanjian, 2016; van Paassen et al., 2010; Wiffin et al., 2007). There are different techniques to achieve targeted calcite precipitation at a desired location. One of them is referred to as enzymatically induced calcite precipitation (EICP). Basically, EICP as we employ it here, relies on the dissociation of urea into carbon dioxide and ammonium catalyzed by the enzyme urease, which is extracted from jack-bean meal (JBM). In circumneutral environments regarding the pH value, ammonium (NH_4^+) and bicarbonate are the dominant products of hydrolysis, see Equation 1 (Mitchell et al., 2019). However, carbon dioxide in aqueous solutions occurs as carbonic acid (H_2CO_3), bicarbonate (HCO_3^-), or carbonate (CO_3^{2-}), depending on the pH value. Since ammonia acts as a weak base by taking up a proton and producing hydroxide, it increases the pH value and shifts the equilibrium toward carbonate ions. The additional presence of calcium ions, in our case provided by adding calcium chloride, forces calcium carbonate to precipitate. According to van Paassen (2009), the release of a proton (H^+) during the calcium carbonate precipitation buffers the production of hydroxide during the hydrolysis, see Equation 2. On the pore scale, precipitated calcium carbonate leads to changes in pore morphology, and on a larger scale, after averaging, this corresponds to changes in the effective quantities porosity and permeability,

$$CO(NH_2)_2 + 3H_2O \xrightarrow{\text{urease}} 2NH_4^+ + HCO_3^- + OH^-, \quad (1)$$

$$HCO_3^- + Ca^{2+} \rightarrow CaCO_3 \downarrow + H^+. \quad (2)$$

In contrast to EICP, the technology of microbially induced calcite precipitation (MICP) relies on microbes expressing the enzyme urease. While the basic mechanism of precipitating carbonates altering the pore morphology is similar as in EICP, the MICP technology is more complex in application; and in particular, the impacts on porous-media properties are even more challenging to model. MICP involves the growth of bacteria and biofilms that have also an influence on the evolving pore space, however not the same as the precipitated calcite. Biofilm is a soft matter and to some extent flexible to adapt to variable shear stress at variable flow velocity. In contrast, precipitated carbonates tend to be more rigid solids.

Recent models developed for MICP have focused on the reaction part and its kinetics (Bachmeier et al., 2012; Ebigbo et al., 2010; Hommel et al., 2015), while it is acknowledged that kinetics are often strongly coupled to hydraulic processes (Ebigbo et al., 2012; Hommel et al., 2016). It has been shown that MICP models can be successfully applied to field-scale application (Cunningham et al., 2019; Minto et al., 2019), although it is highly challenging to validate such models with appropriate and relevant experiments.

In this study, we aim at elaborating on the much-needed experimental evidence for a deeper understanding of the processes at the pore scale that alter pore morphology and eventually change effective parameters porosity and permeability. We envision to determine more thorough process-related knowledge on porosity–permeability relations regarding EICP and MICP. We acknowledge that the Darcy scale (or REV scale), see for example, the respective definitions in Hommel et al. (2018), is the appropriate scale to model field-scale applications of MICP or EICP, where computational demands can become a limiting factor. However, it is the pore scale where the morphological changes occur and from where we, consequently, need to derive new insights. Therefore, we use microfluidics for analyzing EICP processes in the details of our interest.

Precipitation processes in microfluidic devices have been studied in the past with various objectives. In the work of Zhang et al. (2010), mixing-induced carbonate precipitation was investigated in a microfluidic cell made out of Pyrex glass and silicon with the dimensions of 2 cm × 1 cm. The process was observed by optical microscopy with a resolution of 1.62 and 0.65 μm/pixel. Yoon et al. (2012) performed pore-scale simulations based on these experiments. Wang et al. (2019) studied MICP in a microfluidic chip made out of poly-di-methyl-siloxane (PDMS) with the dimension of 1.5 cm × 1.5 cm, fabricated very similar compared to the one that is used here. With a very high resolution of 0.65 μm/pixel, they were able to observe bacteria, as well as to capture qualitatively the shape of single crystals. In contrast, the experiments of Kim et al. (2020) were performed on a larger scale, observing the whole microfluidic chip over time with a resolution of 6.5 μm/pixel, during sequential injections of reactive solutions for EICP. The microfluidic chip was made out of glass and had the dimensions of 2.1 × 1.3 cm. Based on image processing, statistical analysis of the precipitates, more precisely the size distribution over time, was conducted and compared to a simplified kinetic model.

As already mentioned above, it is very important to get reliable quantitative information on the change of pore volume, that is, porosity on the Darcy scale, and on the alteration of pore morphology. Optical microscopy and image processing can provide mainly 2D information with limited details in the through-plane direction. As a complement to optical microscopy, we used X-ray microcomputed tomography (XRCT) to acquire information also in the through-plane direction, with our primary focus being on the change in the hydraulic parameters, like permeability, due to the growth of precipitates. Therefore, it is necessary to be able to monitor the induced pressure drop across the flow network reliably, under various boundary-flow conditions. The experiments presented here combine the visual observation of crystal nucleation and growth over time with reliable pressure measurements under continuous flow conditions. We use XRCT analysis of the shape of the crystals in order to be able to correlate 2D images with 3D structures of the precipitated carbonates in an effective way. This new experimental approach that we present here will allow for more comprehensive studies on EICP, and perspectively also on MICP, and its particularly complex porosity–permeability relations.

Furthermore, the results presented here can serve as a database for a comparison study of reactive transport simulations on the pore scale, including calcite precipitation.

Below, we introduce the materials and methods that are used, developed, and applied. This includes the production of the microfluidic cells by soft lithography, the experimental procedures for the EICP studies, as well as the imaging techniques. Subsequently, we present exemplary results on permeability determination from experiments and evaluate the imaging techniques. The discussion of the results puts a focus on the development of methods and on a workflow that is adapted to the EICP application. Still, we are able to draw important conclusions for further studies toward a better understanding of porosity–permeability relations in porous media affected by EICP or MICP.

2. Materials and Methods

The set-up and the workflow of the microfluidic experiment, including the preparation of the chemical solutions, are described in detail below. Subsequently, the two imaging methods, optical microscopy and XRCT scanning, are described and the corresponding postprocessing of the images is explained.

2.1. Microfluidic Experiments

In the scope of this work, three experiments were conducted, in the following referred to as Experiments 1–3. For each experiment, one microfluidic cell was produced, based on the same design. Essentially, they are three repetitions of identical experimental conditions, except for Experiment 2, which was cut short since clogging occurred during the precipitation. The set-up, experimental procedure, and image processing are explained in the following.

The microfluidic cells were produced by following the regular workflow of soft lithography (Karadimitriou et al., 2013; Xia & Whitesides, 1998). The designs of the pore-network geometry were generated with AutoCAD© and subsequently printed on an A4 transparency, with the pore space being transparent and the solid space being opaque. Such a transparency is commonly called a mask. These masks are employed in optical lithography with the use of SU8-2100 photoresist to produce photoresist spin-coated silicon wafers. After having followed the regular steps of photolithography, the photoresist features sticking out of the wafer had a height of 85 μm. These wafers were used in the production process of the actual microfluidic cells out of PDMS. A mixture of Dow Corning SYLGARD© 184 Silicone Elastomer base and the curing agent, at a mixing ratio of 10:1, is poured into a petri dish with a wafer, so as to create the PDMS slab with the features of the flow network. An equal quantity of the mixture is also poured into another petri dish without a wafer, to create a blank slab which is used as the sealing one. After degassing and subsequent curing for 2 h at 68°C, the resulting PDMS slabs are carefully removed from the wafer and the petri dish. Holes (ø1.5 mm) for the inlet and outlet tubes are punched and the PDMS slabs are diced to fit the size of a standard glass slide for microscopy (26 mm × 76 mm). The bonding of the two PDMS slabs together and subsequently on a glass slide is done with the corona treatment described in Haubert et al. (2006). After another 24 h, the bonding is complete and the microfluidic cells are ready to be used in the experiments.

The reactive solutions were prepared as follows: Solution 1 contained 1 g urea with a molar mass of 60.06 $\frac{\mathrm{g}}{\mathrm{mol}}$ and 2.45 g calcium chloride dihydrate with a molar mass of 147 $\frac{\mathrm{g}}{\mathrm{mol}}$ mixed in 50 mL deionized water. The mass concentrations correspond to an equimolar concentration of 1/3 $\frac{\mathrm{mol}}{\mathrm{L}}$. Both chemicals were provided by MERCK©. For Solution 2, the enzyme urease is extracted from JBM provided by Sigma Aldrich©. JBM (0.25 g) together with 50 mL deionized water are stirred at a constant temperature of 8°C. After 17 h of stirring, the solution is vacuum filtered twice with a 0.45 μm cellulose membrane to remove any JBM particles remaining. The concentrations we used to prepare the reactive solutions are based on similar investigations on EICP, like in the work of Kim et al. (2020) and Feder et al. (2020). From preliminary batch experiments, we know that right after mixing equal volumes of Solutions 1 and 2 the resulting pH value is around 7.

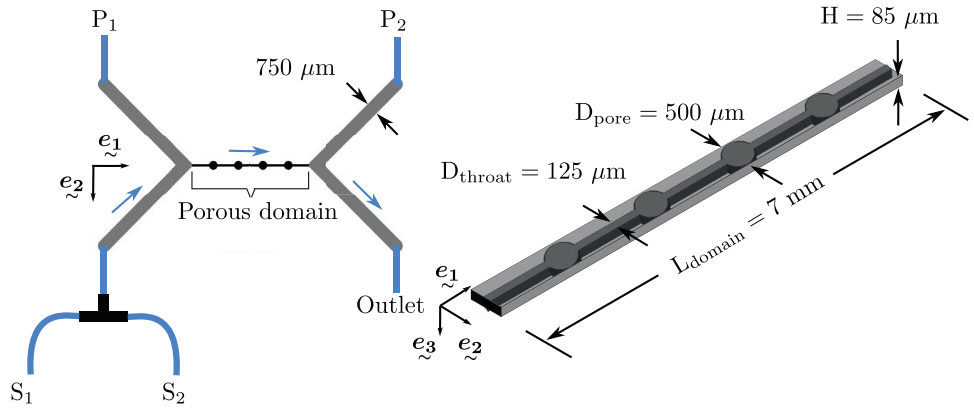

Figure 1. Left: sketch of the microfluidic set-up including the porous domain (black); the inlet, outlet, and pressure channels (gray); the tubes (blue) connected to the syringe pumps (S_1 and S_2) and to the pressure sensors (P_1 and P_2); the flux is indicated with blue arrows. Right: porous domain and its dimensions.

The design of the microfluidic cell and its geometrical parameters are shown in Figure 1. The pore throats have a size of 125 μm and the pore bodies a diameter of 500 μm. This is comparable to the geometric features of previous studies, like in Wang et al. (2019) or Kim et al. (2020) where the size of the pore throats range from below 50 to 140 μm. The inlet at the bottom left is connected with two 2.5 mL glass syringes (S_1, S_2) guided by two, one for each, midpressure pumps CETONI neMESYS 100 N which generate the flow. The interface between the syringe pumps and a computer for the control of the whole process is a base module, CETONI BASE 120. The software QMixElements is used to operate the experiment via predefined scripts. The tubes, connecting the microfluidic cell with the syringes and the pressure sensors, have an inner diameter of 0.5 mm and an outer diameter of 1.59 mm (1/16 in.) and are made of Teflon (poly-tetra-fluoro-ethylene). The outlet is connected to a reservoir with a constant water table of 10 cm above the microfluidic cell. This induces a back-pressure in order to reduce the risk of bubble formation during the experiment. Air bubbles can lead to difficulties in image postprocessing, as shown in the work of Kim et al. (2020), and are likely to disturb the pressure measurements. The tubes for the outlet have an inner diameter of 0.75 mm to avoid clogging. P_1 and P_2 indicate the location of the Elveflow MPS0 pressure sensors with a range of 70 mbar. The analog voltage signals of the pressure sensors are acquired and digitized with 16 bit using the CETONI I/O module at a rate of 1 Hz. By design, the inlet and outlet geometry was chosen to be bigger, so that they would not strongly affect the evolution of events inside the pore structure.

The pressure sensors are connected in parallel to the inlet and outlet channels, making sure that the pressure measurements are always taken under no flow (static) conditions. The inlet channels are large enough to be hydraulically connected to the pressure sensor during the whole precipitation process. Thus, it is possible to measure the pressure drop of the domain of interest (top right in Figure 1) without being compromised by precipitates in the inlet and outlet channels of the microfluidic cell. The porous domain in this work is defined as shown in Figure 1 on the right. Note that permeability in this work is defined arbitrarily (with assumptions for the dimensions used in Darcy's law), since the objective of this work is to measure relative effects, and the value for permeability is only used a normalization factor. The domain is a cuboid with dimensions $D_{\text{pore}} \times H \times L_{\text{domain}}$. Under the same concept, we only refer to porosity as "normalized porosity" due to the increased degrees of freedom in the selection of a reference domain.

Each experiment can be subdivided into three stages: (a) initial permeability measurement, (b) continuous injection of reactive solution, and (c) final permeability measurement, with the ambient temperature being 23°C.

In the beginning of the experiment, the permeability is estimated by applying different flow rates (0.01–1.5 $\frac{\mu L}{s}$) with deionized water only, and by measuring the pressure difference $\Delta p = p_2 - p_1$. Based on these measurements, the initial permeability of the porous domain can then be determined using Darcy's law

(Stage a). Afterward, the microfluidic cell is flushed with both reactant solutions at a high flow rate of 0.25 $\frac{\mu L}{s}$ for 5 min. Urea–calcium-chloride solution is introduced from S_1 and urease solution from S_2, in order to fully saturate the microfluidic cell with the reactive solution. Consequently, the continuous injection of reactive solution starts: a constant flow rate of 0.01 $\frac{\mu L}{s}$ for each syringe is applied for up to 5 h, resulting in a total flow of 0.02 $\frac{\mu L}{s}$ and a forced mixing of the reactants in the inlet tube right before entering the microfluidic cell (Stage b). During this stage, precipitation is taking place and the pressure is continuously monitored at the inlet and outlet of the microfluidic cell in order to quantify the hydraulic effects of the pore space alterations. The flow rate was chosen to ensure creeping flow conditions (Re < 1). The characteristic length, in the calculation of the Reynold's number, in this case is the height of cell H, since it is the smallest feature in the cell which makes it the dominant dimension. After precipitation, the system is flushed with deionized water at a constant flow rate of 0.02 $\frac{\mu L}{s}$ for 20 min. Finally, another permeability estimation is conducted by applying flow rates from 0.005 to 0.03 $\frac{\mu L}{s}$ with water only, while measuring the induced pressure difference $\Delta p = p_2 - p_1$ (Stage c).

2.2. Imaging

During the experiments, the processes were observed using optical microscopy, and after the experiment the microfluidic cells underwent an XRCT scan with all the precipitates in place. The set-up and the subsequent image processing of these methods are described in detail in the following.

2.2.1. Optical Microscopy

The transparent nature of PDMS allows for the direct, real-time visualization of the processes taking place in the pore space by using transmitted light microscopy. For this purpose, a custom-made microscope has been developed, which is able to visualize samples with a resolution of 0.5–20 μm per camera pixel. In the Supporting Information, a sketch with all components is given. An extended version of this optical set-up can be found in Karadimitriou et al. (2012).

In order to analyze the images obtained from optical microscopy with respect to the porosity change and the crystal growth, the gray-scale images were processed with the software Matlab R2019b© (The Mathworks, Inc.) using a procedure briefly described in the following and illustrated in Figure S3. As a first step, a mask was created that defines the porous domain based on the initial image without any precipitates. This includes filtering, geometrical and morphological operations, and binarization methods. When comparing images at different time steps while precipitation is still taking place, it is important that they are geometrically aligned. Even though the set-up, including the stage and the camera, is fixed, small changes of the position can occur. To overcome this issue, all subsequent images are registered to the initial image, before applying the above-mentioned methods to them. In the resulting binarized images, individual crystal aggregates can be identified and the size of their 2D projection can be derived.

2.2.2. X-Ray Microcomputed Tomography

After the EICP experiment, the microfluidic cells were further investigated by means of XRCT imaging. The scan was performed in an open and modular XRCT device. More details about the set-up can be found in the work of Ruf and Steeb (2020) or in the supporting information. The microfluidic cell domain was cut out from the total 3D-scanned volume. With the resolution of 4.25 $\frac{\mu m}{px}$, the size of the XRCT-imaged area (after alignment) is 2,100 × 519 × 20 voxels in length, width, and depth of the porous domain, respectively. This corresponds to a domain volume of approximately 89 × 22 × 0.085 mm.

XRCT scanning was carried out for all three experiments. However, due to the vast amount of a second phase observed around the precipitates after the experiments and before the scans, which will be explained in Section 3.3, only the XRCT data set of Experiment 3 was further postprocessed.

Image processing was performed again by using Matlab R2019b© (The Mathworks, Inc.). The raw images were imported to Matlab as a 3D data set. For facilitating the comparison with the 2D information, the images were transformed to achieve a 3D data set, in which the porous domain is aligned as it is in the microscopy images. Afterward, the images were filtered with a 3D median filter and segmented. Two methods, (i) of maximum entropy and (ii) Otsu (1979) thresholding, were applied to segment the images into four different phases, including the PDMS, the pore space, the calcium carbonate precipitates, and a liquid-resembling phase surrounding some of the crystals. The particles smaller than 10 voxels, which are mostly noise, were removed from the 3D precipitates. The remaining connected components, referred to as crystals, were then investigated. A more detailed description of the image processing can be found in supporting information.

3. Evaluation of the Methods

We evaluate and discuss here the methods described in the previous sections by means of the three experiments. At first, we describe the estimation of the permeability by evaluating the pressure measurements in comparison to the applied boundary-flow conditions. Subsequently, the potential of combining optical microscopy and XRCT scanning is pointed out.

3.1. Determination of Permeability

The permeability of the cell was determined (i) free from precipitates and (ii) with precipitates. It was estimated by applying various boundary-flow rates of deionized water while measuring the corresponding pressure drop (Stages a and c). By rearranging Darcy's law and using the slope of the negative pressure drop over the flow rate s_{pq}, the intrinsic permeability k can then be calculated as

$$k=\frac{\mu L_{domain}}{A s_{pq}}, \tag{3}$$

with A being the cross-sectional area ($H \times D_{\text{pore}}$) and L_{domain} the length of the domain as defined in Figure 1. For example, Figure 2 displays the measured negative pressure drop over the flow rate for Experiment 1. The applied flow rates in the case of the clean cells (before precipitation) show a wider range (up to 1.5 $\frac{\mu L}{s}$) in order to overcome the relatively larger error for small pressure drops. In the case of the cells with precipitates, the permeability is expected to be significantly reduced, thus inducing higher pressure drops for the same boundary-flow conditions. This allowed us to employ lower flow rates in our effort to avoid detachment of the precipitates due to increased shear stresses, while still being able to measure the corresponding pressures in a reliable way.

The boundary pressure is monitored continuously during the entire injection and precipitation period (Stage b). Under the reasonable assumption that the fluid viscosity remains constant throughout the duration of the experiment, the normalized permeability is the reciprocal of the normalized pressure drop ($k/k_0 = \Delta p_0/\Delta p$), while the subscript "0" corresponding to the initial state of the system, before any precipitation.

For both Experiments 1 and 3, the permeability reductions obtained from the subsequent permeability measurement (Stage c) were slightly higher compared to the last measurement during the continuous injection. We think the reason for this is the following. The solution with reactants in the inlet tube has to be flushed through the microfluidic cell before being able to continue with injecting water at different flow rates. This may result in further ongoing precipitation. Besides that, the injection of water could potentially mobilize small precipitates which are subsequently trapped at locations further downstream, as also reported in Mountassir et al. (2014). Since the microfluidic cell from Experiment 2 was apparently clogged, the subsequent permeability measurement could not be performed. However, since we determine the initial and final permeability by injection of water at different flow rates, we are confident that this allows for verifying the continuous pressure measurement during the precipitation phase. This experimental protocol demonstrates that the continuous pressure-monitoring strategy as explained here allows for reliable determination of permeability reductions of up to 3 orders of magnitude. Figure 2 shows the negative pressure drop of Experiments 1–3 during the precipitation process (Stage b) and, additionally, the permeability estimation of the initial and final states is given exemplarily for Experiment 1 (Stages a and c).

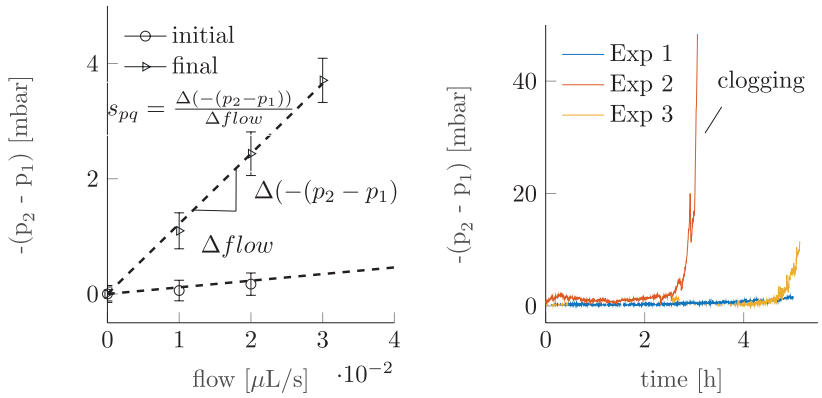

Figure 2. Left: negative pressure drop over flow rate for the cell at initial state and at the final state, after the precipitation—exemplary for Experiment 1; the slope s_{pq} is used to estimate the permeability based on Equation 3; right: negative pressure drop during the precipitation phase of Experiments 1–3.

3.2. Evolution Over Time as Derived From Optical Microscopy

The main advantage of using optical microscopy in this experimental procedure is the time-resolved visual observation of the precipitation process synchronized with continuous pressure measurements. This enables us to observe the nucleation and growth of the precipitates as well as their detachment and reattachment (if occurring) during the continuous injection of the reactant solutions. An exemplary detachment–reattachment process is shown in Figure S6.

After processing the images following the procedure in Section 2.2, the porosity change can be estimated, which is, in fact, essential for investigating porosity–permeability relations. Figure 3 shows the 2D porosity over time, normalized to its initial value. Experiments 1 and 2 show a similar trend of the reduction of the porosity over time, while in Experiment 3 the apparent decrease in pore volume is slower. Figure 3 shows that there are obviously less nuclei in the porous domain of Experiment 3. This lack of nucleation sites leads to a smaller decrease of the apparent 2D porosity over time. The nuclei seem to be spread randomly throughout the domain, but they could be influenced by small imperfections of the microfluidic cell itself. For example, small impurities of the elastomer base or curing agent, originating from the manufacturing process of the microfluidic cells, might cause these imperfections which can then result in a locally increased roughness of the surface. These imperfections can then act as initiation points and are, therefore, a preferred location for heterogeneous nucleation.

From 2D microscopy, we can easily observe crystal growth over time. However, the actual volume change including the third dimension can only be derived with further assumptions. In the work of Kim et al. (2020), the volume of individual crystals is estimated by assuming the shape of the crystals to be either cylindrical or semispherical. From the area observed by optical microscopy (A), an equivalent radius (r_{eq}) is calculated:

$$r_{eq} = \sqrt{\frac{A}{\pi}}. \tag{4}$$

The volume of individual crystals is then estimated based on the equivalent radius and the height of the microfluidic cell. However, in the work of Kim et al. (2020), the shapes are just hypothetical and have not been validated by three-dimensional imaging techniques. Following the same approach, other shapes like spherical or spheroidal shapes are potentially possible as well. In order to overcome these uncertainties, an additional XRCT scan has been performed in order to resolve the 3D structure of the precipitates.

3.3. 3D Structure of Precipitates Derived From XRCT Scan

In order to examine the shape of the crystal aggregates, the XRCT images are segmented and studied following the procedure as described in Section 2.2.2.

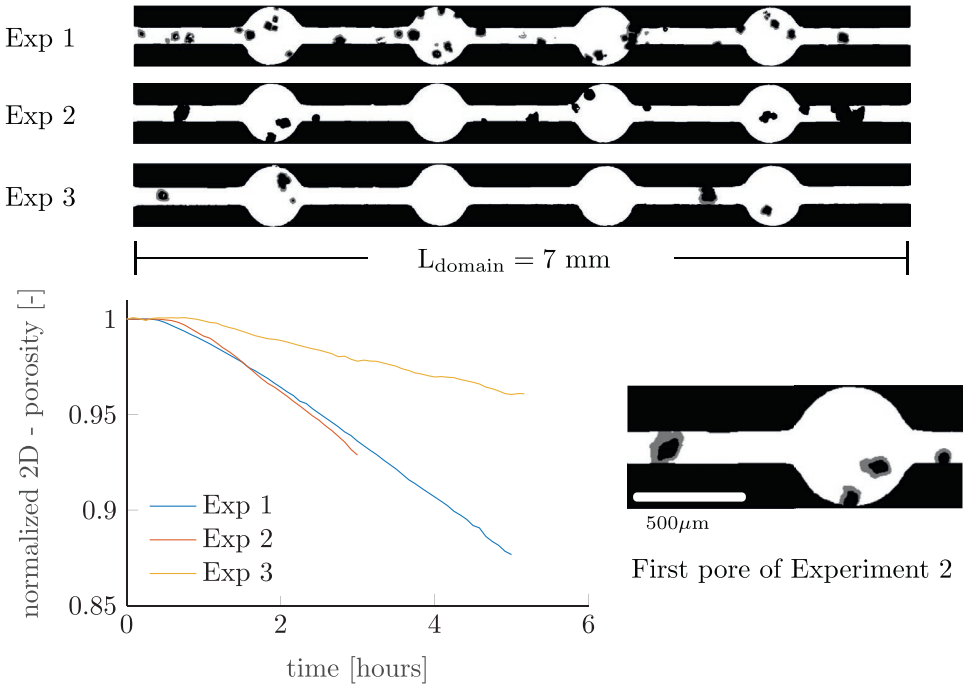

Figure 3. Top: processed images from optical microscopy of Experiments 1–3. Black indicates the crystals after 3 h and 10 min. Gray indicates the further development until the final states for Experiments 1 and 3; bottom left: normalized 2D porosity over time; right: crystal growth in the first pore of Experiment 2; gray indicates the growth within a period of 100 min.

One of the advantages of 3D imaging is the information it offers with respect to volume. Thus, the main purpose of performing an XRCT in this study is to support and complement the 2D information from optical microscopy imaging with the information on spatial extents in the third dimension. This is required for a reliable quantitative estimation of the porosity change in the 3D porous domain. For the figures from XRCT to be comparable to microscopy, the ideal case would be to preserve the final state of the crystals at the end of the experiments as accurately as possible.

After rinsing with deionized water and drying the cell when the experiment was concluded, it was observed that there was a second phase surrounding some of the precipitates. This phase had different X-ray attenuation properties, leading to distinctly different intensities of the gray values in the acquired images. In view of the fact that this second phase appears to be of unknown composition, we considered it not relevant for this work to further define its identity. Hence, in an attempt to be more compatible with the microscopy images, this second phase is removed from the XRCT data set. This is explained in more detail in the SI.

The investigation, with the focus being mainly on the shape-defining properties of the crystals, equipped us with the 3D structure of the crystal aggregates including their volume, surface, and distribution in the cell's depth. Figure 4 shows 2D projection of the microfluidic domain, including the shape of five crystal aggregates obtained from the XRCT scan, and demonstrates the opportunity that XRCT offers to determine the distribution of the aggregates in the depth of the cell. This information provides clues about the location of the nucleation point and to what extent they are attached to the walls of the flow cell as well. This is of great importance when studying EICP on the pore scale, since attachment and potential detachment of the aggregates strongly influence the process. Since we are able to resolve the 3D structure of the precipitates, we can use this to complement the optical imaging, for example, by evaluating different shape assumptions as mentioned in Section 3.2.

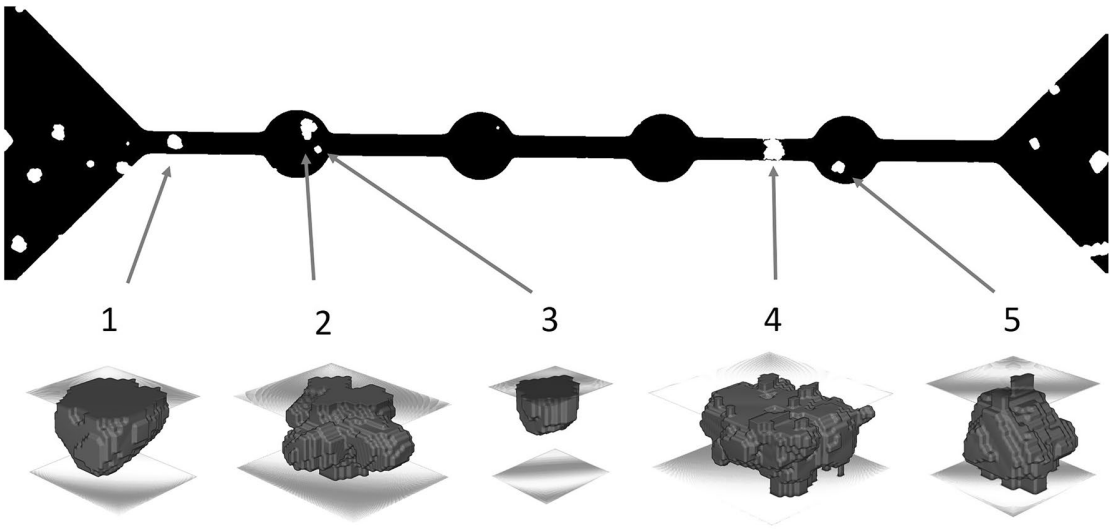

Figure 4. 2D projection of the microfluidic cell (top) and 3D structure of five crystal aggregates, obtained from the XRCT scan. XRCT, X-ray microcomputed tomography.

4. Discussion/Applicability for Further Investigations

As explained in Section 1, we consider this study being in the context of finding specific porosity–permeability relationships for EICP in porous media, and, perspectively, also for MICP where biofilms, additionally present in the pore space, render the problem even more complex. As a porous medium, we used flow cells made of PDMS, while we are aware of the possibility that the porous material and its surface may have an influence on the precipitation process, in particular on the generation of nucleation points due to locally increased roughness, surface charge, etc. This is definitely an aspect that we plan to consider in future studies.

What we have developed and presented above is an experimental strategy that we propose for assessing pore-scale alteration observed during EICP in microfluidic cells. We note here that the main achievement of this study is the experimental procedure rather than results for the envisioned porosity–permeability relations. The latter will be shown along with further experimental data and interpretations in a separate study. The requirements guiding us in designing the experimental procedure include a reliable determination of pore space alteration which can be resolved also in time. In other words, our demand is to assess the when, where, and what in the processes taking place regarding EICP with as much quantifiable data as possible. The cell design, the measurements, and the imaging techniques can be discussed in this context.

Regarding the design of the cell, we put an emphasis on a strongly simplified porous medium which allows for a detailed analysis of the shape of precipitated crystals. We note that this cell design due to its quasi-1D structure is probably not the best representative for deriving porosity-permeability relations in porous media. But the design is optimal for demonstrating and validating our workflow and, of course, it has to be changed and adapted to required complexities in future studies. Another important aspect for the cell design is the evaluation of pressure at the desired locations, that is, without being strongly influenced by precipitates in the inlet and outlet channels or tubes. With the designed pressure channels, we have found a satisfactory solution to this problem.

The continuous pressure measurements during injection and precipitation (Stage b) were necessary for the temporal resolution of the process. They were validated by permeability determination via injection of deionized water at varying rates, both before the injection (and precipitation) and after its stop. This implies a small temporal shift due to the required changes in the set-up, during which precipitation in the cell may go on and further change the pore space and the permeability. Yet, we could see that this effect is minor and the "validation" of the continuous pressure monitoring can be considered successful.

While the pressure information is important for concluding on permeability changes, imaging is the crucial part for the quantification of changes in pore morphology and pore volume. We have applied optical microscopy and, as a subsequent 3D characterization technique, XRCT scans. Similar to our approach with respect to the measurement of the pressure drop, we have here with the optical microscopy an approach of continuous monitoring during the injection and precipitation, while we use XRCT scans to prop up the 2D information from microscopy. Optical microscopy allows for observing changes of the pore structure synchronized with the continuous pressure measurements, but it does not resolve the structure of the precipitated solids in the third dimension.

We have mentioned that the microscopy images can be usefully complemented with the help of information from the XRCT scans. The XRCT scans, though costly and only a posteriori to perform unless maybe at a synchrotron tomography beamline, are able to resolve the third dimension. The shapes of the crystals can be examined and it enables finding reasonable approximations for volumes derived from 2D projections and, consequently, a better quantification of the changes in the pore space due to precipitation. This means that throughout our future experiments more value can be attributed to information from cheap and continuous optical microscopy. However, the XRCT scans require preparations; the cells need to be flushed, dried, and moved to the scanner. Thus, it is likely that there occur some discrepancies between the "final" state of the injection/precipitation experiment and scanned state. Time-resolved scanning during the experiment would require to apply for beam time in a synchrotron, which implies certain limitations. It is worth noting that the perfect experimental XRCT technique for a microfluidic cell, in which the aspect ratio of the depth relative to the other dimensions is small and is considered as flat, would be laminography (Gondrom et al., 1999). Nevertheless, we were able to derive beneficial information out of the XRCT set-up as it is already available to us.

The experimental procedure we propose in this study can be applied for more realistic designs of the porous domain, where flow has more degrees of freedom to bypass clogging, in order to derive realistic porosity–permeability relations. These relations are crucially important when modeling reactive transport during EICP or MICP including precipitation on the REV scale.

The provided data include the segmented XRCT scan, as well as the segmented images of microscopy. Based on these data, pore-scale simulations can be validated.

Data Availability Statement

The data sets will be available in the Data Repository of the University of Stuttgart (DaRUS). Two data sets are separately published: images of optical microscopy together with the log data, including flow rates and pressure measurements, can be found in Weinhardt et al. (2021). The XRCT data set is published in Vahid Dastjerdi et al. (2021).

Acknowledgments
The work was supported by the German Research Foundation (Deutsche Forschungsgemeinschaft, DFG) within the Collaborative Research Center 1313 (project number 327154368 – SFB 1313). We acknowledge funding by the DFG under Germany's Excellence Strategy EXC 2075 (project number 390740016 - EXC 2075).

References

Bachmeier, K., Williams, A., Warmington, J., & Bang, S. (2012). Urease activity in microbiologically-induced calcite precipitation. *Journal of Biotechnology*, *93*, 171–181. https://doi.org/10.1016/s0168-1656(01)00393-5

Cunningham, A., Class, H., Ebigbo, A., Gerlach, R., Phillips, A., & Hommel, J. (2019). Field-scale modeling of microbially induced calcite precipitation. *Computational Geosciences*, *23*, 399–414. https://doi.org/10.1007/s10596-018-9797-6

Cuthbert, M., McMillan, L., Handley-Sidhu, S., Riley, M., Tobler, D., & Phoenix, V. (2013). A field and modeling study of fractured rock permeability reduction using microbially induced calcite precipitation. *Environmental Science & Technology*, *47*(23), 13637–13643. https://doi.org/10.1021/es402601g

Ebigbo, A., Helmig, R., Cunningham, A., Class, H., & Gerlach, R. (2010). Modelling biofilm growth in the presence of carbon dioxide and water flow in the subsurface. *Advances in Water Resources*, *33*(7), 762–781. https://doi.org/10.1016/j.advwatres.2010.04.004

Ebigbo, A., Phillips, A., Gerlach, R., Helmig, R., Cunningham, A., Class, H., & Spangler, L. (2012). Darcy-scale modeling of microbially induced carbonate mineral precipitation in sand columns. *Water Resources Research*, *48*, W07519. https://doi.org/10.1029/2011WR011714

Feder, M. J., Akyel, A., Morasko, V. J., Gerlach, R., & Phillips, A. J. (2020). Temperature-dependent inactivation and catalysis rates of plant-based ureases for engineered biomineralization. *Engineering Reports*. *3*(2), e12299. https://doi.org/10.1002/eng2.12299

Gondrom, S., Zhou, J., Maisl, M., Reiter, H., Kröning, M., & Arnold, W. (1999). X-ray computed laminography: An approach of computed tomography for applications with limited access. *Nuclear Engineering and Design*, *190*, 141–147. https://doi.org/10.1016/S0029-5493(98)00319-7

Hamdan, N., & Kavazanjian, E. (2016). Enzyme-induced carbonate mineral precipitation for fugitive dust control. *Géotechnique*, *66*(7), 546–555. https://doi.org/10.1680/jgeot.15.P.168

Haubert, K., Drier, T., & Beebe, D. (2006). PDMS bonding by means of a portable, low-cost corona system. *Lab on a Chip*, *6*(12), 1548–1549. https://doi.org/10.1039/b610567j

Hommel, J., Coltman, E., & Class, H. (2018). Porosity–permeability relations for evolving pore space: A review with a focus on (bio-)geochemically altered porous media. *Transport in Porous Media*, *124*, 589–629. https://doi.org/10.1007/s11242-018-1086-2

Hommel, J., Cunningham, A., Helmig, R., Ebigbo, A., & Class, H. (2013). Numerical investigation of microbially induced calcite precipitation as a leakage mitigation technology. *Energy Procedia*, *40C*, 392–397. https://doi.org/10.1016/j.egypro.2013.08.045

Hommel, J., Lauchnor, E., Gerlach, R., Cunningham, A., Ebigbo, A., Helmig, R., & Class, H. (2016). Investigating the influence of the initial biomass distribution and injection strategies on biofilm-mediated calcite precipitation in porous media. *Transport in Porous Media*, *114*(2), 557–579. https://doi.org/10.1007/s11242-015-0617-3

Hommel, J., Lauchnor, E., Phillips, A., Gerlach, R., Cunningham, A. B., Helmig, R., et al. (2015). A revised model for microbially induced calcite precipitation: Improvements and new insights based on recent experiments. *Water Resources Research*, *51*, 3695–3715. https://doi.org/10.1002/2014WR016503

Karadimitriou, N. K., Joekar-Niasar, V., Hassanizadeh, S. M., Kleingeld, P. J., & Pyrak-Nolte, L. J. (2012). A novel deep reactive ion etched (DRIE) glass micro-model for two-phase flow experiments. *Lab on a Chip*, *12*, 3413–3418. https://doi.org/10.1039/C2LC40530J

Karadimitriou, N. K., Musterd, M., Kleingeld, P. J., Kreutzer, M. T., Hassanizadeh, S. M., & Joekar-Niasar, V. (2013). On the fabrication of PDMS micromodels by rapid prototyping, and their use in two-phase flow studies. *Water Resources Research*, *49*, 2056–2067. https://doi.org/10.1002/wrcr.20196

Kim, D. H., Mahabadi, N., Jang, J., & van Paassen, L. A. (2020). Assessing the kinetics and pore-scale characteristics of biological calcium carbonate precipitation in porous media using a microfluidic chip experiment. *Water Resources Research*, *56*, e2019WR025420. https://doi.org/10.1029/2019WR025420

Minto, J. M., Lunn, R. J., & El Mountassir, G. (2019). Development of a reactive transport model for field-scale simulation of microbially induced carbonate precipitation. *Water Resources Research*, *55*, 7229–7245. https://doi.org/10.1029/2019WR025153

Mitchell, A. C., Espinosa-Ortiz, E. J., Parks, S. L., Phillips, A. J., Cunningham, A. B., & Gerlach, R. (2019). Kinetics of calcite precipitation by ureolytic bacteria under aerobic and anaerobic conditions. *Biogeosciences*, *16*(10), 2147–2161. https://doi.org/10.5194/bg-16-2147-2019

Mountassir, G. E., Lunn, R. J., Moir, H., & MacLachlan, E. (2014). Hydrodynamic coupling in microbially mediated fracture mineralization: Formation of self-organized groundwater flow channels. *Water Resources Research*, *50*, 1–16. https://doi.org/10.1002/2013WR013578

Otsu, N. (1979). A threshold selection method from gray-level histograms. *IEEE Transactions on Systems, Man, and Cybernetics*, *9*(1), 62–66. https://doi.org/10.1109/TSMC.1979.4310076

Phillips, A., Gerlach, R., Lauchnor, E., Mitchell, A., Cunningham, A., & Spangler, L. (2013). Engineered applications of ureolytic biomineralization: A review. *Biofouling*, *29*(6), 715–733. https://doi.org/10.1080/08927014.2013.796550

Phillips, A., Lauchnor, E., Eldring, J., Esposito, R., Mitchell, A., Gerlach, R., et al. (2013). Potential CO_2 leakage reduction through biofilm-induced calcium carbonate precipitation. *Environmental Science & Technology*, *47*(1), 142–149. https://doi.org/10.1021/es301294q

Ruf, M., & Steeb, H. (2020). An open, modular, and flexible micro X-ray computed tomography system for research. *Review of Scientific Instruments*, *91*(11), 113102. https://doi.org/10.1063/5.0019541

Vahid Dastjerdi, S., Steeb, H., Ruf, M., Lee, D., Weinhardt, F., Karadimitriou, N., & Class, H. (2021). Micro-XRCT dataset of Enzymatically Induced Calcite Precipitation (EICP) in a microfluidic cell. *DaRUS*. https://doi.org/10.18419/darus-866

van Paassen, L. (2009). *Biogrout: Ground improvement by microbially induced carbonate precipitation* (PhD thesis). Delft, the Netherlands: Delft University of Technology.

van Paassen, L., Ghose, R., van der Linden, T., van der Star, W., & van Loosdrecht, M. (2010). Quantifying biomediated ground improvement by ureolysis: Large-scale biogrout experiment. *Journal of Geotechnical and Geoenvironmental Engineering*, *136*(12), 1721–1728. https://doi.org/10.1061/(ASCE)GT.1943-5606.0000382

Wang, Y., Soga, K., Dejong, J. T., & Kabla, A. J. (2019). A microfluidic chip and its use in characterising the particle-scale behaviour of microbial-induced calcium carbonate precipitation (MICP). *Géotechnique*, *69*(12), 1086–1094. https://doi.org/10.1680/jgeot.18.P.031

Weinhardt, F., Class, H., Vahid Dastjerdi, S., Karadimitriou, N., Lee, D., & Steeb, H. (2021). Optical microscopy and pressure measurements of Enzymatically Induced Calcite Precipitation (EICP) in a microfluidic cell. *DaRUS*. https://doi.org/10.18419/darus-818

Wiffin, V., van Paassen, L., & Harkes, M. (2007). Microbial carbonate precipitation as a soil improvement technique. *Geomicrobiology Journal*, *24*(5), 417–423. https://doi.org/10.1080/01490450701436505

Xia, Y., & Whitesides, G. M. (1998). Soft lithography. *Angewandte Chemie International Edition*, *37*(5), 550–575. https://doi.org/10.1146/annurev.matsci.28.1.153

Yoon, H., Valocchi, A. J., Werth, C. J., & Dewers, T. (2012). Pore-scale simulation of mixing-induced calcium carbonate precipitation and dissolution in a microfluidic pore network. *Water Resources Research*, *48*, W02524. https://doi.org/10.1029/2011WR011192

Zhang, C., Dehoff, K., Hess, N., Oostrom, M., Wietsma, T. W., Valocchi, A. J., et al. (2010). Pore-scale study of transverse mixing induced $CaCO_3$ precipitation and permeability reduction in a model subsurface sedimentary system. *Environmental Science & Technology*, *44*(20), 7833–7838. https://doi.org/10.1021/es1019788

A.2 Contribution 2: Investigation of Crystal Growth in Enzymatically Induced Calcite Precipitation by Micro-Fluidic Experimental Methods and Comparison with Mathematical Modeling

Title	Investigation of Crystal Growth in Enzymatically Induced Calcite Precipitation by Micro-Fluidic Experimental Methods and Comparison with Mathematical Modeling
Authors	Lars von Wolff, **Felix Weinhardt**, Holger Class, Johannes Hommel, Christian Rohde
Journal	Transport in Porous Media
Publication status	published (February, 24, 2021)
copyright	open access (creative common)
DOI	https://doi.org/10.1007/s11242-021-01560-y
Dataset(s)	-

Table A.2: Metadata of contribution II

Transport in Porous Media
https://doi.org/10.1007/s11242-021-01560-y

Investigation of Crystal Growth in Enzymatically Induced Calcite Precipitation by Micro-Fluidic Experimental Methods and Comparison with Mathematical Modeling

Lars von Wolff[1] · **Felix Weinhardt**[2] · **Holger Class**[2] · **Johannes Hommel**[2] · **Christian Rohde**[1]

Received: 14 October 2020 / Accepted: 28 January 2021

Abstract
Enzymatically induced calcite precipitation (EICP) is an engineering technology that allows for targeted reduction of porosity in a porous medium by precipitation of calcium carbonates. This might be employed for reducing permeability in order to seal flow paths or for soil stabilization. This study investigates the growth of calcium-carbonate crystals in a micro-fluidic EICP setup and relies on experimental results of precipitation observed over time and under flow-through conditions in a setup of four pore bodies connected by pore throats. A phase-field approach to model the growth of crystal aggregates is presented, and the corresponding simulation results are compared to the available experimental observations. We discuss the model's capability to reproduce the direction and volume of crystal growth. The mechanisms that dominate crystal growth are complex depending on the local flow field as well as on concentrations of solutes. We have good agreement between experimental data and model results. In particular, we observe that crystal aggregates prefer to grow in upstream flow direction and toward the center of the flow channels, where the volume growth rate is also higher due to better supply.

Keywords EICP · Micro-fluidics · Phase-field model · Reactive transport · Pore scale simulation

1 Introduction

Enzymatically induced calcium carbonate precipitation (EICP) is an engineering technology that employs enzymatic activity for altering geochemistry, thus resulting in precipitation of calcium carbonate. This is mostly due to hydrolysis of urea and catalyzed by ureases, which are widespread enzymes in soil bacteria and plants (Kappaun et al. 2018). In

✉ Lars von Wolff
lars.von-wolff@mathematik.uni-stuttgart.de

[1] Institute of Applied Analysis and Numerical Simulation, University of Stuttgart, Pfaffenwaldring 57, 70569 Stuttgart, Germany

[2] Department of Hydromechanics and Modelling of Hydrosystems, University of Stuttgart, Pfaffenwaldring 61, 70569 Stuttgart, Germany

this study, we focus on EICP via ureolysis by the enzyme urease extracted from ground seeds of the Jack Bean *Canavalia ensiformis*, which are known for their high urease content. Urease catalyzes the hydrolysis reaction of urea ($(NH_2)_2CO$), resulting at typical environmental conditions in the products bicarbonate (HCO_3^-) and ammonium (NH_4^+), i.e.,

$$(NH_2)_2CO + 3H_2O \xrightarrow{urease} NH_4^+ + H_2NCOO^- + 2H_2O \longrightarrow 2NH_4^+ + HCO_3^- + OH^-. \tag{1}$$

The products of ureolysis, HCO_3^- and NH_4^+, dissociate depending on pH. In the presence of calcium ions (Ca^{2+}), this results in calcium carbonate ($CaCO_3$) precipitation:

$$NH_3 + H^+ \rightleftharpoons NH_4^+, \tag{2}$$

$$H_2CO_3 \rightleftharpoons H^+ + HCO_3^- \rightleftharpoons 2H^+ + CO_3^{2-}, \tag{3}$$

$$Ca_2^+ + CO_3^{2-} \rightleftharpoons CaCO_3 \downarrow. \tag{4}$$

This yields the overall reaction

$$CO(NH_2)_2 + 2H_2O + Ca_2^+ \rightleftharpoons 2NH_4^+ + CaCO_3 \downarrow. \tag{5}$$

EICP offers an engineering option to precipitate calcium carbonate in situ, and by that to alter porous medium parameters such as porosity and permeability as well as the strength and stiffness of the porous medium. Hence, EICP can be used similarly to other methods of inducing mineral precipitation, such as, e.g., microbially induced calcium carbonate precipitation (MICP), to seal high-permeable leakage pathways. This has been demonstrated for MICP in various studies, (Cunningham et al. 2019; Phillips et al. 2016; Cuthbert et al. 2013; Phillips et al. 2013,[28]).

Applications for soil stabilization are described in (Whitaker et al. 2018; Mujah et al. 2017; van Paassen et al. 2010), for coprecipitation of heavy metals in (Lauchnor et al. 2013; Mitchell and Ferris 2005), or for building or monument restoration in (Minto et al. 2018). EICP itself has already been applied for dust control (Hamdan and Kavazanjian 2016),[41], soil strengthening (Neupane et al. 2013), or to modify permeability (Nemati and Voordouw 2003).

Successful sealing results from a complex interplay between the transport of chemicals and urease, determined by fluid dynamics, the ureolysis as well as the precipitation reaction leading to clogging and thus a change in the transport-determining porous medium properties. Numerical modeling can employ conceptual ideas for these individual processes and mechanisms, and account for complex interactions between different processes. As such it improves process-understanding, optimizes experimental and field setups, and predicts, e.g., the outcome of the application of EICP.

Field-scale applications require a Darcy-scale approach to be able to account for the large domain sizes. The Darcy-scale models of EICP or MICP, e.g., (Hommel et al. 2020; Minto et al. 2019; Cunningham et al. 2019; Nassar et al. 2018; van Wijngaarden et al. 2016; Hommel et al. 2018) currently rely on simple parametrizations of the effects of precipitation on porous-medium properties, such as permeability. Especially for the sealing applications of EICP or MICP, the correct prediction of permeability is of outstanding importance. To improve on the simplistic relations currently used to describe the change in porous-medium Darcy-scale properties due to EICP or MICP, the

pore-scale needs to be considered, as here Darcy-scale properties can be observed and described as changes in geometry.

This is experimentally possible due to advances in imaging technologies and their use, e.g., (Blunt et al. 2013; Wildenschild et al. 2013). From a modeling perspective, there are different approaches to the challenge of describing calcite precipitation at the pore scale. One can introduce a calcite volume fraction and determine by a threshold value whether to allow fluid flow (Yoon et al. 2012). A different idea is to determine the evolving surface of precipitated calcite. Of various suitable methods (Molins et al. 2020), the most straightforward is to describe the surface as a free boundary problem. In such sharp-interface models (van Duijn and Pop 2004), the interface between pore space and precipitated calcium carbonate evolves in time and gets characterized by its movement in normal direction. This approach requires a constant remeshing of the pore space available for flow, or more sophisticated methods of tracking the boundary, e.g., (Ray et al. 2019; Molins et al. 2012).

As an alternative, a diffuse-interface approach can be used. Phase-field models employ an additional order parameter to indicate the current phase. This order parameter is smoothed out between different phases, leading to a small diffuse transition zone. Such models have been previously used to account for both dissolution and precipitation, e.g., (van Noorden and Eck 2011; Redeker et al. 2016; Bringedal et al. 2020; Rohde and von Wolff 2020), as well as MICP without and with electrodiffusion, (Zhang and Klapper 2010) and (Zhang and Klapper 2011), respectively. Phase-field models are widely used to model interface dynamics, for the related issue of dendritic growth see (Takaki 2014) for a review.

In this study, we develop a phase-field model for EICP based on (Bringedal et al. 2020; Rohde and von Wolff 2020). For the reactions, we adopt simplifying assumptions of a constant ureolysis rate, calculated for the experimental conditions of (Weinhardt et al. 2020) based on the ureolysis kinetics of (Hommel et al. 2020). The precipitation process is assumed to be an equilibrium reaction, therefore crystal growth will be limited by the diffusion of ions to the crystal interface from the aqueous bulk liquid, which is oversaturated due to ureolysis.

Experimental and modeling investigations complement each other. The very small dimensions of the experimental setup do not allow for reliable measurements of local concentrations. Only minuscule volumes would be available for analysis and the volume of the inlet and outlet structures as well as the tubing are much larger than the volume of the region of interest.

Using complementary modeling, detailed concentration distributions, crystal growth rates and growth directions within the region of interest can be predicted reliably. The distribution of crystal aggregates and their growth over time is a measure available in both the experiment and the numerical simulation, allowing for a validation of the developed model by comparison of the model predictions with the experimental data. Note, that the developed model does not have any additional calibration parameters; the model estimates the calcite oversaturation due to enzymatic ureolysis in the inlet region using the jack beanmeal (JBM) extract ureolysis kinetics of (Hommel et al. 2020).

In this study, we show that the developed model reproduces the following observations of pore-scale experiments:

- Crystal aggregates grow faster on their upstream side than on their downstream side, leading to a shift of the center of mass in the upstream direction.
- Crystal aggregates grow faster in places of high flow velocity.

The study shows that our approach of diffusion-limited crystal growth reproduces the patterns observed in the experiments such as preferential growth toward the higher concentration gradient on the upstream side or in advection-dominated flow in pore throats. Perspectively, within a multi-scale approach, pore-scale models might inform Darcy-scale models what relation to use for predicting the change in Darcy-scale hydraulic properties and how to parameterize those relations.

2 Micro-Fluidic Experiments

2.1 Experimental Setup and Procedure

In this section, the micro-fluidic experiment is briefly described. More detailed information about the procedure and the setup can be found in the previous work of (Weinhardt et al. 2020). The micro-fluidic cells were produced by following the standard workflow of soft lithography (Karadimitriou et al. 2013; Xia and Whitesides 1998). The design of the micro-fluidic cell is shown in Fig. 1 and consists of an inlet channel, an outlet channel, and the actual domain of interest, which is a series of four identical circular pore bodies connected by rectangular pore throats. The details of the channels connected to the pressure sensors are not pictured here since the pressure measurements have been analyzed in detail in (Weinhardt et al. 2020) and are not in the focus of the present study here. There are two syringe pumps which induce the flow: Syringe 1 (S_1) is filled with an urea/calcium-chloride solution with equimolar concentrations of 1/3 mol/L. Syringe 2 (S_2) is filled with a solution extracted from a 5 g/L JBM suspension by filtering through a 0.45 μm cellulose membrane. The reactive solutions mix in the T-junction, before entering the micro-fluidic cell via an inlet tube of the length 10 cm and an inner diameter of 0.5 mm.

The whole system was initially saturated with deionized water. The inlet tube, the inlet channel, the porous domain and the outlet channel were subsequently saturated with the reactant solutions. The pressure sensors end up in a dead end. Therefore, there is no flow

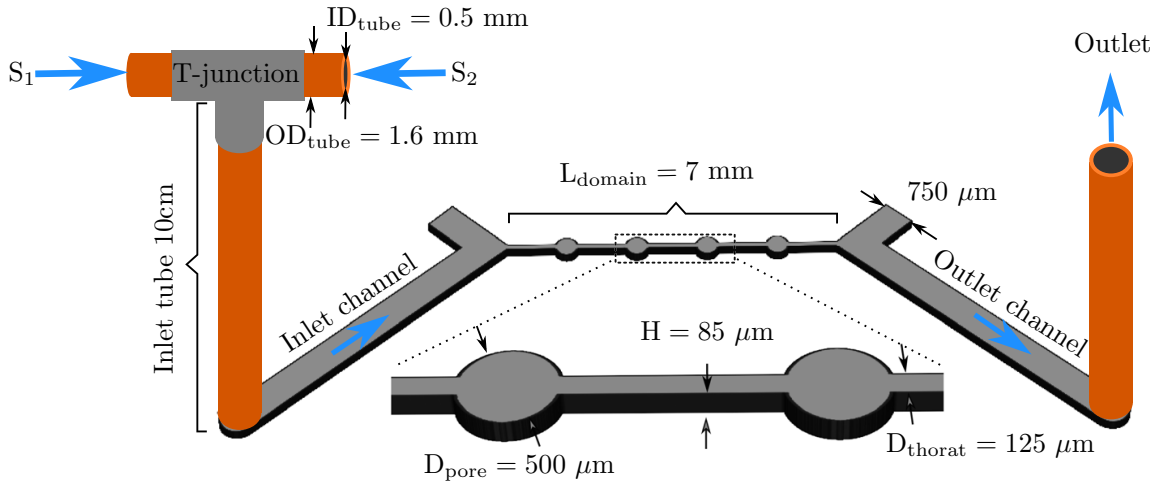

Fig. 1 Schematic sketch of the micro-fluidic cell and its dimensions: It includes the inlet and outlet tubes (orange) connected to the inlet and outlet channels. The domain of interest consists of four pore bodies connected with pore throats. A part of it is shown enlarged in the bottom of the figure. The blue arrows indicate the flow direction of the reactive solutions, induced by the syringe pumps S_1 and S_2, filled with urea calcium chloride solution and filtered JBM suspension respectively. Sketch based on (Weinhardt et al. 2020)

in the channels connected to the pressure sensors. Once the micro-fluidic cell was saturated with the reactive solutions, a constant flow rate of 0.01 μL/s was applied at both syringes for 5 h. The flow direction is indicated with blue arrows in Fig. 1. The transparent nature of polydimethylsiloxane (PDMS) allowed the direct visualization of the processes taking place in the pore space by using transmitted light microscopy. A description of the microscope used can be found in the work of (Karadimitriou et al. 2012). In Table 1, the concentrations of the reactive solutions, as well as the flow rates are summarized. The ambient temperature was 23°C throughout the experiment.

2.2 Kinetics of Urea Hydrolysis

The hydrolysis of urea can be assumed to follow a first-order kinetic reaction with respect to the concentration of urea c_{urea} (6) (Feder et al. 2020; Hommel et al. 2020). In this case, the reaction rate r_{u} is a function of the molar concentration of urea c_{urea} as well as the mass concentration of JBM extract, C_{JBM}.

$$r_{\text{u}} = -\frac{dc_{\text{urea}}}{dt} = k_{\text{u}} c_{\text{urea}} C_{\text{JBM}} \tag{6}$$

According to (Feder et al. 2020) and (Hommel et al. 2020), the temperature-dependent rate coefficient for enzymatic ureolysis, k_{u}, can be calculated using Arrhenius-type exponential relations. The expression (7) below is based on the experimental investigations of (Feder et al. 2020), with $a_{\text{u,0}}$ being the pre-exponential factor and $a_{\text{u,T}}$ being a lumped exponent describing the temperature dependence of the rate coefficient.

$$k_{\text{u}} = a_{\text{u,0}} e^{\left(\frac{a_{\text{u,T}}}{T}\right)} \tag{7}$$

By integrating Equation (6) over time, the concentration of urea can explicitly be calculated at a certain time t, based on an initial concentration of urea, $c_{\text{urea, 0}}$:

$$c_{\text{urea}}(t) = c_{\text{urea,0}} e^{-(k_u C_{JBM\,t})} \tag{8}$$

Consequentially, also the reaction rate can be determined explicitly at a certain time or, likewise, since the flow rate is constant, at a point along the flow path. The reaction takes place once the two solutions, as described in the previous section, mix. The mixing happens in the inlet tube, right after the T-junction (see Fig. 1). The residence time in the inlet tube, which is determined by the flow rate and the geometry of the inlet tube, is approximately 16 min. Since the residence time in the micro-fluidic cell is only a few seconds, we assume that the changes of the urea concentration are negligible. Therefore, the ureolysis reaction rate can be assumed to be constant throughout the micro-fluidic cell, while it is determined by the residence time in the inlet tube. Table 2 gives the relevant parameters to

Table 1 Concentrations and flow rate of the reactive solutions (based on (Weinhardt et al. 2020))

Solution	c_{urea} (mol/L)	c_{CaCl_2} (mol/L)	C_{JBM} (g/L)	Q [μL/s]
S_1	1/3	1/3	0	0.01
S_2	0	0	5	0.01
Mixed	1/6	1/6	2.5	0.02

Table 2 Kinetic and other parameters to estimate the ureolysis rate based on Eq. (6)

Symbol	Parameter	Value	Unit
$a_{u,0}$	Arrhenius-type kinetics coefficient	462.74	[L/(g s)]
$a_{u,T}$	Arrhenius-type kinetics coefficient	-4263.108	[K]
T	Temperature	296.15	[K]
C_{JBM}	Mass concentration of suspended urease (JBM)	2.5	[g/L]
$k_u(296.15)$	Rate coefficient at 296.15 Kelvin	2.592E-4	[L/(g s)]
t_{tube}	Residence time in the tube	16.36	[min]
$c_{urea}, 0$	Initial molar concentration at the T-junction	0.167	[mol/L]
$c_{urea,cell}$	Molar concentration of urea in the cell	0.088	[mol/L]
$r_{u,\,cell}$	Ureolysis rate in the cell	5.716E-5	[mol/(L s)]

determine the ureolysis rate in the cell, assuming that there is no accumulation or inactivation of urease in the inlet tubing and the porous domain and the urease concentration is constant at the injected concentration of $C_{JBM} = 2.5$ g/L.

2.3 Phase-Field Model

Multiphase problems can be modeled using a sharp- or a diffuse-interface approach. We consider here a diffuse-interface approach to allow for changes in topology, such as merging of crystal aggregates. Precisely, we rely on a phase-field model presented in (Rohde and von Wolff 2020). The model employs a phase-field parameter ϕ for the volume fraction of fluid. That is, $\phi = 1$ indicates the fluid phase and $\phi = 0$ indicates the solid precipitate. The interface separating the fluid phase from the precipitated calcium carbonate is approximated by a thin diffuse transition region of width ε. When the interface width ε approaches zero, the model converges to a classical sharp-interface model. Therefore, the interface width ε will be chosen small in comparison to the characteristic length scale of the micro-fluidic cell.

To present the model, we introduce as unknowns the phase-field parameter ϕ, the fluid velocity $\mathbf{v}$, the pressure p, and the inorganic carbon concentration c in the fluid. The model couples the equation for the transport, diffusion, and reaction of inorganic carbon

$$\partial_t(\phi c) + \nabla \cdot ((\phi \mathbf{v} + J)c) = \nabla \cdot (D\phi \nabla c) + \phi r_{u,cell} - r_{precip}(\phi, c) \tag{9}$$

with the Navier–Stokes equations in the fluid phase, given by

$$\nabla \cdot (\phi \mathbf{v}) = 0, \tag{10}$$

$$\partial_t(\rho\phi\mathbf{v}) + \nabla \cdot (\rho(\phi\mathbf{v} + J) \otimes \mathbf{v}) = -\phi\nabla p + \nabla \cdot (2\gamma\nabla^s\mathbf{v}) - \frac{12\gamma}{h^2}\mathbf{v} - d(\phi)\mathbf{v}. \tag{11}$$

The phase-field parameter ϕ is determined by the Cahn–Hilliard evolution

$$\partial_t\phi + \nabla \cdot J = -\frac{r_{precip}(\phi, c)}{c^*}, \qquad J = -M\nabla\mu, \qquad \mu = \frac{W'(\phi)}{\varepsilon} - \varepsilon\nabla^2\phi. \tag{12}$$

Here, ρ is the fluid density, γ is the fluid viscosity, D is the diffusion coefficient of carbonate ions, and c^* is the molar density of the precipitated calcium carbonate. Values are taken

from literature and listed in Table 1. From the Cahn–Hilliard evolution, we have a phase-field mobility M and a double-well potential W with minima at 0 and 1.

Equations (10), (11) are the Navier–Stokes equations, modified as follows. Firstly, they are formulated only for the fluid fraction ϕ. Secondly, the model is employed only in the two-dimensional geometry of the micro-fluidic cell. From the assumption of a parabolic flow profile across the height h of the cell, an additional drag term enters the Navier–Stokes equation, analogous to the derivation of a Hele–Shaw flow (Lamb 1932). Lastly, the model should ensure $\mathbf{v} \approx 0$ in the precipitated calcium carbonate, i.e., when $\phi = 0$, and a no-slip condition between the solid and fluid phase. For this, the term $d(\phi)\mathbf{v}$ with

$$d(\phi) = d_0(1-\phi)^2$$

is introduced and the constant d_0 is chosen sufficiently large. For more details, on the choice of d_0, see Remark 2.3 in (Rohde and von Wolff 2020).

Equation (9) has two reaction terms on the right-hand side. The term $r_{\text{u,cell}}$ describes the hydrolysis of urea. As discussed in Sect. 2.2, this will depend on temperature, activity of urea, and mass concentration of enzyme. These values are assumed to be approximately constant in the micro-fluidic cell, as the time for fluid to pass through the cell is in the order of seconds. The value for $r_{\text{u,cell}}$ is determined in Sect. 2.2 and is given in Table 2. In (Rohde and von Wolff 2020), no such bulk-reaction term is considered, but the extension of the analysis to the case with constant $r_{\text{u,cell}}$ is straightforward. The second reaction term, r_{precip}, models the precipitation of calcium carbonate and is given by

$$r_{\text{precip}}(\phi, c) = k_{\text{precip}}(c - c_{\text{eq}}) \max\left(\phi(1-\phi) - 0.1\ ,\ 0\right). \tag{13}$$

The reaction rate is proportional to the oversaturation $c - c_{\text{eq}}$ of inorganic carbon. The ϕ -dependence of r_{precip} ensures that precipitation only occurs at the interface to pre-existing crystals. As the precipitation process is fast in comparison to the hydrolysis of urea, it is assumed to be an equilibrium reaction. The choice for k_{precip} is therefore not from literature, but instead big enough that equilibrium conditions can be observed at the interface at all times (Table 3).

Table 3 Parameters for the phase-field model

Symbol	Parameter	Value	Unit
c^*	Molar density of $CaCO_3$	27.1	[mol/L]
c_{eq}	Fully saturated carbonate concentration	1.4E-04	[mol/L]
D	Diffusion coefficient	8.04E-10	[m^2/s]
ρ	Density of water	0.997E03	[kg/m^3]
γ	Viscosity of water	1.01E-03	[kg/(m s)]
d_0	Momentum dissipation in solid phase	1E06	[kg/(m^3 s)]
$r_{\text{u,cell}}$	Reaction rate of urea hydrolysis	5.716E-05	[mol/(L s)]
h	Height of micro-fluidic cell	8.5E-05	[m]
k_{precip}	Precipitation rate	200	[1/s]
ε	Interface width	2E-06	[m]
M	Phase-field mobility	1E-05	dimensionless

2.4 Numerical Implementation

The Cahn–Hilliard evolution (12) does not ensure $0 \leq \phi \leq 1$, i.e., the fluid's volume fraction ϕ can exceed the physically relevant regime. To ensure that the phase-field model (10) - (12) does not degenerate because of $\phi \leq 0$, we modify our system exactly as in (Rohde and von Wolff 2020). A new small number δ is introduced and quantities depending on ϕ have to be modified by δ to ensure positivity. The choice $\delta = 5\text{E-}03$ keeps the numerical system stable while barely perturbing the solution.

The equations are discretized by a finite element method, with Taylor–Hood elements for velocity $\mathbf{v}$ and pressure p, and second-order Lagrange elements for concentration c and phase-field parameter ϕ. All equations are discretized fully implicit in time, i.e., by implicit Euler method. We do not solve the system monolithically, but instead iterate between solving the Navier–Stokes equations (10), (11) and equations (9), (12) until convergence.

The implementation was done in Dune-PDELab (Bastian et al. 2010) using ALUGrid (Alkämper et al. 2016). This comes with the benefit of adaptive grid generation. The phase-field model requires small grid cells to resolve the diffuse interface, while grid cells at larger distance to the interfaces can be considerably larger. Fig. 2 shows a section of the grid containing one crystal aggregate. The grid is adapted after each timestep to account for the evolving interfaces.

One major challenge for the simulation is the relatively fast flow in the order of mm/s compared to the total runtime of the experiment of multiple hours. The flow regime introduces a severe restriction on the timestep dt. For the simulation of the full system, including the flow, small timesteps of size $dt = 0.01s$ are used, making the simulation computationally demanding. To tackle this problem, a special timestepping is introduced; small timesteps are needed to resolve the interplay between transport, diffusion, and reaction. After a few seconds in the simulation, transport, diffusion and reaction balance each other and all unknowns change on the timescale of minutes. This is facilitated by the laminar flow regime. At this stage, the only process leading to a change in unknowns is the growth of precipitated calcium carbonate. This growth happens rather slowly, i.e., on a larger timescale, and it is now possible to only update the phase field ϕ using

$$\partial_t \phi = -\frac{r_{\text{precip}}(\phi, c)}{c^*} \tag{14}$$

with a larger timestep $dt = 10s$, while keeping all other unknowns constant. After this big timestep, smaller timesteps with the full system are again performed until a quasi-static state is reached. A sketch of such a timestepping procedure is shown in Fig. 3

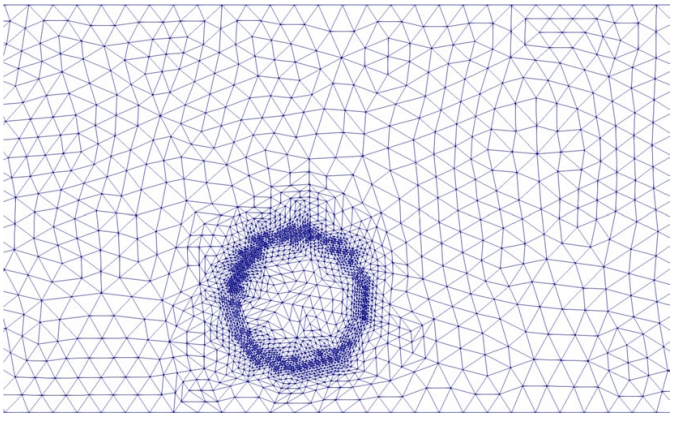

Fig. 2 Part of the grid used for the simulation in Sect. 3. The grid is refined at the interface between the fluid phase and the precipitated calcium carbonate

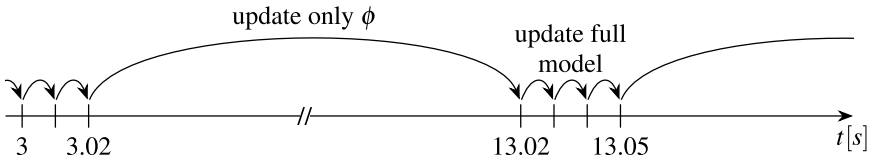

Fig. 3 Sketch of the timestepping algorithm, with small and big timesteps

2.5 Calculation of the Inflow Conditions

The simulation of the experiment is performed on the domain consisting of pore throats and pore bodies, without the inlet and outlet region of the micro-fluidic cell, see Fig. 1. At the inflow boundary of the simulation domain, both fluid velocity $\mathbf{v}_{\text{in}}$ and inorganic carbon concentration c_{in} have to be prescribed. The velocity is chosen as a parabolic flow profile with total flow rate of 0.02 μL/s. In contrast, it is more difficult to determine the inorganic-carbon concentration c_{in} at the inflow boundary.

The hydrolysis of urea begins as soon as the reactant solutions mix in the T-junction before the inlet tube. Due to the residence time in the tube of 16 min, see Table 2, the inorganic carbon produced in this time cannot be neglected. While integrating the reaction rate (6) over the residence time gives an upper bound for c_{in}, the actual value is much lower because of precipitation in the inflow tube and the inlet area of the micro-fluidic cell.

Therefore, to determine the concentration c_{in}, we have to take into consideration the distribution of precipitated carbonate in the inlet area of the micro-fluidic cell. We use the knowledge about the model reaching a quasi-static state as described in Sect. 2.4. In case the inlet area is long enough, this state will be reached before the inflow boundary of the main simulation. Figure 4 shows a picture of the inlet area taken at the end of the experiment. For the simulation, a section S of the inlet area is used as representative for the whole inlet area. This justifies using periodic boundaries at inflow and outflow boundary of S. Now, the flow profile around the precipitated carbonate can be calculated by solving for steady-state solutions of (10), (11) in S. Next, the inorganic-carbon concentration c in the inlet section is determined by

$$\nabla \cdot (\phi \mathbf{v} c) = \nabla \cdot (D\phi \nabla c) + \phi r_{\text{u,cell}} - r_{\text{precip}}(\phi, c). \tag{15}$$

This equation is a steady state version of (9). The concentration c_{in} is then calculated as the flux average

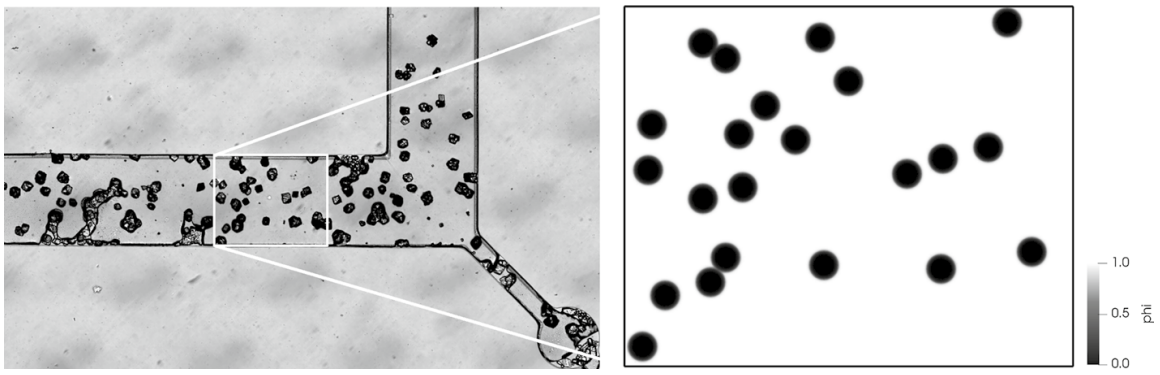

Fig. 4 Left: Calcite precipitation in the inlet area after the experimental run. A representative section S is highlighted by a white-colored boundary. Right: Simplified precipitate distribution in the section S used for simulation

$$c_{\text{in}} = \frac{\int_S c\phi \mathbf{v} \cdot \mathbf{e}_1 dx}{\int_S \phi \mathbf{v} \cdot \mathbf{e}_1 dx}$$

where $\mathbf{e}_1$ is the unit vector pointing from inflow to outflow boundary of S. We obtain the slightly oversaturated inflow condition $c_{\text{in}} = 3.150E-04$ mol/l.

3 Results and Discussion

We compare results (Weinhardt et al. 2020) of the experiment described in Sect. 2.1 with the mathematical model of Sect. 2.3. The exact locations of the points of nucleation are different for each repetition of the experiment; they are obviously subject to effects which we have to denote for now as random since we attribute them to conditions that are not easy to analyze in the details, such as impurities of the PDMS surface as hypothesized in (Weinhardt et al. 2020). In any case, we cannot determine or predict the points of nucleation a-priori, thus we use here data from an experimental run 52 min after start to determine the initial nuclei for the simulation model.

The model leaves its range of validity in approaching conditions of clogging; it is therefore stopped shortly before clogging. We compare the results of the final state of the simulation with a corresponding state of the experimental run that shows similar clogging behavior. In the comparison, we characterize crystal aggregates by centroid and volume.

Figure 5 shows the initial and the final distribution of precipitated calcite in both experiment and simulation. All crystal aggregates show some growth, and we observe near-clogging at the end of the third pore body. For further investigation and more convenient referencing, we number the crystal aggregates from left to right, as shown in Fig. 6. The three crystal aggregates at the end of the third pore body are excluded from the comparison and thus numbering, since they merged during the experiment. Also, new nucleation points forming after the initial 52 min are not considered, as they would have to be placed into the running simulation. The black dot in the pore throat between the third and the fourth pore body is an impurity of the micro-fluidic cell and not a calcite crystal.

While the final state of the simulation and the corresponding state of the experimental run match fairly well, the elapsed time in experiment and model is different. The pictures of the experiment shown in Fig. 5 are at 52 min and 112 min after the start of the

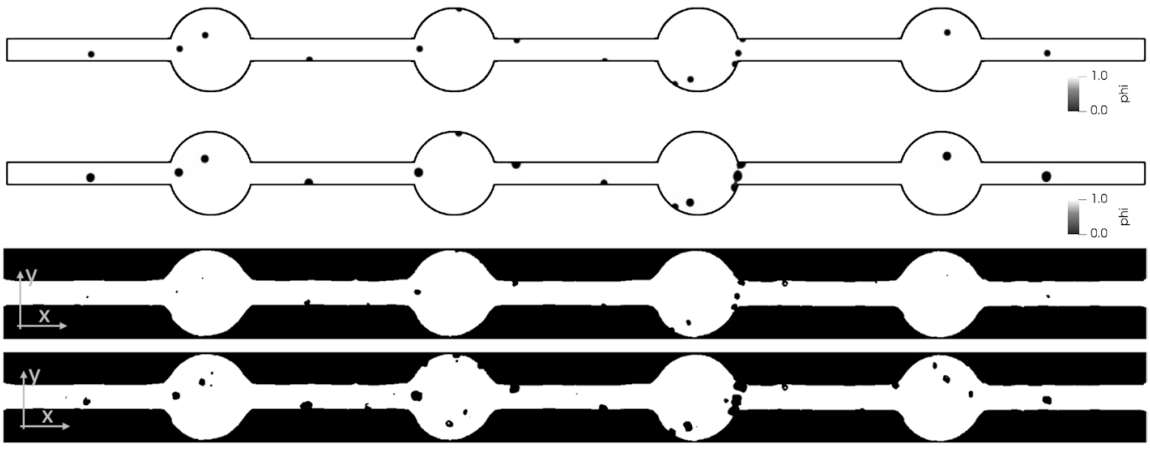

Fig. 5 Top: Fluid volume fraction ϕ in initial and final state of the simulation. Bottom: Corresponding states of the experimental run

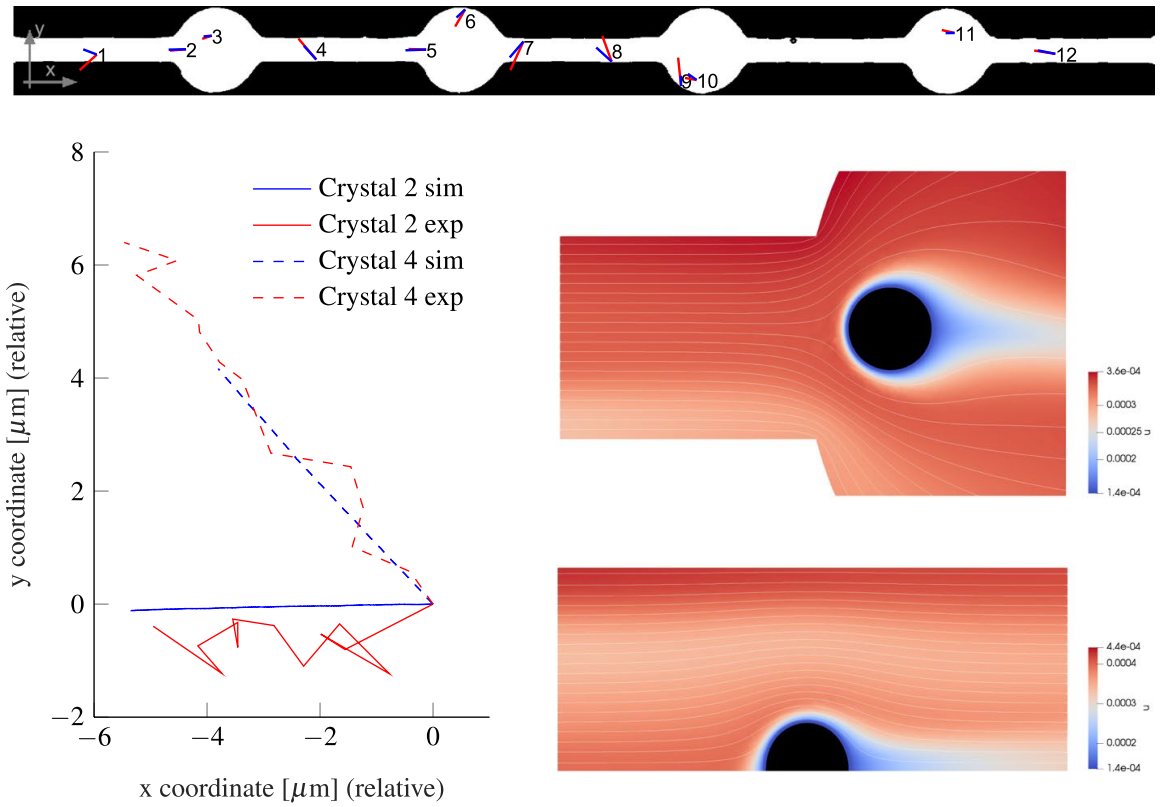

Fig. 6 Growth of precipitates; top: Change of the position of the centroids as vector (20 times enlarged) for simulation (blue) and the experiment (red); bottom left: change of the position of centroids relative to the initial location for the crystal aggregates 2 and 4; bottom right: streamlines and inorganic carbon concentration c around the crystal aggregates 2 and 4, obtained from the simulation

experiment. Compared to the elapsed 60 min, the simulation reaches its final state after 287 min. There are several reasons for this. Firstly, the model is two-dimensional and therefore cannot capture all effects of flow around the precipitates. In particular, it assumes that crystal aggregates span the whole height of the micro-fluidic cell, i.e., they form cylindrical shapes. Weinhardt et al. (2020) show that this is not true and this will be discussed further in Sect. 3.2. Secondly, the model neglects electrodiffusion, which has been shown to enhance the precipitation process in similar models, see (Zhang and Klapper 2011). Lastly, both the ureolysis rate $r_{\mathrm{u,cell}}$ and the determination of the inorganic carbon concentration c_{in} at the inflow boundary are subject to uncertainty. We find from multiple simulation runs that the crystal-growth rate is approximately reciprocal to $r_{\mathrm{u,cell}}$.

3.1 Movement of Centroids

We determine the centroid of each crystal aggregate in the simulation by integrating over an area containing the crystal aggregate. For the experimental data, the same is done after image segmentation. In Fig. 6, the evolution of the centroids relative to the initial position is shown.

In both experiment and simulation, it can be observed that the values of the x-coordinate of the centroids decrease over time, i.e., the crystal aggregates grow in upstream direction. To comprehend this, we exemplary consider crystal aggregates with numbers 2 and 4. In Fig. 6, the inorganic carbon concentration around crystal aggregate 5 is shown. The oversaturated calcium carbonate gets transported to the upstream side of the aggregate

and precipitates there due to the fast timescale of precipitation. When the fluid reaches the downstream side of the aggregate, little oversaturation of calcium carbonate is left and therefore nearly no precipitation is observed at this side.

We conclude from the simulation that the growth process is governed by the interplay of transport and diffusion close to the crystal aggregate. A lower flow rate and more diffusion lead to a less pronounced growth in the upstream direction. Indeed, this can be observed when comparing pore throats, which have a high flow rate, with pore bodies. Figure 6 shows that crystal aggregates located in pore throats grow more in the upstream direction than crystal aggregates located in pore bodies.

A second observation is that in both experiment and simulation the centroids mainly grow toward the center of the channel, as seen exemplary for crystal aggregate 4 in Fig. 6. The primary cause for this effect is that once the precipitate reaches a wall, it cannot grow further in this direction. Another cause is that the flow velocity close to the wall is small. Therefore, more calcium carbonate gets transported to the side of the crystal aggregate facing toward the center of the channel than to the most upstream point. Consequently, the centroid moves toward the center of the channel.

In contrast to the simulation, the centroid of crystal aggregate 1 moves toward the wall in the experiment, see Fig. 6. This is one of the major differences observed between model and experiment. One possible reason for this is a new nucleation point in front of crystal aggregate 1 that formed only during the experiment. This new nucleation point cannot be taken into account in the simulation, as it was not present in the model's initial configuration. Another possible reason is challenges in image segmentation, due to the reflective surface of the crystal aggregate.

In conclusion, the model matches the observed data well, and thus can capture dominating mechanisms for determining crystal-growth directions in this micro-fluidic EICP setup. Growth of the crystal aggregates leads to a shift of centroids in the upstream direction, and this effect is more pronounced in pore throats, where the flow rate is higher.

3.2 Growth of Crystal Aggregates

While the previous section focused on the direction of growth of the precipitates, we compare now the volume change of the crystal aggregates. The mathematical model is two-dimensional and assumes that ϕ is constant across the height of the micro-fluidic cell. Therefore, the volume of the precipitates can be computed by integrating over the calcite fraction $1 - \phi$ and subsequently multiplying by the height of the cell. The three-dimensional shape of the crystal aggregates is therefore obtained by extruding the two-dimensional data, which cannot analogously be applied for the experimental data. It has been shown by (Weinhardt et al. 2020), that the most suitable shape approximation for estimating the (3D) volume of the precipitates in micro-fluidic cells from (2D) optical microscopy data is the spheroidal shape. A representative radius is calculated from the projected area of the aggregates. Based on this radius, the volume can be derived for the assumption of a spheroidal shape. This approach is described in (Weinhardt et al. 2020) and is based on the idea given in (Kim et al. 2020). During the here investigated time frame of 60 min the radii of the crystal aggregates range from approximately 5 μm to 35 μm. Compared to the height of the channel of 85 μm, the radii of the crystal aggregates are smaller than half of the channel height. Therefore, the crystal aggregates are not expected to reach all the way from the bottom to the top of the micro-fluidic cell.

In Fig. 7(a), the growth of the precipitates is plotted over the velocity magnitude at the initial position of the precipitates. These velocity values are obtained from a stationary flow simulation without any precipitates present. More precisely, this means solving a stationary version of equations (10) and (11) with $\phi = 1$ and $J = 0$ everywhere. We will call velocities obtained from this simulation initial velocities.

As the growth of the precipitates is mainly driven by the transport of carbonate ions to the crystal aggregates, the initial velocity at the nucleation points gives a good estimate for the carbonate supply at specific locations in the domain. Exemplary, we compare crystal aggregates 4, 5 and 6, as labeled in Fig. 6. Crystal aggregate 6 is located at the outer part of a pore body. This leads to a relatively small initial velocity and a slow growth of volume. In contrast, crystal aggregate 5 lies in the center of the pore body and right after a pore throat. This implies a high initial velocity and, therefore, a large amount of carbonate ions passing by. Crystal aggregate 4 is in a pore-throat, where generally the velocities are high due to the reduced cross-sectional area. However, it sits right at the wall of the throat, where the velocity is reduced due to the shear forces caused by the wall friction.

From this analysis, we conclude that there is a tendency of the crystal aggregates to grow faster and bigger where the initial velocities are higher. This is directly linked to the supply of carbonate ions. The linear regressions, illustrated as dashed lines in Fig. 7(a), show a good agreement between simulation and the experiments. As already mentioned in Sect. 3.1, crystal aggregate 1 is again an obvious outlier and is therefore excluded for determining the linear regression of the experimental data. The coefficient of determination (R^2) for the simulation data clearly indicates a linear trend, while the one for the experimental Dataset indicates a weaker, but still significant trend.

However, the initial velocity does not take into account that the fluid flow is influenced by the precipitates. Especially in pore-throats precipitates reduce the cross-sectional area and lead therefore to higher velocities. As our introduced mathematical model includes the influence of precipitates on the fluid flow, we expect a better correlation when evaluating the velocity for the full model. The result is shown in Fig. 7(b), where we use the velocity

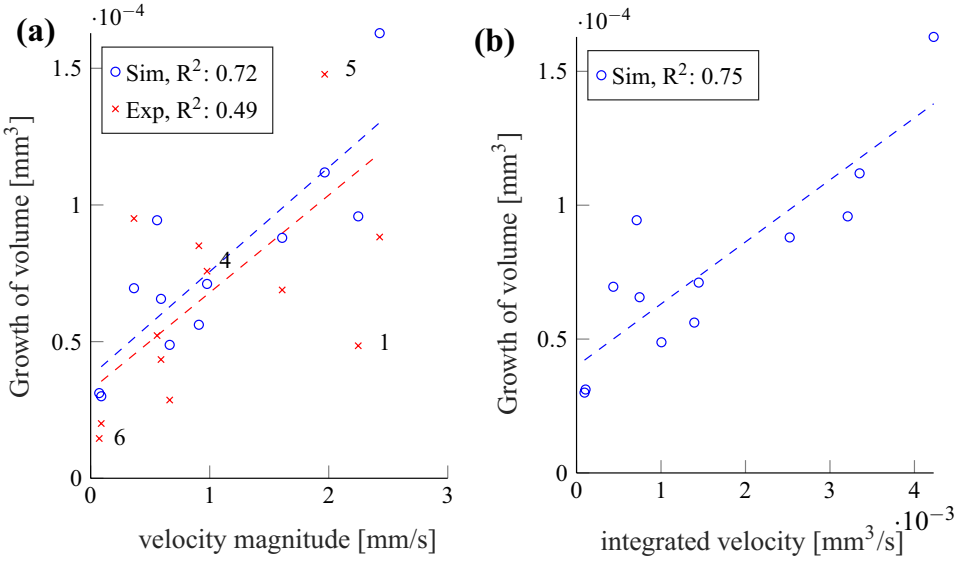

Fig. 7 Growth of precipitates; (**a**) Total growth of volume over the velocity magnitude at the initial position of the crystal aggregates, obtained from stationary Stokes simulation without precipitates. (**b**) Total growth of the volume over the velocity integrated over the area around the crystal aggregates, as obtained from the numerical model (9)-(12)

field obtained from the full numerical model for the initial calcite distribution. We cannot evaluate the velocity at the center of the crystal aggregates, as there is no fluid flow in the precipitates. Instead, we now integrate the magnitude of the velocity over a disk shaped area around the crystal aggregates. The center of the disk coincides with the center of the crystal aggregate, and the radius is 1.8 times the diameter of the crystal aggregate.

Compared to Fig. 7(a), the results in Fig. 7(b) show an more evident linear correlation between the velocity magnitude close to the precipitates and the volume growth of the precipitates. The coefficient of determination for the simulation increased from 0.72 to 0.75. We conclude that the velocity field plays a significant role for the growth of the precipitates and the influence of precipitates on the flow field should not be neglected.

4 Conclusions

We have developed a phase-field approach for modeling crystal growth in enzymatically induced calcite precipitation and compared it to micro-fluidic experiments. Without any additional calibration there is a good qualitative agreement between model and experiment. Quantitatively, there is a very good agreement for the movement of centroids, and a good agreement for the growth of crystal aggregates. Only the predicted time until near-clogging differs significantly.

This joint experimental and numerical study allows for new insights into the dominant processes and mechanisms involved in the growth of crystal aggregates. We have seen that growth is strongly dependent on the flow conditions, i.e., the flow field and corresponding concentrations of the inorganic carbon. The concentrations are subject to local changes due to reaction but also due to the complexity of the flow field which is influenced by the geometry of the flow cell and the pattern of precipitates. In particular, for a single crystal aggregate, the growth is determined by the interplay between transport around the aggregate and diffusion toward the surface.

It has been observed consistently in experiment and simulation that nuclei show a clear tendency toward growing upstream and toward the center of the channel. Additionally, the growth rate is correlated with the magnitude of flow velocity, leading to a faster growth in the center of the channel.

A better understanding of the pore-scale mechanisms involved in EICP-related growth of crystals will contribute to developing optimization strategies for an effective use of the EICP technology. Perspectively, the phase-field approach presented here can be further developed to describe also microbially induced precipitation (MICP), where the mechanisms of growth are even more complex due to the involvement of biofilm in the pore space.

Acknowledgements We thank Matthijs de Winter for the image provided from the inlet channel of the micro-fluidic cell in Fig. 4

Funding Open Access funding enabled and organized by Projekt DEAL. Funded by the Deutsche Forschungsgemeinschaft (DFG, German Research Foundation)—Project Number 327154368 – SFB 1313. We thank the German Research Foundation (DFG) for supporting this work by funding Johannes Hommel by the DFG Project Number 380443677.

Compliance with ethical standards

Conflict of interest The authors declare that they have no conflict of interest.

References

Alkämper, M., Dedner, A., Klöfkorn, R., Nolte, M.: The DUNE-ALUGrid module. Archive Numer. Software **4**(1), 1–28 (2016)

Bastian, P., Heimann, F., Marnach, S.: Generic implementation of finite element methods in the distributed and unified numerics environment (dune). Kybernetika **2**, (2010)

Blunt, M.J., Bijeljic, B., Dong, H., Gharbi, O., Iglauer, S., Mostaghimi, P., Paluszny, A., Pentland, C.: Pore-scale imaging and modelling. Adv. Water Resour. **51**(supplement C), 197–216 (2013). https://doi.org/10.1016/j.advwatres.2012.03.003

Bringedal, C., von Wolff, L., Pop, I.S.: Phase field modeling of precipitation and dissolution processes in porous media: upscaling and numerical experiments. Multiscale Model. Simulat. **18**(2), 1076–1112 (2020). https://doi.org/10.1137/19M1239003

Cunningham, A., Class, H., Ebigbo, A., Gerlach, R., Phillips, A., Hommel, J.: Field-scale modeling of microbially induced calcite precipitation. Comput. Geosci. **23**, 399–414 (2019). https://doi.org/10.1007/s10596-018-9797-6

Cuthbert, M., McMillan, L., Handley-Sidhu, S., Riley, M., Tobler, D., Phoenix, V.: A field and modeling study of fractured rock permeability reduction using microbially induced calcite precipitation. Environ. Sci. Technol. **47**(23), 13637–13643 (2013). https://doi.org/10.1021/es402601g

Feder, M.J., Morasko, V.J., Akyel, A., Gerlach, R., Phillips, A.J.: Temperature-dependent inactivation and catalysis rates of plant-based ureases for engineered biomineralization. Engineering Reports (2020). In Revision, Manuscript ID # ENG-2019-12-0913

Hamdan, N., Kavazanjian, E.: Enzyme-induced carbonate mineral precipitation for fugitive dust control. Géotechnique **66**(7), 546–555 (2016). https://doi.org/10.1680/jgeot.15.P.168

Hommel, J., Akyel, A., Frieling, Z., Phillips, A.J., Gerlach, R., Cunningham, A.B., Class, H.: A numerical model for enzymatically induced calcium carbonate precipitation. Appl. Sci. **10**, 4538 (2020)

Hommel, J., Coltman, E., Class, H.: Porosity-permeability relations for evolving pore space: A review with a focus on (bio-)geochemically altered porous media. Transp. Porous Media **124**(2), 589–629 (2018). https://doi.org/10.1007/s11242-018-1086-2

Kappaun, K., Piovesan, A.R., Carlini, C.R., Ligabue-Braun, R.: Ureases: historical aspects, catalytic, and non-catalytic properties–a review. J. Adv. Res. **13**, 3–17 (2018). https://doi.org/10.1016/j.jare.2018.05.010

Karadimitriou, N.K., Joekar-Niasar, V., Hassanizadeh, S.M., Kleingeld, P.J., Pyrak-Nolte, L.J.: A novel deep reactive ion etched (drie) glass micro-model for two-phase flow experiments. Lab Chip **12**, 3413–3418 (2012). https://doi.org/10.1039/C2LC40530J

Karadimitriou, N.K., Musterd, M., Kleingeld, P.J., Kreutzer, M.T., Hassanizadeh, S.M., Joekar-Niasar, V.: On the fabrication of pdms micromodels by rapid prototyping, and their use in two-phase flow studies. Water Resour. Res. **49**(4), 2056–2067 (2013). https://doi.org/10.1002/wrcr.20196

Kim, D.H., Mahabadi, N., Jang, J., van Paassen, L.A.: Assessing the kinetics and pore-scale characteristics of biological calcium carbonate precipitation in porous media using a microfluidic chip experiment. Water Resour. Res. **56**(2), 10.1029/2019WR02542025420 (2020). https://doi.org/10.1029/2019WR025420

Lamb, H.: Hydrodynamics, 6th edn. Cambridge University Press, Cambridge (1932)

Lauchnor, E.G., Schultz, L.N., Bugni, S., Mitchell, A.C., Cunningham, A.B., Gerlach, R.: Bacterially induced calcium carbonate precipitation and strontium co-precipitation in a porous media flow system. Environ. Sci. Technol. **47**(3), 1557–1564 (2013)

Minto, J.M., Lunn, R.J., Mountassir, G.E.: Development of a reactive transport model for field-scale simulation of microbially induced carbonate precipitation. Water Resour. Res. (2019). https://doi.org/10.1029/2019WR025153

Minto, J.M., Tan, Q., Lunn, R.J., Mountassir, G.E., Guo, H., Cheng, X.: Microbial mortar-restoration of degraded marble structures with microbially induced carbonate precipitation. Construct. Build. Mater. **180**, 44–54 (2018). https://doi.org/10.1016/j.conbuildmat.2018.05.200

Mitchell, A.C., Ferris, F.G.: The coprecipitation of Sr into calcite precipitates induced by bacterial ureolysis in artificial groundwater: Temperature and kinetic dependence. Geochimica et Cosmochimica Acta **69**(17), 4199–4210 (2005). https://doi.org/10.1016/j.gca.2005.03.014

Molins, S., Soulaine, C., Prasianakis, N.I., Abbasi, A., Poncet, P., Ladd, A.J.C., Starchenko, V., Roman, S., Trebotich, D., Tchelepi, H.A., Steefel, C.I.: Simulation of mineral dissolution at the pore scale with evolving fluid-solid interfaces: review of approaches and benchmark problem set. Computat. Geosci. (2020). https://doi.org/10.1007/s10596-019-09903-x

Molins, S., Trebotich, D., Steefel, C.I., Shen, C.: An investigation of the effect of pore scale flow on average geochemical reaction rates using direct numerical simulation. Water Resour. Res. **48**, 3 (2012). https://doi.org/10.1029/2011WR011404

Mujah, D., Shahin, M.A., Cheng, L.: State-of-the-art review of biocementation by microbially induced calcite precipitation (MICP) for soil stabilization. Geomicrobiol. J. **34**(6), 524–537 (2017). https://doi.org/10.1080/01490451.2016.1225866

Nassar, M.K., Gurung, D., Bastani, M., Ginn, T.R., Shafei, B., Gomez, M.G., Graddy, C.M.R., Nelson, D.C., DeJong, J.T.: Large-scale experiments in microbially induced calcite precipitation (MICP): reactive transport model development and prediction. Water Resour. Res. **54**, 480–500 (2018). https://doi.org/10.1002/2017WR021488

Nemati, M., Voordouw, G.: Modification of porous media permeability, using calcium carbonate produced enzymatically in situ. Enzyme Microbial Technol. **33**(5), 635–642 (2003). https://doi.org/10.1016/S0141-0229(03)00191-1

Neupane, D., Yasuhara, H., Kinoshita, N., Unno, T.: Applicability of enzymatic calcium carbonate precipitation as a soil-strengthening technique. ASCE J. Geotech. Geoenviron. Eng. **139**, 2201–2211 (2013)

Phillips, A., Gerlach, R., Lauchnor, E., Mitchell, A., Cunningham, A., Spangler, L.: Engineered applications of ureolytic biomineralization: A review. Biofouling **29**(6), 715–733 (2013). https://doi.org/10.1080/08927014.2013.796550

Phillips, A., Lauchnor, E., Eldring, J., Esposito, R., Mitchell, A., Gerlach, R., Cunningham, A., Spangler, L.: Potential CO_2 leakage reduction through biofilm-induced calcium carbonate precipitation. Environ. Sci. Technol. **47**(1), 142–149 (2013). https://doi.org/10.1021/es301294q

Phillips, A.J., Cunningham, A.B., Gerlach, R., Hiebert, R., Hwang, C., Lomans, B.P., Westrich, J., Mantilla, C., Kirksey, J., Esposito, R., Spangler, L.H.: Fracture Sealing with Microbially-Induced Calcium Carbonate Precipitation: A Field Study. Environ. Sci. Technol. **50**, 4111–4117 (2016). https://doi.org/10.1021/acs.est.5b05559

Ray, N., Oberlander, J., Frolkovic, P.: Numerical investigation of a fully coupled micro-macro model for mineral dissolution and precipitation. Computat. Geosci. **23**, 1173–1192 (2019)

Redeker, M., Rohde, C., Sorin Pop, I.: Upscaling of a tri-phase phase-field model for precipitation in porous media. IMA J. Appl. Math. **81**(5), 898–939 (2016). https://doi.org/10.1093/imamat/hxw023

Rohde, C., von Wolff, L.: A ternary Cahn-Hilliard-Navier-Stokes model for two-phase flow with precipitation and dissolution. Math. Models Methods Appl. Sci. (2020). https://doi.org/10.1142/S0218202521500019

Takaki, T.: Phase-field modeling and simulations of dendrite growth. ISIJ Int. **54**(2), 437–444 (2014). https://doi.org/10.2355/isijinternational.54.437

van Duijn, C.J., Pop, I.S.: Crystal dissolution and precipitation in porous media: Pore scale analysis. J. die reine und angewandte Mathematik **2004**(577), 171–211 (2004)

van Noorden, T., Eck, C.: Phase field approximation of a kinetic moving-boundary problem modelling dissolution and precipitation. Interfaces Free Bound. **13**(1), 29–55 (2011). https://doi.org/10.4171/IFB/247

van Paassen, L., Ghose, R., van der Linden, T., van der Star, W., van Loosdrecht, M.: Quantifying biomediated ground improvement by ureolysis: large-scale biogrout experiment. J. Geotech. Geoenviron. Eng. **136**(12), 1721–1728 (2010)

Weinhardt, F., Class, H., Vahid Dastjerdi, S., Karadimitriou, N., Lee, D., Steeb, H.: Optical Microscopy and pressure measurements of Enzymatically Induced Calcite Precipitation (EICP) in a micro-fluidic cell. DaRUS (2020). https://doi.org/10.18419/darus-818

Weinhardt, F., Class, H., Vahid Dastjerdi, S., Karadimitriou, N. K., Lee, D., Steeb, H.: Experimental methods and imaging for enzymatically induced calcite precipitation in a microfluidic cell. Accepted in Water Resources Research (2021). https://doi.org/10.1029/2020WR029361

Whitaker, J.M., Vanapalli, S., Fortin, D.: Improving the strength of sandy soils via ureolytic $caco_3$ solidification by Sporosarcina ureae. Biogeosci. Discuss. **2018**, 1–22 (2018). https://doi.org/10.5194/bg-2017-517

van Wijngaarden, W.K., van Paassen, L.A., Vermolen, F.J., van Meurs, G.A.M., Vuik, C.: A reactive transport model for biogrout compared to experimental data. Transp. Porous Media **111**(3), 627–648 (2016). https://doi.org/10.1007/s11242-015-0615-5

Wildenschild, D., Sheppard, A.P.: X-ray imaging and analysis techniques for quantifying pore-scale structure and processes in subsurface porous medium systems. Adv. Water Resour. Environ. Sci. Technol. **51**(Supplement C), 217–246 (2013). https://doi.org/10.1016/j.advwatres.2012.07.018

Woolley, M.A., van Paassen, L., Kavazanjian, E.: Impact on Surface Hydraulic Conductivity of EICP Treatment for Fugitive Dust Mitigation, pp. 132–140. https://doi.org/10.1061/9780784482834.015

Xia, Y., Whitesides, G.M.: Soft lithography. Angewandte Chemie Int. Edition **37**(5), 550–575 (1998)

Yoon, H., Valocchi, A.J., Werth, C.J., Dewers, T.: Pore-scale simulation of mixing-induced calcium carbonate precipitation and dissolution in a microfluidic pore network. Water Resour. Res. **48**, 2 (2012). https://doi.org/10.1029/2011WR011192

Zhang, T., Klapper, I.: Mathematical model of biofilm induced calcite precipitation. Water Sci. Technol. **61**(11), 2957–2964 (2010). https://doi.org/10.2166/wst.2010.064

Zhang, T., Klapper, I.: Mathematical model of the effect of electrodiffusion on biomineralization. Int. J. Non-Linear Mech. **46**(4), 657–666 (2011). https://doi.org/10.1016/j.ijnonlinmec.2010.12.008

A.3 Contribution 3: Spatiotemporal distribution of precipitates and mineral phase transition during biomineralization affect porosity-permeability relationships

Title	Spatiotemporal distribution of precipitates and mineral phase transition during biomineralization affect porosity-permeability relationships
Authors	**Felix Weinhardt**, Jingxuan Deng, Johannes Hommel, Samaneh Vahid Dastjerdi, Robin Gerlach, Holger Steeb, Holger Class
Journal	Transport in Porous Media
Publication status	published (May, 10, 2022)
copyright	open access (creative common)
DOI	https://doi.org/10.1007/s11242-022-01782-8
Dataset(s)	https://doi.org/10.18419/darus-1799

Table A.3: Metadata of contribution III

Transport in Porous Media
https://doi.org/10.1007/s11242-022-01782-8

Spatiotemporal Distribution of Precipitates and Mineral Phase Transition During Biomineralization Affect Porosity–Permeability Relationships

Microfluidic investigations

Felix Weinhardt[1] · Jingxuan Deng[2] · Johannes Hommel[1] · Samaneh Vahid Dastjerdi[4] · Robin Gerlach[3] · Holger Steeb[4] · Holger Class[1]

Received: 11 January 2022 / Accepted: 11 April 2022

Abstract

Enzymatically induced calcium carbonate precipitation is a promising geotechnique with the potential, for example, to seal leakage pathways in the subsurface or to stabilize soils. Precipitation of calcium carbonate in a porous medium reduces the porosity and, consequently, the permeability. With pseudo-2D microfluidic experiments, including pressure monitoring and, for visualization, optical microscopy and X-ray computed tomography, pore-space alterations were reliably related to corresponding hydraulic responses. The study comprises six experiments with two different pore structures, a simple, quasi-1D structure, and a 2D structure. Using a continuous injection strategy with either constant or step-wise reduced flow rates, we identified key mechanisms that significantly influence the relationship between porosity and permeability. In the quasi-1D structure, the location of precipitates is more relevant to the hydraulic response (pressure gradients) than the overall porosity change. In the quasi-2D structure, this is different, because flow can bypass locally clogged regions, thus leading to steadier porosity–permeability relationships. Moreover, in quasi-2D systems, during continuous injection, preferential flow paths can evolve and remain open. Classical porosity–permeability power-law relationships with constant exponents cannot adequately describe this phenomenon. We furthermore observed coexistence and transformation of different polymorphs of calcium carbonate, namely amorphous calcium carbonate, vaterite, and calcite and discuss their influence on the observed development of preferential flow paths. This has so far not been accounted for in the state-of-the-art approaches for porosity–permeability relationships during calcium carbonate precipitation in porous media.

Article Highlights

- We record a detailed pore geometry evolution during EICP with synchronized pressure measurements

✉ Felix Weinhardt
felix.weinhardt@iws.uni-stuttgart.de

Extended author information available on the last page of the article

Published online: 10 May 2022

- We observe that the porosity–permeability relationship is strongly influenced by the complexity of the pore structure (Quasi-1D vs. Quasi-2D)
- The evolution and preservation of flow paths during EICP treatment with constant flow can significantly affect the apparent permeability

Keywords Biomineralization · EICP · Microfluidics · Porosity–permeability relationship

1 Introduction

Biomineralization offers an environmentally more sustainable technology to replace the use of Portland cement (Terzis and Laloui 2018), which is known to be energy demanding and has significant impact on global CO_2 emissions (Andrew 2019). Microbially or enzymatically induced calcium carbonate precipitation (MICP/EICP) refers to a bio-geochemical process, which is already intensively investigated for its potential to substitute and complement the use of Portland cement in various applications of civil and environmental engineering (Nething et al. 2020; Phillips et al. 2013a; Rahman et al. 2020; Akyel et al. 2022). The overall process relies on the hydrolysis of urea and the precipitation of calcium carbonate:

$$CO(NH_2)_2 + 3H_2O \xrightarrow{[urease]} 2NH_4^+ + HCO_3^- + OH^- \tag{1}$$

$$HCO_3^- + Ca^{2+} \longrightarrow CaCO_3 \downarrow + H^+ \tag{2}$$

Urea ($CO(NH_2)_2$) hydrolyzes irreversibly into ammonium and inorganic carbon, which is in general a very slow reaction, but can be catalyzed by the enzyme urease. This can speed up the reaction by several orders of magnitude (Benini et al. 1999; Krajewska 2009, 2018). The most common approaches to obtain urease for geotechnical application are either extracting it from jack-bean meal—then referred to as EICP—or produce it locally using microbial activity—referred to as MICP. In order to induce the precipitation of calcium carbonate, a source for calcium ions has to be present, which, in this work, is ensured through the addition of calcium chloride and can be provided in the form of ice-melt on the commercial scale (Phillips et al. 2016; Kirkland et al. 2021).

The precipitation of calcium carbonate itself is a complex combination of nucleation, crystal growth, and changes of the crystal structure (van Paassen 2009). Calcium carbonate has six different polymorphs, i.e., calcite, aragonite, vaterite, mono-hydrocalcite, ikaite, and amorphous calcium carbonate (ACC). Their thermodynamic stability decreases from calcite to ACC (El-Sheikh et al. 2013). In accordance with Ostwald's step rule, usually the least-stable phase forms first, which then transforms into more stable polymorphs (Cöelfen and Antonietti 2008) [as cited in Wang et al. (2019b)]. Generally, calcite crystals are rhombohedral, vaterite is spherical, and ACC is irregularly shaped (Rodriguez-Blanco et al. 2011). Moreover, the density of ACC is lower ($\rho = 2.18$ g/cm^3) than that of calcite ($\rho = 2.71$ g/cm^3) or vaterite ($\rho = 2.65$ g/cm^3) (Rodriguez-Navarro et al. 2015; Nebel 2008).

EICP or MICP in porous media are typically applied for stabilizing soils or for creating and improving hydraulic barriers. In soil stabilization, the precipitated calcium carbonate acts as cement-stabilizing loose material, for example, to control fugitive dust or

to produce construction material, like bio-bricks or other more complex bio-cemented spatial structures (Arab et al. 2021; Nething et al. 2020; Hamdan and Kavazanjian 2016; Akyel et al. 2022). In this case, mechanical properties like Young's modulus and shear modulus are of great interest and have been extensively studied (van Paassen 2009; Dejong et al. 2013; Mujah et al. 2017). In creating hydraulic barriers, to prevent or to remediate leakages in the subsurface, the key parameter to be controlled is the intrinsic permeability, which is strongly coupled to the porosity. (Phillips et al. 2013a, b; Hommel et al. 2018). A useful tool to predict and plan field applications is numerical simulation on the scale of representative elementary volumes (REV) (Cunningham et al. 2019; Minto et al. 2019; Landa-Marbán et al. 2021), which inherently relies on upscaled porosity–permeability relationships (Ebigbo et al. 2012; Hommel et al. 2016). The literature provides many different approaches of porosity–permeability relationships, which are used to model pore-space alterations on the REV scale, like Kozeny–Carman type, Thullner biofilm relation, or Verma-Pruess type, to name only a few (Pandey et al. 2015; Thullner 2010; Verma and Pruess 1988). As reviewed by Hommel et al. (2018), many of them do not lead to fundamentally different permeability alterations compared to a simple power-law relationship with a suitable exponent η:

$$k/k_0 = (\phi/\phi_0)^{\eta}, \tag{3}$$

with k being the intrinsic permeability and ϕ the porosity; k_0 and ϕ_0 are the initial values, respectively. Therefore, this simple approach should be the first choice unless substantial pore-scale information is available and justifies more sophisticated approaches.

Recent studies addressed how pore-scale factors determine the evolution of porosity and permeability driven by pore-space alteration, like precipitation or biofilm growth:

Effects of biofilm growth have been investigated by Jung and Meile (2021) using Stokes simulations of an idealized system. They concluded that the Péclet (Pe) and the diffusive Damköhler (Da) numbers (see SI for their definition) determine the biofilm distribution. High Pe numbers result in a homogeneous distribution of the biofilm. As a consequence, the resulting porosity–permeability relationships are closer to the classical Kozeny–Carman relationship.

In contrast, high Da numbers lead to preferential biofilm growth. This leads to a rapid decrease in the permeability even though the reduction in the porosity is small.

Experimentally, there have been several studies on the laboratory-scale where biofilm accumulation and its effect on the hydrodynamics have been studied. Cunningham et al. (1991) used reactors filled with glass beads and different types of sand. Their results indicated substantial interaction between mass transport, hydrodynamics, and biofilm accumulation at the fluid-biofilm interface. Furthermore, naturally bioluminescent biofilm experiments in meso-scale flat plate reactors were performed in the work of Sharp et al. (1999). With dye tracer studies, they were able to visualize the formation of flow channels during a continuous injection of the nutrient solution. In a recent experimental approach, the effect of biofilm growth on the permeability has been studied using microfluidic glass cells (Hassannayebi et al. 2021). Based on their experimental approach, the main mechanisms for biofilm aggregation were identified as adsorption, filtration, and bacterial growth, resulting in the formation of preferential flow paths. Supported by numerical simulations, they hypothesized that the increased velocity in the remaining flow paths may prevent further biomass aggregation and keeps them open. This contradicts the conclusions of the numerical study of Jung and Meile (2021), since they did not account for detachment and subsequent filtering processes of the biomass.

Similar to the work of Jung and Meile (2021), a numerical study was performed by Niu and Zhang (2019), addressing how mineral precipitation—instead of biofilm growth—influences the permeability of a porous medium. Ni and Ratner (2008) looked at advection-dominated systems (Pe > 1) and distinguished between reaction-limited cases and transport-limited cases. In the reaction-limited case, the precipitates form uniformly at the solid–fluid interface resulting in a porosity–permeability relationship with a constant exponent. In contrast, for the transport-limited cases, the precipitated minerals develop mostly near the pore throats where the fluid velocity, and thus reactant supply, is relatively high. This in turn results in a more rapid reduction in the permeability for a given reduction in the porosity and, consequently, cannot be represented reliably by a simple power-law relationship with a constant exponent.

Recently, investigations which are more specific to the pore-scale phenomena in processes of MICP and EICP were reported. In an experimental study, Mountassir et al. (2014) investigated MICP treatment in fractures using flow cells with a length of 20 cm and fractures of varying widths (1–20 mm) and apertures (0.1–0.5 mm). They observed the formation of flow channels within a fracture during MICP treatment, which becomes more distinct as precipitation progresses. They conclude that the effect of channeling enhances precipitation in regions of low flow velocities, whereas it is inhibited in the remaining high velocity channels.

Wang et al. (2019a) showed in their experimental study that the use of a microfluidic chip made out of polydimethylsiloxane (PDMS) is beneficial for studying MICP on the pore-scale. They found that calcium carbonate crystals form both at narrow pore throats and in open pore bodies during no-flow conditions. In two follow-up studies, Wang et al. (2019b, 2021) observed through high-resolution optical microscopy crystals of different shape. They hypothesized them to be different calcium carbonate polymorphs, which evolve during a staged injection strategy of the cementation solution. They observed that during the initial stage of the precipitation process, mainly irregularly shaped $CaCO_3$ precipitates (assumed to be ACC) formed, which later transform to spherical or rhombohedral crystals (assumed to be vaterite and calcite, respectively). At later time scales, rhombohedral calcium carbonate (calcite) was the dominant shape.

In the work of (Zambare et al. 2020), the mineralogy of MICP was studied using single-cell drop-based microfluidics. Using Raman microspectroscopy, they found that ACC occurred first, followed by the formation of vaterite, while the ratio of ACC to vaterite decreased during time. Due to the observation of autofluorescence of the precipitates and further analysis using energy dispersive X-ray spectroscopy (EDX), they presumed the additional presence of calcite. This is in agreement with the hypothesis of Wang et al. (2021), that ACC forms first and is later on transformed into vaterite and calcite.

Kim et al. (2020) performed an EICP experiment in a glass cell using a staged injection strategy and observed the pore-space alteration with optical microscopy. Assuming a semispherical as well as a cylindrical shape of the precipitates to estimate the volume of the evolving precipitates, they were able to conclude on the kinetics of the precipitation process by comparing the results to a simplified kinetic model. The main focus of these microfluidic investigations was on the kinetics of the biomineralization process.

In contrast to that we recently developed an experimental workflow that combines optical microscopy and high-resolution X-ray computed tomography (μXRCT) together with continuous pressure measurements in order to investigate the hydraulic effects, like the reduction in the intrinsic permeability. This enables us to directly relate changes of the pore space to changes in permeability (Weinhardt et al. 2021a). The utilized microfluidic cell was PDMS-based and the pore geometry consisted of four linearly aligned pore bodies

connected with pore throats. Due to the simplified geometry, we were able to compare the experimental results with a mathematical model that couples reactive transport with phase changes due to precipitation (von Wolff et al. 2021).

We present in this study an analysis of both the previous experiments in the simple pore structure (*Quasi-1D-structure*) and additional new microfluidic experiments with a more complex pore structure (*Quasi-2D-structure*). A focus is put also on how different injection strategies, constant versus step-wise reduced inflow, affect precipitation and porosity–permeability relationships. In the *Quasi-1D-structure*, the location of individual precipitates, whether in a pore throat or in a pore body, for example, is expected to have a much larger effect on the porosity–permeability relationship than in the *Quasi-2D-structure*, where the porous medium offers more degrees of freedom for flow paths to develop. It is demonstrated that mechanisms like shearing off and redeposition of small precipitates, which strongly affect the development of flow paths, are dependent on these boundary conditions imposed in the experiments. And we discuss how this affects the parameterization of functions to approximate the obtained porosity–permeability relationships. Taking the perspective of a modeler, it is an important goal of this fundamental experimental study to derive porosity–permeability relationships also on a larger scale, i.e., the REV scale (Hommel et al. 2018), and we can show that preferential flow is a major process to consider. It is important to consider the occurrence of preferential flow development in the context of boundary conditions. Constant flux (Neumann-type boundary condition) might lead to the development of preferential flow paths, while constant pressure differences (Dirichlet-type boundary condition) might minimize the development of such preferential flow paths (Zhang and Klapper 2014).

Based on our results, we therefore hypothesize that the (co)existence and transformation of differently shaped polymorphs strongly influence the resulting permeability reduction which has so far not been discussed in literature.

2 Materials and Methods

In this work, two sets of experiments are considered with different designs of the porous medium and different injection strategies. The first set of experiments consists of three experiments using a PDMS-based microfluidic cell with a simple 1D structure and are referred to as *Quasi-1D-experiments 1-3*. The corresponding data set includes time-resolved images obtained from optical microscopy, flow rates, pressure measurements and a µXRCT dataset obtained from one of the experiments after reaching its final state. The data corresponding to this study are available at Weinhardt et al. (2021b) and Vahid Dastjerdi et al. (2021), while details on the experimental methods are given by Weinhardt et al. (2021a). In the second set of experiments, we used microfluidic glass cells with a more complex structure, referred to as *Quasi-2D-experiments 1-3*. Besides the structure and the material, also the injection strategy varies slightly compared to the *Quasi-1D-experiments*. The resulting dataset includes again time-resolved images of optical microscopy and synchronized flow and pressure data (Weinhardt et al. 2022). In the following, the microfluidic setup and the experimental procedure are described, including the fabrication and designs of the microfluidic cells, the preparation of the chemical solutions, and the injection strategies (2.1). Furthermore, the imaging techniques including optical microscopy and µXRCT scanning are described and the necessary steps of the processing are detailed (2.2).

2.1 Microfluidic Setup and Procedure

2.1.1 Preparation of Reactive Solutions

The reactive solutions were prepared according to the procedure and concentrations described in Weinhardt et al. (2021a): Solution 1 contained calcium chloride dihydrate and urea (MERCK©) at equimolar concentrations of 1/3 mol/L. Solution 2 contained the enzyme urease extracted from jack-bean meal (Sigma-Aldrich©). To prepare Solution 2, a jack-bean-meal suspension at a concentration of 5 g/L was stirred for 17 hours at 8 °C and subsequently filtered twice through a cellulose membrane with a filter size of 0.45 µm before use in experiments.

2.1.2 Microfluidic Cells

We used two different types of microfluidic cells: (1) a PDMS-based microfluidic cell for the *Quasi-1D-structure*; (2) a glass cell for the *Quasi-2D-structure*. The corresponding pore structures are shown in Fig. 1.

The PDMS-based cells were produced using the general workflow of soft lithography (Xia and Whitesides 1998; Karadimitriou et al. 2013). The microfluidic cell consists of an inlet channel, an outlet channel, and two channels connected to the pressure sensors (type MPS0/MPS3 from Elveflow, Paris, France). The domain of interest in this case is the pore structure that consists of four pore bodies with a diameter of $D_{\text{pore}} = 500$ µm connected with pore throats with a width of $D_{\text{throat}} = 125$ µm. All features are extruded in

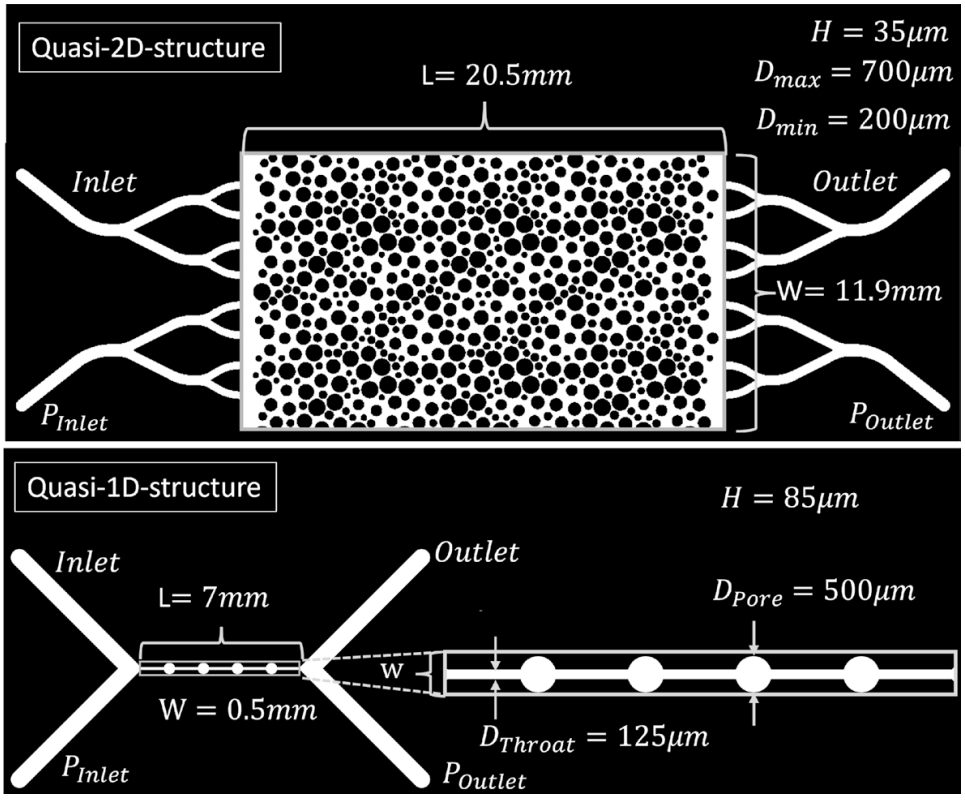

Fig. 1 Dimensions of the two types of porous media structures: Top: *Quasi-2D-structure* made out of glass. Bottom: *Quasi-1D-structure* made out of PDMS. White refers to pore space and black to solid. The porous domains, for which porosities and permeabilities are defined in this work, are framed in gray

through-plane to an extent of 85 µm. The porous domain in this case has the dimensions 7 $\times 0.5$ $\times 0.085$ mm.

The glass cells were purchased from Micronit©, Enschede, The Netherlands, and are made out of Borosilicate glass. Similar to the previously described PDMS-based cells, the glass cells also consist of an inlet and an outlet channel, including distribution channels and two additional channels that are connected to the pressure sensors. However, the pore structure is different. The solid matrix consists of pillars of various sizes, ranging from diameters between 200 and 700 µm. The pore space (white) inbetween is initially fully connected and its extension in the through-plane is 35 µm. The porous domain in this case has the dimensions 20.5 $\times$ 11.9 $\times 0.035$.

2.1.3 Injection Strategy

The microfluidic cells were fully saturated with deionized water prior to the microfluidic experiments. Solutions 1 and 2 were co-injected into the glass cells using syringe pumps from CETONI GmbH, Korbussen, Germany, at controlled flow rates; they mix in a T-junction right before they enter the cell through an inlet tube. The outlet tube was connected to a reservoir with a constant head, elevated 10 cm above the cell. The precipitation process was observed and visualized by optical microscopy (see 2.2), and the flow and pressure data were logged continuously. The setup was designed in a way that the pressure sensors were connected in parallel to the inlet and outlet channels to enable reliable measurements of pressure differences across the porous domain of interest, for details see (Weinhardt et al. 2021a). With that we are able to measure the pressure drop of the porous domain reliably and synchronized with the pore-space alteration observed through optical microscopy.

The detailed injection procedures varied slightly between the six experiments and are summarized in Table 1. They differ in terms of the total duration of the experiment, the type of pressure sensor that was used with different measurement ranges, the flow rates, and the residence times in the porous domain. The experiments with the simple pore structure (*Quasi-1D-1 - 3*) were conducted by applying constant flow rates of the two syringes with a total flow rate of 0.02 µL/s. The duration of experiment *Quasi-1D-2* was shorter in time compared to the others since the pressure limit of the pressure sensor was reached after 3.1 hours of injection (also see Weinhardt et al. [2021a)].

Table 1 Injection procedure: *Flow rate* corresponds to the total flow of both reactant solutions, *Residence time* refers to how long the reactive solutions sojourn in the porous domain, *Sensor* defines the range of the pressure sensor, *Duration* corresponds to the total duration of the experiment, Re and Pe are the Reynold's and Péclet numbers with regard to the porous domain, where the height of the cell was chosen as the characteristic length, and the diffusion coefficient of carbonate ions in water ($D = 8.04E - 10$ m^2/s) was used for determining the *Pe* (von Wolff et al. 2021)

Experiment	Flow rate [µL/s]	Res. time [s]	Sensor [mbar]	Duration [h]	Re [-]	Pe [-]
Quasi-1D-1	0.02	6	70	5.0	0.04	5
Quasi-1D-2	0.02	6	70	3.1	0.04	5
Quasi-1D-3	0.02	6	70	5.1	0.04	5
Quasi-2D-1	0.04, 0.02, 0.01	90–360	70	41.4	8*E*-4 – 3*E*-3	1–4
Quasi-2D-2	0.04, 0.02, 0.01	90–360	70	25.9	8*E*-4 – 3*E*-3	1–4
Quasi-2D-3	0.01, 0.04	360	1000	26.4	3*E*-3	4

For the experiments with the complex structure, the initially applied flow rate was 0.04 µL/s. For the experiments *Quasi-2D-1* and *Quasi-2D-2*, the flow rate was decreased to 50% once the limit of the pressure sensor was reached. This procedure was repeated twice before the cell was flushed with deionized water to stop the reaction. It has to be mentioned that experiment *Quasi-2D-1* required an intermediate restart and resaturation after approximately 26 hours due to leakage and clogging issues in the inlet zone of the cell. The relatively high flow rates during the resaturation process may have led to experimental artifacts, like the initiation of a preferential flow path and will be discussed in Sect. 3. For experiment *Quasi-2D-3*, a MPS2 pressure sensor with an increased range of 1000 mbar was used, and the applied flow rate was initially constant at 0.01 µL/s for two hours and then constant at 0.04 µL/s until the end of the experiment. For all experiments, we have creeping-flow conditions, i.e., Reynolds numbers < 1. The corresponding Péclet numbers (Pe) range between 1 and 5, indicating a slightly advection-dominated flow regime. The Damköhler number (Da) in our experiments is not straightforward to define, since two reactions are occurring in parallel: (1) the hydrolysis of urea and (2) the precipitation of calcium carbonate (see SI for the definitions of the dimensionless numbers). Even though the precipitation rate depends inter alia on the available surface, supersaturation of the bulk, and other factors, it is rather fast compared to the urea hydrolysis (Hommel et al. 2016). Therefore, the precipitation rate is often considered to be controlled by the rate of ureolysis (Landa-Marbán et al. 2021; Qin et al. 2016). According to Feder et al. (2021) and Hommel et al. (2020), the hydrolysis can be assumed to be a first-order kinetic reaction with respect to the concentration of urea. However, due to relatively short residence times in the porous domain and high enough initial concentration of urea, the hydrolysis rate can be assumed as constant throughout the domain, meaning that the influent and effluent concentrations were approximately equal (von Wolff et al. 2021; Jackson et al. 2021; Connolly et al. 2015).

2.2 Imaging

In this study, we used both optical microscopy and μXRCT scanning, in order to observe the precipitation processes in the microfluidic cells.

2.2.1 Optical Microscopy

During the experiment, we used transmitted light microscopy, which allowed us to observe the process time-resolved. A custom-made microscope has been used as described in Karadimitriou et al. (2012) that allows to visualize samples with a resolution of 0.5–20 µm/pixel. In this study, the resolution of the first data set with the *Quasi-1D-structure* was between 3.17 and 3.36 µm/pixel and between 8.93 and 9.31 µm/pixel for the second data set with the *Quasi-2D-structure*. The frame rates ranged between 1 and 0.1 fps, but not all of the recorded images were used for further processing. Details can be found in the description of the respective datasets (Weinhardt et al. 2021b, c).

2.2.2 μXRCT Scanning

In this study, we analyze the reconstructed and segmented μXRCT data set, obtained from one of the Quasi-1D-structure experiments (Vahid Dastjerdi et al. 2021). The microfluidic cell was scanned after the precipitation experiment using an open and modular XRCT device described

in Ruf and Steeb (2020). Therefore, the scan visualizes the precipitates at their final state, and, thus, not time-resolved. The resolution was 4.25 µm/pixel. Details on the segmentation can be found in Weinhardt et al. (2021a) and operating parameters in the description of the dataset Vahid Dastjerdi et al. (2021).

2.2.3 3D Reconstruction from 2D Images

As already outlined, images obtained from optical microscopy are time-resolved in this study. However, in order to derive the volume change, we need to reconstruct from 2D projections to 3D objects. As proposed in Kim et al. (2020) and elaborated in detail by Weinhardt et al. (2021a), a convenient way in microfluidic precipitation experiments is to assume certain shapes of individual crystals, like cylinders, semispheres, spheres, or spheroids, as shown in Fig. 2. The projection area of a crystal aggregate (A) is converted into an equivalent radius (r_{eq}), Eq. 4. Based on the r_{eq} and the height of the microfluidic cell (H), the volume of individual crystal aggregates can be quantified according to Eq. 5a–5c. Using the 3D dataset obtained from μXRCT imaging, we can identify the best-matching shape assumption in terms of volume estimation, derived from the projection area of each individual crystal.

However, this approach can only be applied, if we can distinguish individual crystal aggregates, as it is the case for the *Quasi-1D-structure*. In the case of the *Quasi-2D-structure*, recorded with less resolution and increased injection time, it has been observed that precipitates grow together and at some point cannot easily be distinguished or separated by image processing anymore. In that case, the 3D volume is estimated by assuming a frustum shape of the aggregates as illustrated in Figure 2. It is defined by the Euclidean distance of the center of a pixel, segmented as solid, to the center of the closest pixel, segmented as void space, (dist(i)) and the angle (α) that determines the slope of the frustum (Eq. 5d). In contrast to the previous approaches, the angle (α) is adjustable and must be defined before processing.

$$r_{eq} = \sqrt{\frac{A}{\pi}} \tag{4}$$

$$V_{cylindrical} = \pi r_{eq}^2 H \tag{5a}$$

$$V_{semisphere} = \begin{cases} \frac{2}{3}\pi r_{eq}^3 & r_{eq} < H \\ \frac{\pi}{3}(3Hr_{eq}^2 - H^3) & r_{eq} > H \end{cases} \tag{5b}$$

$$V_{spheroid} = \begin{cases} \frac{4}{3}\pi r_{eq}^3 & 2r_{eq} < H \\ \frac{2}{3}\pi r_{eq}^2 H & 2r_{eq} > H \end{cases} \tag{5c}$$

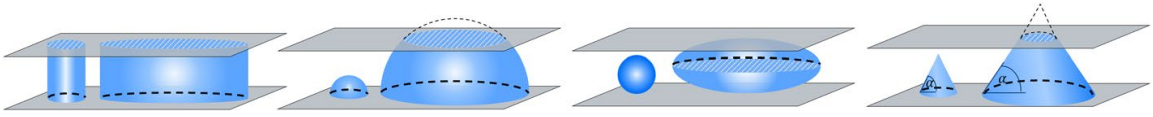

Fig. 2 Hypothetical shape of crystal aggregates from left to rigth: cylinder, semisphere, spheroid, frustum

$$V_{\text{frustum}} = \sum_{i=1}^{n} \min\big(\text{dist}(i) \cdot \tan(\alpha), H\big) \tag{5d}$$

3 Results and Discussion

3.1 Validation of the Reconstruction Method

To begin with, we consider only the data gathered from μXRCT scans (Vahid Dastjerdi et al. 2021). Therefore, the projection of all planes from the μXRCT images were used as a hypothetical 2D image, since this would correspond to what could be observed by optical microscopy. Based on the projections of the precipitates, their volumes were calculated assuming four different shapes, respectively. In Fig. 3 on the right, the procedure is shown for one exemplary crystal in the porous domain. The top part of this figure gives the 2D projection of the μXRCT images. As a reference, the real 3D structure, as obtained from the μXRCT scan, is shown on the right and below that are the other shape assumptions illustrated, i.e., semisphere, spheroid and frustum, the latter one with the angle $\alpha = 71°$.

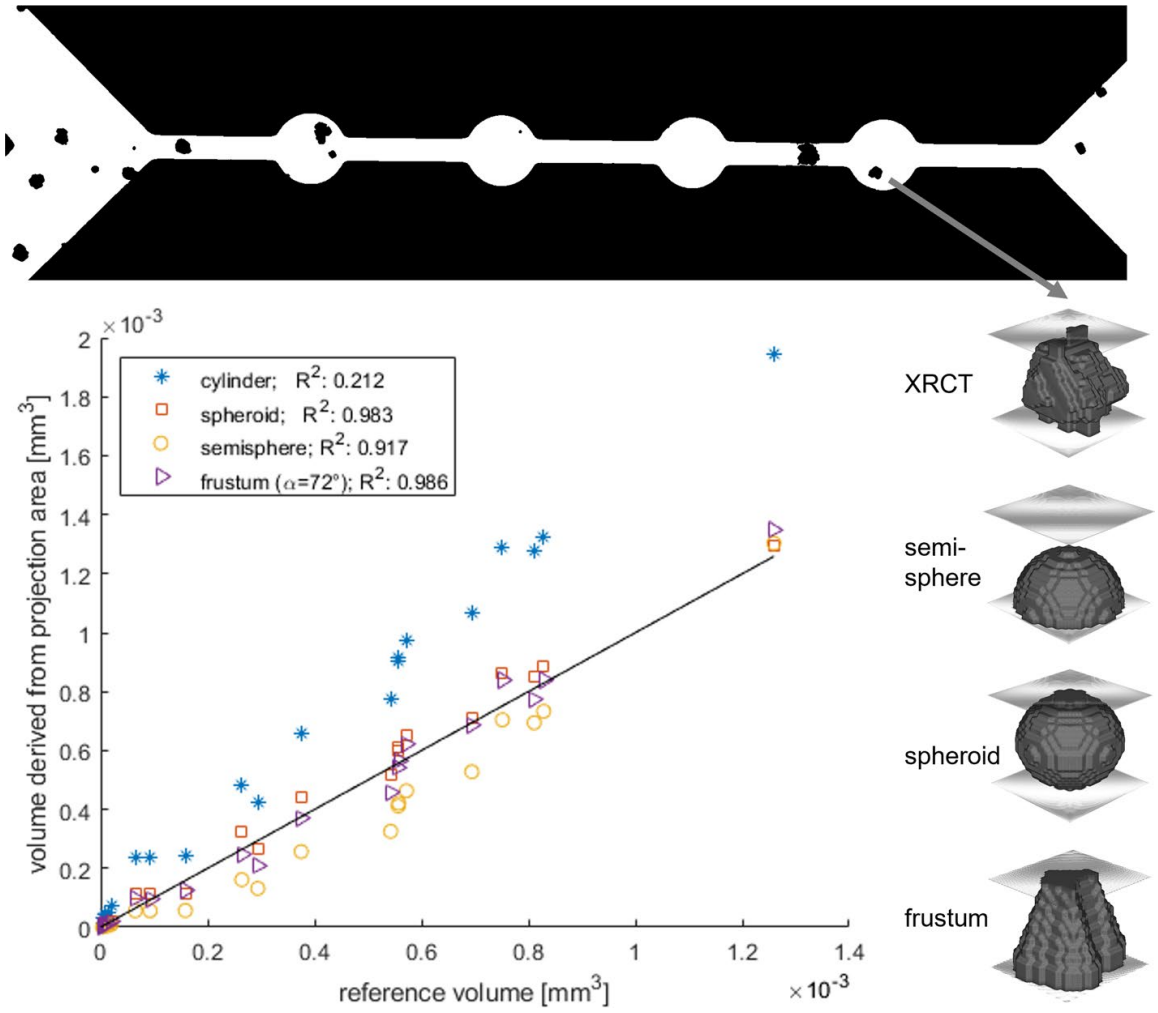

Fig. 3 Volume derived from projection area of the XRCT-scan for different shape assumptions, including their coefficient of determination (R^2) with respect to the reference volume. Top: 2D projection of the domain. Right: Reconstructed shapes for one exemplary precipitate

On the left of that figure, the volumes derived from the projected areas are plotted against the actual volume derived from the 3D data set, where the latter is the reference volume. Therefore, the bisector, shown as black solid line, corresponds to the perfect match of the volume derived from the projection with the reference volume. Each data point represents one crystal in the entire scanned domain. The assumption of a cylindrical shape clearly overestimates the volume of the crystal aggregates, which can be expected since the crystals do not fill the entire height of the micro-fluidic cell everywhere. The approach of the spheroidal shape is in quite good agreement with the reference volume over the entire range of sizes, while the semispherical approach, proposed by Kim et al. (2020) mainly underestimates the volume of the crystals. In the case of the frustum-shape assumption, we have a parameter α, determining the slope, as an adjustable (tunable) parameter. In this case, the best fitting value is $\alpha = 72°$. Based on the coefficient of determination (R^2), it can be concluded that the spheroidal shape as well as the frustum shape are best choices to determine the volume from a projected area. Note that this is a pragmatic and empirical way with the aim to estimate the overall volume change of precipitates from 2D projections in a more sophisticated way.

3.2 Crystal Growth and Transformation of Calcium Carbonate Polymorphs

We observe in our studies that different *types* of precipitates occur in the microfluidic cells. They differ in terms of gray-scale value when they are recorded through optical microscopy. In Fig. 4, a time series from 4 to 24 h is shown for the experiment *Quasi-2D-2*. There are precipitates with darker appearance that mainly stay at their original position and grow over time, as well as lighter ones, irregularly shaped, which are more likely to be transported with the flow. Since different polymorphs of calcium carbonate can occur, and indeed their occurrence in the context of MICP has been reported in recent microfluidic

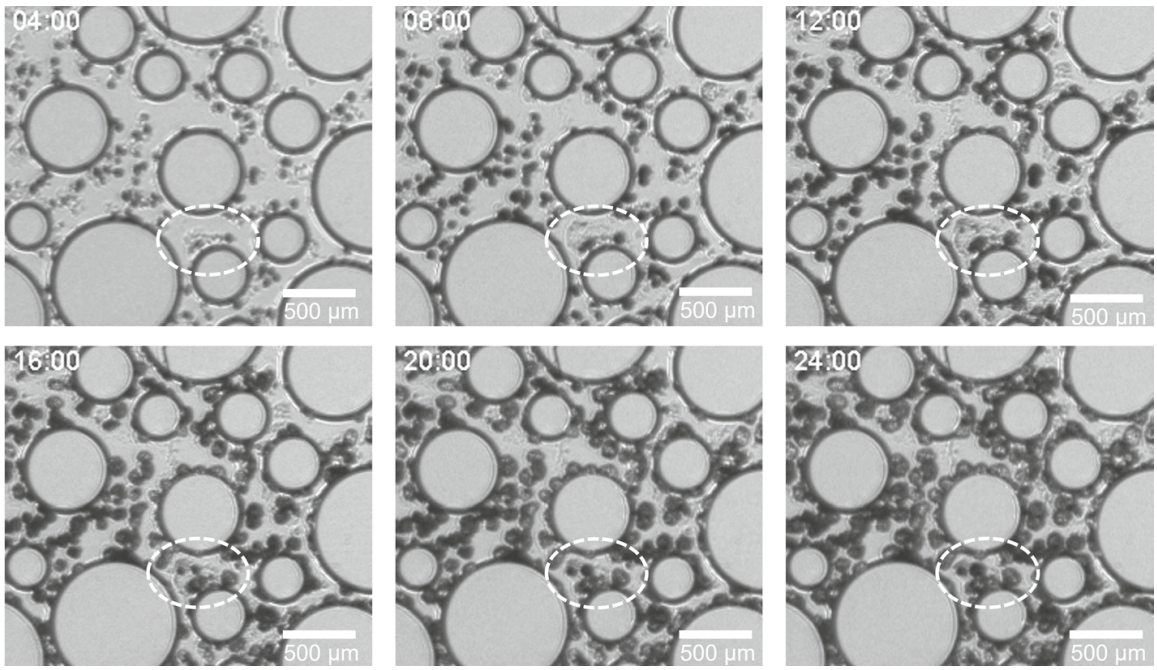

Fig. 4 Time series of a small section of Experiment *Quasi-2D-2* from 4 to 24 h: transformation of lighter appearing precipitates (hypothesized to be ACC) to darker appearing precipitates (hypothesized to be vaterite or calcite). A corresponding video is provided in the SI (*V_Transformation.mp4*)

investigations (Wang et al. 2021; Zambare et al. 2020), it seems likely that these are different polymorphs. During the initial stage of the precipitation process, mainly lighter irregularly shaped $CaCO_3$ precipitates (hypothesized to be ACC) formed, which later on transformed into darker crystals (hypothesized to be vaterite and calcite). In Fig. 4, such a transformation can clearly be seen in the area marked with a dashed circle: from the time stamps at 04:00 h until 12:00 h two darker precipitates are surrounded by irregularly shaped lighter precipitates. At time stamp 16:00 h, two additional darker precipitates form within the aggregation of irregularly shaped lighter precipitates. These darker precipitates grow within time, while the surrounding lighter precipitates seem to disappear in favor of the darker ones.

In fact, we cannot distinguish with certainty between these different polymorphs of $CaCO_3$ with our setup; however, our observations indicate that formation of ACC at early stages of the precipitation process, followed later by transformation into vaterite or calcite, is very plausible. Even though we use EICP with a continuous injection of the reactive solutions, these findings are in agreement with the ones reported in (Wang et al. 2021; Zambare et al. 2020) who used MICP and a staged injection or a batch system, respectively. This occurrence of different polymorphs and their transformation have substantial effects on the porosity–permeability relation, which will be further discussed in Sects. 3.3.2 and 3.3.3 .

3.3 Porosity–Permeability Relation

In this subsection, we present our experimental results with the focus on the porosity–permeability relationship. We identified different key mechanisms that influence the shape of the porosity–permeability relationships. At first, the initial geometry of the porous domain, in our case the *Quasi-1D-structure* compared to the *Quasi-2D-structure*, is discussed. Furthermore, time dependence and two kinds of injection strategies, namely constant flow vs. step-wise decreased flow imposed at the boundary, are evaluated. Subsequently, the role of preferential flow paths during precipitation are evaluated and discussed. In order to evaluate porosity changes from 2D projections, the segmented images of all experiments were processed further, based on the approach described in Sect. 2.2. In this case, we used the assumption of a frustum shape for the precipitates using a slope with an angle of $\alpha = 72°$, since this has been shown in Sect. 3.1 to fit best in terms of volume estimation. Since the permeability can be calculated from the pressure data, we can relate the obtained average quantities, porosity and permeability, to each other. Both the segmented images and the log data, including flow rates and pressure measurements, can be found in Weinhardt et al. (2021b, 2022).

3.3.1 Effect of the Pore Structure (*Quasi-1D vs Quasi-2D*)

In Fig. 5, the normalized permeability is plotted over the change of the porosity for all six experiments in a log-log graph. Here, it needs to be mentioned that the experiment *Quasi-2D-1* had to be restarted and resaturated, and, therefore, the data shown in this figure start when precipitation has already been present in the domain (see Sect. 2.1). It can be clearly observed that the experiments using the *Quasi-1D-structure* have a very dominant decrease in the normalized permeability within 10% of porosity reduction. Comparing it to a simple power-law relationship (Eq. 3), the exponents, η, are roughly in the range of 30–100. This wide range of values for the exponents can be explained by the rather simple

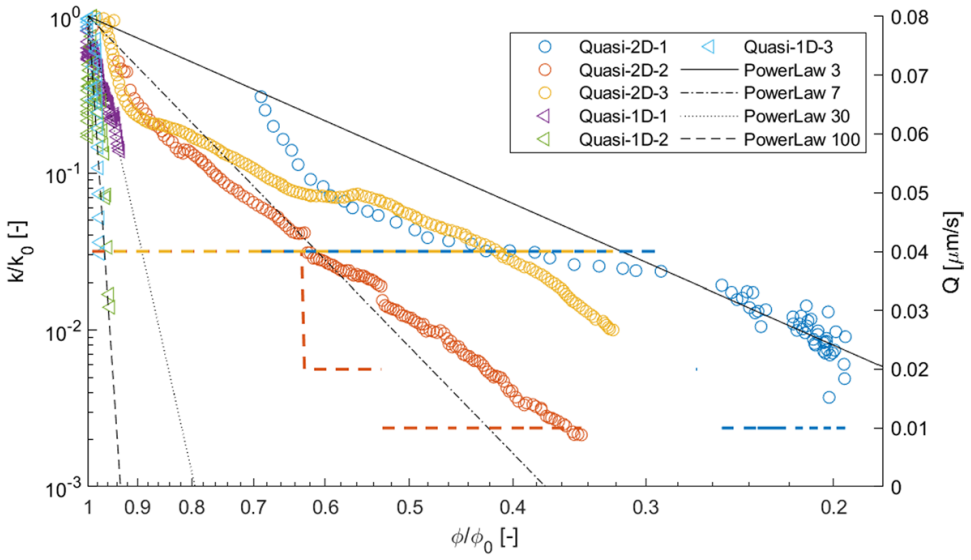

Fig. 5 Left: Log-log-plot of the porosity–permeability relationship for the six experiments, compared to power-law relationships with different exponents. The horizontal dashed lines indicate the applied flow rates of the *Quasi-2D-experiments* referring to the second y-axis on the right

and one-dimensional structure of the porous domain. If one single location in the domain is clogged or close to clogging, the permeability decreases, even though the overall change of pore space is not significant. We can conclude from this that at least for this specific geometry, the location of the precipitates dominates the decrease in permeability rather than the porosity as a averaged quantity. It has to be noted that the pore morphology chosen for the microfluidic cell only consists of four pore cavities connected with pore throats, it has to be noted that this cannot considered as being representative for a porous medium.

In contrast, the experiments using the *Quasi-2D-structure* show a different behavior. The geometry itself can generally be considered as closer to representing a 2D porous medium. Compared to the *Quasi-1D-structure*, there is now another degree of freedom in the lateral direction, so fluids can flow even though some individual pore throats might be locally clogged. This leads to a smoother porosity–permeability relationship. Comparing them again to simple power-law relationships, the exponents range between 3 and 7. This is in agreement with what has been reported in the literature. To describe precipitation processes, widely used exponents are in a range between 1 and 9 (Hommel et al. 2018).

We can conclude that for quasi-1D systems, like the *Quasi-1D-structure*, the location of the precipitates is much more important than the overall porosity reduction. In contrast, in more realistic porous media, like the *Quasi-2D-structures*, this local effect is averaged out to some extent, which leads to smoother porosity–permeability relationships. However, among these three *Quasi-2D-experiments*, differences exist, and phenomena and mechanisms leading to this will be discussed below.

3.3.2 Time Dependence and Injection Strategies

We discuss how the occurrence of amorphous calcium carbonate (ACC), its further transformation to vaterite or calcite, that has been described in Sect. 3.2, as well as the applied injection strategy influence the porosity–permeability relationship. We consider the occurrence of ACC and its transformation to other polymorphs of calcium carbonate as very plausible. This hypothesis is therefore used below for interpreting particular hydraulic

responses. We note, however, that the currently available data do not allow for an unequivocal identification of those irregularly shaped precipitates as ACC. This would require other sophisticated experimental techniques, such as Raman microspectroscopy as in the work of Zambare et al. (2020). In Fig. 6, the two experiments *Quasi-2D-2* and *Quasi-2D-3* are directly compared to each other. In the early stages, approximately during the first five

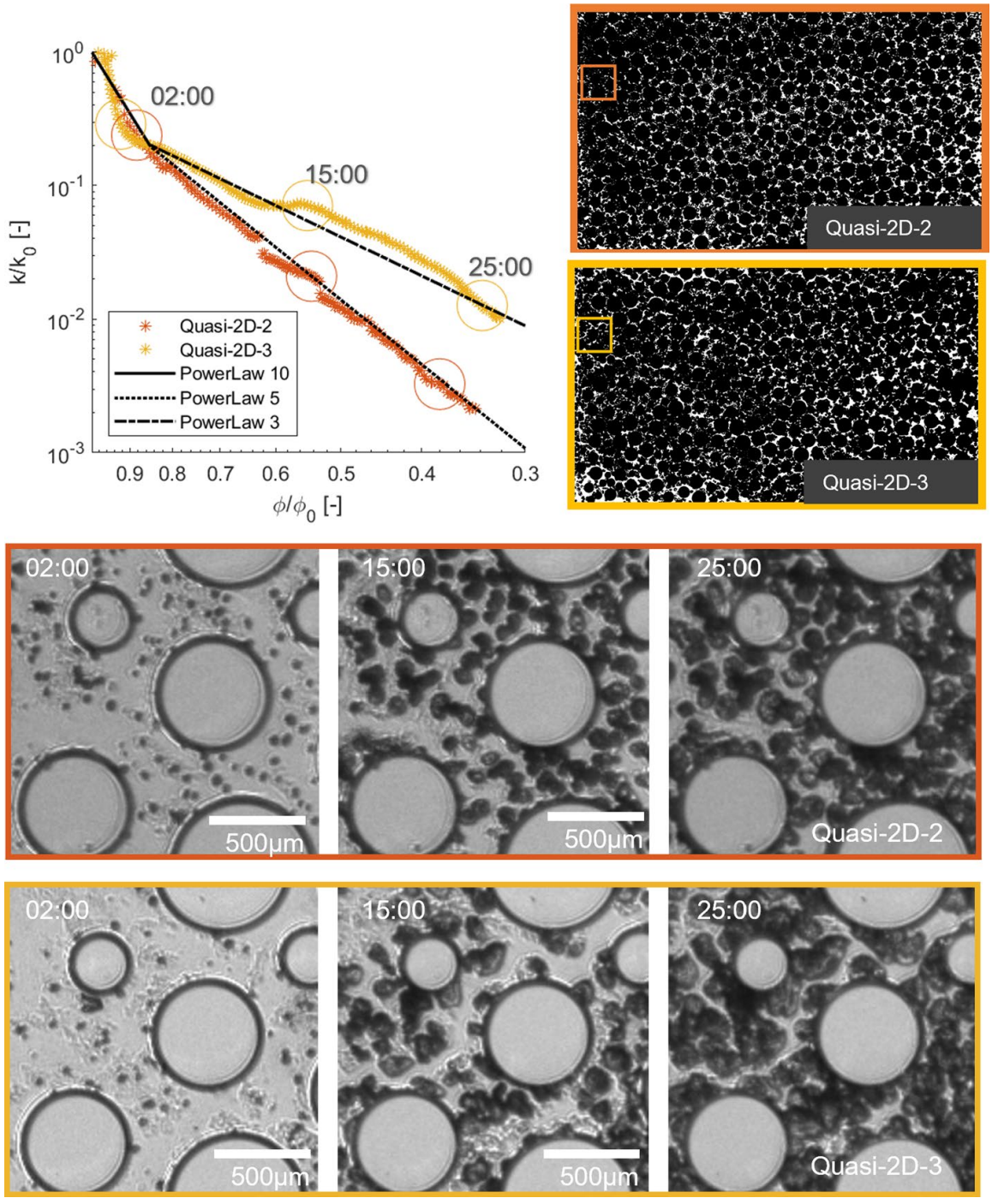

Fig. 6 Temporal evolution of the porosity–permeability relationship for the Experiments *Quasi-2D-2* and *Quasi-2D-3*. Top left: Experimental data points including fitted power law relationships with the exponents 10 (early stage), as well as 5 and 3 for the later stages, respectively. Top right: Segmented images of the whole domain at time stamp 25 h. Bottom: series of unprocessed microscopy images after 02:00, 15:00 and 25:00 h. The corresponding data points are highlighted with circles in the graph above. See Video *V_TimeDependentPoroPerm.mp4* in the SI for the complete temporal evolution

hours of both experiments, the decrease in the permeability is rather fast compared to the porosity reduction. This results in a rather high exponent ($\eta = 10$) of the fitted power-law relationship. This early decrease in permeability has also been described in previous MICP experiments (Phillips et al. 2013b), while numerical modeling led to an underestimation of the initial reduction in permeability (Hommel et al. 2013). We hypothesize that the reason for this early disproportional decrease in the permeability is the relatively high ratio of ACC present in the domain, compared to the crystalline polymorphs vaterite or calcite. The optical microscopy images in Fig. 6 at the time stamp 02:00 h hours show this amorphous aggregation of precipitates surrounding the crystalline polymorphs. Since ACC is hydrated in the early stages of a precipitation process, it has a relatively low density (Rodriguez-Navarro et al. 2015). Moreover, due to the small size of the ACC precipitates in the early stages, the surface area, where shear forces act on, is higher compared to later stages. Therefore, it can be transported with the flow and temporally clog pathways, especially when the overall pressure drop is still low, as it is the case in the early stages of the experiment. The pressure drop can be interpreted as a proxy for the average flow velocity, which again is a proxy for the shear stresses acting on the precipitates. In addition to that in the early stages, precipitates might not be as well-attached to the surface yet, and there is more space available where they can be transported to. While precipitation continues and time passes, the amount (~ volume) of ACC reduces due to its possible transformation to vaterite or calcite and the available void space reduces. As a consequence, temporally clogged pathways become passable again, and the fitted power-law relationships have smaller exponents in the later stage. While the early stage for both experiments is quite similar, the curves diverge toward the end. This can be explained by the different injection strategies of the experiments, namely a step-wise decreased flow rate in Experiment *Quasi-2D-2* and a constant flow boundary in the Experiment *Quasi-2D-3*. The curve for Experiment *Quasi-2D-2* shows a quite smooth porosity–permeability relationship with an exponent of 5. In contrast, the data set of experiment *Quasi-2D-3* shows a plateau between 10 and 15 h, which corresponds to the normalized porosities between 0.65 and 0.55. Both experiments globally show a rather homogeneous distribution of the precipitates, which indicates reaction-limited conditions as described in Sect. 2.1. However, on the sub-pore scale, we can observe that flow paths develop locally through detachment, transport, and filtering of ACC. This phenomenon cannot be explained by state-of-the-art theoretical descriptions of precipitation processes in porous media, which so far only differentiate between reaction- and transport-limited regimes; the phenomenon is also mostly neglected in theoretical computational studies like (Niu and Zhang 2019; Jung and Meile 2021; von Wolff et al. 2021). While in Experiment *Quasi-2D-3*, with a constant flow rate, these flow paths stay open, in Experiment *Quasi-2D-2* with a reduced flow rate, the growth of the existing precipitates dominates over the transport of loose precipitates with the consequence that flow paths can close. This temporal evolution is also visualized in the Video *V_TimeDependent-PoroPerm.mp4* in the SI.

It seems that the exact positions of precipitate formation and flow path development are difficult—if not impossible—to reproduce. This depends inter alia on initial nucleation sites present in the domain (Weinhardt et al. 2021a) and can therefore be considered a stochastic process. Still, it is plausible to conclude that the polymorphism of calcium carbonate has a substantial impact and promotes these detachment and reattachment scenarios of loose precipitates (mostly ACC), thus leading to the evolution of preferential flow paths. Due to the presence of preferential flow paths, the porosity–permeability curve is shifted toward lower porosities at almost constant permeabilities—meaning it temporally flattens the curve and reduces the exponent of the overall fitted power-law relationship. This effect can

be reduced by step-wise decreasing the injection rate and, therefore, reducing the exposure of calcium carbonate precipitates to shear stress.

3.3.3 Dominant Preferential Flow Path

Moreover, in the case of the Experiment *Quasi-2D-1*, we see an even more dominant shift of the porosity–permeability relationship in Fig. 5. A clear preferential flow path can be identified in the top of the domain and the precipitation pattern throughout the domain is quite heterogeneous (see Fig. 7a). Here, it needs to be mentioned that during this experiment the

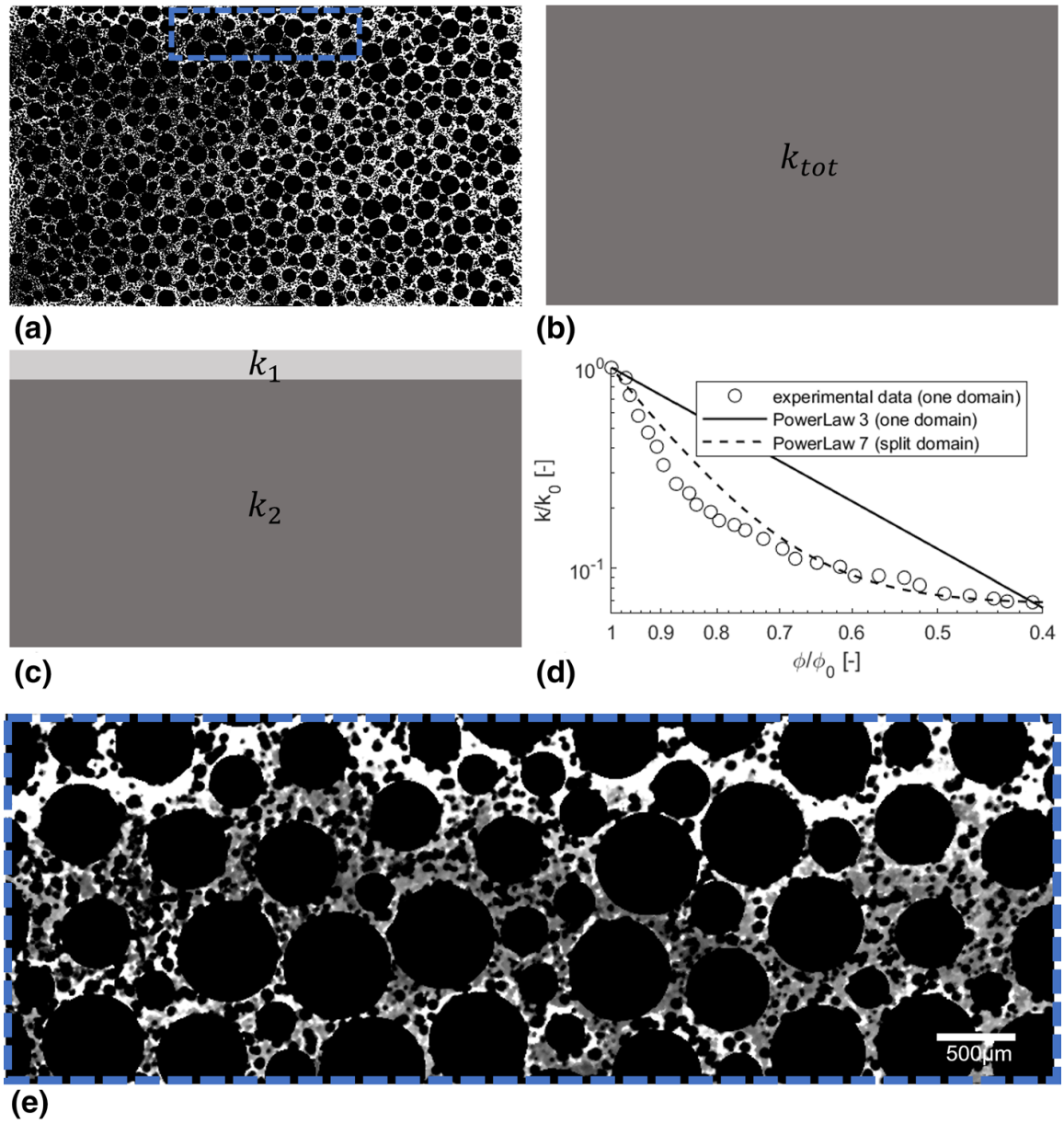

Fig. 7 Subdomain approach to account for preferential flow paths. Experimental data from the *Quasi-2D-1* experiment during a 5-hour interval and a constant flow rate of 0.04 μL/s. **a** segmented image at the end of the interval. **b** Representation as one REV. **c** Representation as two subdomains with individual permeabilities, k_1 and k_2. The cross-sectional proportions are 1/15 for domain 1 and 14/15 for domain 2. **d** Porosity–permeability relationship in a log-log-plot. The values are normalized to the initial state of the interval. Comparison of the two approaches to the experimental dataset. **e** Section of the domain, white is void space, black is solid and gray indicates the increment in precipitates during the five hour interval

microfluidic cell had to be resaturated by applying relatively high flow rates using deionized water (see Sect. 2.1). This has probably caused a breakthrough at the top of the domain by flushing out some precipitates and has led to an *artificially created* dominant preferential flow path (see SI for further explanations). Note that we now discuss the results of the *Quasi-2D-1* experiment during the period after its restart and before reducing the flow rate. This means that precipitates already exist inside the cell, and that during this 5-hour interval, a constant flow rate of 0.04 µL/s was applied. Thus, after continuing the experiment at a constant flow rate, this flow path stays open, while increased precipitation is noticed in its surrounding. This temporal evolution is visualized in Fig. 7e), where a small section of the domain is given. For that, time-resolved binarized images (white is void, black is solid) are summed up over a period of 5 h. The resulting gray-scale values represent the time period during which a precipitate has been at the corresponding location (the darker, the longer). The changes of the precipitates within the flow path (indicated by a gray frame around them) are relatively small compared to the gray areas in the surrounding of the flow path. In addition, the video, *V_DominantPreferentialFlowPath.mp4*, given in the SI, shows the transport of small precipitates into the vicinity of the flow path. From this it can be concluded that the pore-space alteration due to transport of loose precipitates into the pore throats next to the flow path might have been more important than the growth of individual crystals in the preferential flow path. During a constant flow rate, the small crystals (hypothesized to be ACC) are transported along the flow path and at bifurcations also into smaller pore throats. This consequently leads toward a separation of the preferential flow path from the rest of the domain, which again locally increases kinetic energy in the flow path concomitant with detachment and transport of smaller crystals. Therefore, at constant-flow boundaries, this channeling is a self-enhancing process, which was similarly observed during MICP treatment of fractures (Mountassir et al. 2014). In addition to that we showed that this strongly affects the developing porosity–permeability relationship.

Due to this dominant preferential flow path in the top of the domain, the precipitation pattern is quite heterogeneous. Thus, the corresponding apparent porosity–permeability relationship deviates strongly from the classical power-law relationship. This can be explained by the fact that the domain cannot be described as one single representative elementary volume (REV) anymore, which may be difficult to adapt in REV-scale modeling efforts and highlights the relevance of pore-scale modeling. In order to explain the behavior of the porosity–permeability relation, we compare two assumptions: the first one is that we assume the domain to be **one single** REV and define one permeability: k_{tot} (Fig. 7b). The other assumption would be to split the domain into two subdomains, each with an individual permeability, k_1 and k_2 (Fig. 7c). In that case, one REV represents the upper part including the preferential flow path and the second one represents the rest of the domain. Since we observed that the flow path stayed open, we assign a constant permeability to Domain 1. The permeability of Domain 2 is calculated by a power-law relationship with the exponent 7. Since the flow is parallel to the interface of the subdomains, we can use the arithmetic mean to calculate the averaged permeability of both subdomains. In Fig. 7d, the two approaches are compared to the measured experimental data. We can see that with the assumption of two subdomains, we can reproduce the shape of the apparent porosity–permeability curve of the experimental data.

4 Conclusions

In this study, enzymatically induced calcium carbonate precipitation (EICP) was investigated in microfluidic cells during a continuous injection of the reaction solutions. The design of the microfluidic cells allowed for reliable continuous pressure and flow rate monitoring during the precipitation. From these pressure and flow rate measurements, the permeability reduction of the porous domain was obtained. Since the cells are transparent, we were able to use optical microscopy to observe the growth of the crystal aggregates synchronized with the pressure measurements. Analyzing a μXRCT-scan, we found that assumptions of spheroidal or frustum shape approximate the volume of precipitates the best when estimating the change in pore volume based on the 2D-projected images from optical microscopy. Thus, we were able to accurately relate porosities and permeabilities and to identify the following key mechanisms during EICP treatment:

- In the *Quasi-1D-structure*, the changes in permeability are dominated by the location of the precipitates rather than by the overall porosity reduction, leading to very high exponents (30–100, Eq. 3) which are hard to determine when trying to match permeability/porosity data with a simple power-law. In contrast, for the *Quasi-2D-structures*, which are, of course, closer to reality, the effect of single pore-throat clogging is less important, which leads to much smoother porosity–permeability relationships with smaller exponents (3–7, Eq. 3).
- We observed that particularly in the early stages of the precipitation process mainly small, irregularly shaped precipitates (hypothesized to be ACC) formed, which, due to their small size and density, would be more likely to be transported with the flow, and may have temporarily clogged pathways. Possible additional factors are that in the early stages, these precipitates are not as well-attached to the surface yet, and that there is more space available into which they can be transported, compared to later stages when most of the void space has been occupied. This consequently results in a high permeability reduction at early times and a power-law exponent of around 10 in our case. In later stages, ACC appears to transform to vaterite or calcite and consequently reduces the slope of the porosity–permeability data with power-law exponents between 3 and 5 (Eq. 3).
- With constant-flow boundaries, flow paths evolve and remain open due to shearing off and redepositing of the small precipitates. This leads to a shift in the porosity–permeability relationship with the consequence of reduced exponents of the corresponding fitted power-law relationship. Under step-wise decreased flow boundary conditions, which can be interpreted as moving toward an approximation of constant-head conditions, these effects are not seen, since the kinetic energy of the fluid and, consequently, the shear forces, to which the precipitates are exposed, remain approximately constant.
- Preferential flow paths form and appear to persist under continuous flow conditions. As a consequence, the resulting heterogeneous precipitation pattern, identified on the pore-scale, leads to difficulties for the macro-scale definition of the correct REV with its upscaled parameter permeability. In consequence, this would justify the use of dual-porosity models for approximating permeability on the macroscale. However, this only holds for constant-flow conditions, where the flow enforces preferential flow paths as soon as the matrix is sufficiently impermeable.

This study raises further research questions. For example, how EICP treatment could be optimized for fractured porous media, where obviously preferential flow paths already exist. Fluorescence microscopy, as well as micro-scale particle image velocimetry (μPIV), would enhance our, for now qualitative, observations by measuring the velocities in the flow paths and by quantifying the portion of autofluorescent calcite in the domain. Also Raman microspectroscopy, as performed by Zambare et al. (2020), would be necessary to be certain about the occurrence and transformation of ACC to more stable calcium carbonate polymorphs. Furthermore, experiments with varying inlet concentrations would be expedient for field-scale applications where locally concentrations vary. Moreover, it needs to be understood in what way these findings can be extrapolated to more realistic, fully three-dimensional porous media. In that case, flow has an additional degree of freedom which potentially affects the evolution and persistence of preferential flow paths and their length scales, while different surface properties might also influence the precipitation process. Even though we are convinced that constant flow boundary conditions will also lead to the evolution of preferential flow paths, the question how this will affect the porosity–permeability relationship still remains. Therefore, further investigations using column experiments are needed which would require time-resolved tomographic imaging techniques, for example nuclear magnetic resonance or μXRCT measurements as used in (Bray et al. 2017; Fridjonsson et al. 2011).

Electronic supplementary material The online version of this article (https://doi.org/10.1007/s11242-022-01782-8) contains supplementary material, which is available to authorized users.

Funding Open Access funding enabled and organized by Projekt DEAL. Funded by the Deutsche Forschungsgemeinschaft (DFG, German Research Foundation) - Project Number 327154368 (SFB 1313) and DFG Project Number 380443677 (for Johannes Hommel). Partial financial support for Robin Gerlach for this work was provided by the Office of Research Economic Development and Graduate Education and the Norm Asbjornson College of Engineering at Montana State University.

Data Availability The experimental dataset is available in the data repository of the University of Stuttgart (DaRUS). It contains images of optical microscopy together with the log data, including flow rates and pressure measurements and can be accessed via the link: https://doi.org/10.18419/darus-1799 (Weinhardt et al. 2022).

Declarations

Conflict of interest The authors declare that they have no conflict of interest.

References

Akyel, A., Coburn, M., Phillips, A., Gerlach, R.: Key applications of biomineralization. In: Mineral Formation by Microorganisms - Concepts and Applications, Springer International Publishing: 347–387, Cham (2022). https://doi.org/10.1007/978-3-030-80807-5_10

Andrew, R.M.: Global CO_2 emissions from cement production, 1928–2018. Earth Sys. Sci. Data **11**(4), 1675–1710 (2019). https://doi.org/10.5194/essd-11-1675-2019

Arab, M.G., Omar, M., Almajed, A., Elbaz, Y., Ahmed, A.H.: Hybrid technique to produce bio-bricks using enzyme-induced carbonate precipitation (EICP) and sodium alginate biopolymer. Constr. Build. Mater. (2021). https://doi.org/10.1016/j.conbuildmat.2021.122846

Benini, S., Rypniewski, W.R., Wilson, K.S., Miletti, S., Ciurli, S., Mangani, S.: A new proposal for urease mechanism based on the crystal structures of the native and inhibited enzyme from Bacillus pasteurii: Why urea hydrolysis costs two nickels. Structure **7**(2), 205–216 (1999). https://doi.org/10.1016/S0969-2126(99)80026-4

Bray, J.M., Lauchnor, E.G., Redden, G.D., Gerlach, R., Fujita, Y., Codd, S.L., Seymour, J.D.: Impact of mineral precipitation on flow and mixing in porous media determined by microcomputed tomography and MRI. Environ. Sci. Technol. **51**(3), 1562–1569 (2017). https://doi.org/10.1021/acs.est.6b02999

Cöelfen, H., Antonietti, M.: Mesocrystals and Nonclassical Crystallization. Wiley, New York (2008)

Connolly, J.M., Jackson, B., Rothman, A.P., Klapper, I., Gerlach, R.: Estimation of a biofilm-specific reaction rate: Kinetics of bacterial urea hydrolysis in a biofilm. npj Biofilms Microbiomes **1**, 15014 (2015). https://doi.org/10.1038/npjbiofilms.2015.14

Cunningham, A.B., Characklis, W.G., Abedeen, F., Crawford, D.: Influence of biofilm accumulation on porous media hydrodynamics. Environ. Sci. Technol. **25**(7), 1305–1311 (1991). https://doi.org/10.1021/es00019a013

Cunningham, A.B., Class, H., Ebigbo, A., Gerlach, R., Phillips, A.J., Hommel, J.: Field-scale modeling of microbially induced calcite precipitation. Comput. Geosci. **23**(2), 399–414 (2019). https://doi.org/10.1007/s10596-018-9797-6

Dejong, J.T., Soga, K., Kavazanjian, E., Burns, S., Van Paassen, L.A., Al Qabany, A., Aydilek, A., Bang, S.S., Burbank, M., Caslake, L.F., Chen, C.Y., Cheng, X., Chu, J., Ciurli, S., Esnault-Filet, A., Fauriel, S., Hamdan, N., Hata, T., Inagaki, Y., Jefferis, S., Kuo, M., Laloui, L., Larrahondo, J., Manning, D.A., Martinez, B., Montoya, B.M., Nelson, D.C., Palomino, A., Renforth, P., Santamarina, J.C., Seagren, E.A., Tanyu, B., Tsesarsky, M., Weaver, T.: Biogeochemical processes and geotechnical applications: Progress, opportunities and challenges. Geotech. **63**(4), 143–157 (2013). https://doi.org/10.1680/bcmpge.60531.014

Ebigbo, A., Phillips, A., Gerlach, R., Helmig, R., Cunningham, A.B., Class, H., Spangler, L.H.: Darcy-scale modeling of microbially induced carbonate mineral precipitation in sand columns. Water Resour. Res. **48**, W07519 (2012). https://doi.org/10.1029/2011WR011714

El-Sheikh, S.M., El-Sherbiny, S., Barhoum, A., Deng, Y.: Effects of cationic surfactant during the precipitation of calcium carbonate nano-particles on their size, morphology, and other characteristics. Colloids Surf. A Physicochem. Eng. Asp. **422**, 44–49 (2013). https://doi.org/10.1016/j.colsurfa.2013.01.020

Feder, M.J., Akyel, A., Morasko, V.J., Gerlach, R., Phillips, A.J.: Temperature-dependent inactivation and catalysis rates of plant-based ureases for engineered biomineralization. Eng. Rep. (2021). https://doi.org/10.1002/eng2.12299

Fridjonsson, E.O., Seymour, J.D., Schultz, L.N., Gerlach, R., Cunningham, A.B., Codd, S.L.: NMR measurement of hydrodynamic dispersion in porous media subject to biofilm mediated precipitation reactions. J. Contam. Hydrol. **120–121**, 79–88 (2011). https://doi.org/10.1016/j.jconhyd.2010.07.009

Hamdan, N., Kavazanjian, E.: Enzyme-induced carbonate mineral precipitation for fugitive dust control. Geotechnique **66**(7), 546–555 (2016). https://doi.org/10.1680/jgeot.15.P.168

Hassannayebi, N., Jammernegg, B., Schritter, J., Arnold, P., Enzmann, F., Kersten, M., Loibner, A.P., Fernø, M., Ott, H.: Relationship between microbial growth and hydraulic properties at the sub-pore scale. Transp. Porous Media **139**(3), 579–593 (2021). https://doi.org/10.1007/s11242-021-01680-5

Hommel, J., Cunningham, A.B., Helmig, R., Ebigbo, A., Class, H.: Numerical investigation of microbially induced calcite precipitation as a leakage mitigation technology. Energy Procedia **40**, 392–397 (2013). https://doi.org/10.1016/j.egypro.2013.08.045

Hommel, J., Lauchnor, E., Gerlach, R., Cunningham, A.B., Ebigbo, A., Helmig, R., Class, H.: Investigating the influence of the initial biomass distribution and injection strategies on biofilm-mediated calcite precipitation in porous media. Transp. Porous Media **114**(2), 557–579 (2016). https://doi.org/10.1007/s11242-015-0617-3

Hommel, J., Coltman, E., Class, H.: Porosity-permeability relations for evolving pore space: A review with a focus on (bio-)geochemically altered porous media. Transp. Porous Media **124**(2), 589–629 (2018). https://doi.org/10.1007/s11242-018-1086-2

Hommel, J., Akyel, A., Frieling, Z., Phillips, A.J., Gerlach, R., Cunningham, A.B., Class, H.: A numerical model for enzymatically induced calcium carbonate precipitation. Appl. Sci. **10**(13), 4538 (2020). https://doi.org/10.3390/app10134538

Jackson, B.D., Connolly, J.M., Gerlach, R., Klapper, I., Parker, A.E.: Bayesian estimation and uncertainty quantification in models of urea hydrolysis by E. coli biofilms. Inverse Prob. Sci. Eng. **29**(11), 1629–1652 (2011). https://doi.org/10.1080/17415977.2021.1887172

Jung, H., Meile, C.: Pore-scale numerical investigation of evolving porosity and permeability driven by biofilm growth. Transp. Porous Media **139**(2), 203–221 (2021). https://doi.org/10.1007/s11242-021-01654-7

Karadimitriou, N.K., Joekar-Niasar, V., Hassanizadeh, S.M., Kleingeld, P.J., Pyrak-Nolte, L.J.: A novel deep reactive ion etched (DRIE) glass micro-model for two-phase flow experiments. Lab Chip **12**(18), 3413–3418 (2012). https://doi.org/10.1039/c2lc40530j

Karadimitriou, N.K., Musterd, M., Kleingeld, P.J., Kreutzer, M.T., Hassanizadeh, S.M., Joekar-Niasar, V.: On the fabrication of PDMS micromodels by rapid prototyping, and their use in two-phase flow studies. Water Resour. Res. **49**(4), 2056–2067 (2013). https://doi.org/10.1002/wrcr.20196

Kim, D.H., Mahabadi, N., Jang, J., van Paassen, L.A.: Assessing the kinetics and pore-scale characteristics of biological calcium carbonate precipitation in porous media using a microfluidic chip experiment. Water Resour. Res. (2020). https://doi.org/10.1029/2019WR025420

Kirkland, C.M., Akyel, A., Hiebert, R., McCloskey, J., Kirksey, J., Cunningham, A.B., Gerlach, R., Spangler, L., Phillips, A.J.: Ureolysis-induced calcium carbonate precipitation (UICP) in the presence of CO_2-affected brine: A field demonstration. Int. J, Greenh. Gas Control (2021). https://doi.org/10.1016/j.ijggc.2021.103391

Krajewska, B.: Ureases I. Functional, catalytic and kinetic properties: A review. J. Mol. Catal. B Enzym. **59**(1–3), 9–21 (2009). https://doi.org/10.1016/j.molcatb.2009.01.003

Krajewska, B.: Urease-aided calcium carbonate mineralization for engineering applications: A review. J. Adv. Res. **13**, 59–67 (2018). https://doi.org/10.1016/j.jare.2017.10.009

Landa-Marbán, D., Tveit, S., Kumar, K., Gasda, S.E.: Practical approaches to study microbially induced calcite precipitation at the field scale. Int. J. Greenh. Gas Control (2021). https://doi.org/10.1016/j.ijggc.2021.103256

Minto, J.M., Lunn, R.J., El Mountassir, G.: Development of a reactive transport model for field-scale simulation of microbially induced carbonate precipitation. Water Resour. Res. **55**(8), 7229–7245 (2019). https://doi.org/10.1029/2019WR025153

Mountassir, G.E., Lunn, R.J., Moir, H., Maclachlan, E.: Hydrodynamic coupling in microbially mediated fracture mineralization: Formation of self-organized groundwater flow channels. Water Resources Research **50**(1), 1–16 (2014). https://doi.org/10.1002/2013WR013578

Mujah, D., Shahin, M.A., Cheng, L.: State-of-the-art review of biocementation by microbially induced calcite precipitation (MICP) for soil stabilization. Geomicrobiol. J. **34**(6), 524–537 (2017). https://doi.org/10.1080/01490451.2016.1225866

Nebel, H.: Kontrollierte Fällung von CaCO3 in einem modular aufgebauten Kristallisationsreaktor. In: PhD thesis, University of Duisburg-Essen, Essen (2008)

Nething, C., Smirnova, M., Gröning, J.A., Haase, W., Stolz, A., Sobek, W.: A method for 3D printing bio-cemented spatial structures using sand and urease active calcium carbonate powder. Mater. Des. (2020). https://doi.org/10.1016/j.matdes.2020.109032

Ni, M., Ratner, B.D.: Differentiating calcium carbonate polymorphs by surface analysis techniques - An XPS and TOF-SIMS study. Surf. Interface Anal. **40**(10), 1356–1361 (2008). https://doi.org/10.1002/sia.2904

Niu, Q., Zhang, C.: Permeability prediction in rocks experiencing mineral precipitation and dissolution: A numerical study. Water Resour. Res. **55**(4), 3107–3121 (2019). https://doi.org/10.1029/2018WR024174

Pandey, S.N., Chaudhuri, A., Rajaram, H., Kelkar, S.: Fracture transmissivity evolution due to silica dissolution/precipitation during geothermal heat extraction. Geothermics **57**, 111–126 (2015). https://doi.org/10.1016/j.geothermics.2015.06.011

Phillips, A.J., Gerlach, R., Lauchnor, E., Mitchell, A.C., Cunningham, A.B., Spangler, L.: Engineered applications of ureolytic biomineralization: A review. Biofouling **29**(6), 715–733 (2013). https://doi.org/10.1080/08927014.2013.796550

Phillips, A.J., Lauchnor, E., Eldring, J., Esposito, R., Mitchell, A.C., Gerlach, R., Cunningham, A.B., Spangler, L.H.: Potential CO_2 leakage reduction through biofilm-induced calcium carbonate precipitation. Environ. Sci. Technol. **47**(1), 142–149 (2013). https://doi.org/10.1021/es301294q

Phillips, A.J., Cunningham, A.B., Gerlach, R., Hiebert, R., Hwang, C., Lomans, B.P., Westrich, J., Mantilla, C., Kirksey, J., Esposito, R., Spangler, L.: Fracture sealing with microbially-induced calcium carbonate precipitation: A field study. Environ. Sci. Technol. **50**(7), 4111–4117 (2016). https://doi.org/10.1021/acs.est.5b05559

Qin, C.Z., Hassanizadeh, S.M., Ebigbo, A.: Pore-scale network modeling of microbially induced calcium carbonate precipitation: Insight into scale dependence of biogeochemical reaction rates. Water Resour. Res. **52**(11), 8794–8810 (2016). https://doi.org/10.1002/2016WR019128

Rahman, M., Hora, R.N., Ahenkorah, I., Beecham, S.: State-of-the-art review of microbial-induced calcite precipitation and its sustainability in engineering applications. Sustainability **12**(15), 6281 (2020). https://doi.org/10.3390/su12156281

Rodriguez-Blanco, J.D., Shaw, S., Benning, L.G.: The kinetics and mechanisms of amorphous calcium carbonate (ACC) crystallization to calcite, via vaterite. Nanoscale **3**(1), 265–271 (2011). https://doi.org/10.1039/c0nr00589d

Rodriguez-Navarro, C., Kudłacz, K., Cizer, Ö., Ruiz-Agudo, E.: Formation of amorphous calcium carbonate and its transformation into mesostructured calcite. CrystEngComm **17**(1), 58–72 (2015). https://doi.org/10.1039/C4CE01562B

Ruf, M., Steeb, H.: An open, modular, and flexible micro X-ray computed tomography system for research. Rev. Sci. Instrum. (2020). https://doi.org/10.1063/5.0019541

Sharp, R.R., Cunningham, A.B., Komlos, J., Billmayer, J.: Observation of thick biofilm accumulation and structure in porous media and corresponding hydrodynamic and mass transfer effects. Water Sci. Technol. **39**(7), 195–201 (1999). https://doi.org/10.2166/wst.1999.0359

Terzis, D., Laloui, L.: 3-D micro-architecture and mechanical response of soil cemented via microbial-induced calcite precipitation. Sci. Rep. **8**(1), 1–11 (2018). https://doi.org/10.1038/s41598-018-19895-w

Thullner, M.: Comparison of bioclogging effects in saturated porous media within one- and two-dimensional flow systems. Ecol. Eng. **36**(2), 176–196 (2010). https://doi.org/10.1016/j.ecoleng.2008.12.037

Vahid Dastjerdi, S., Steeb, H., Ruf, M., Lee, D., Weinhardt, F., Karadimitriou, N., Class, H.: Micro-XRCT Dataset of Enzymatically Induced Calcite Precipitation (EICP) in a Microfluidic Cell, V1, DaRUS (2021). https://doi.org/10.18419/darus-866

van Paassen, L.: Biogrout: Ground Improvement by Microbially Induced Carbonate Precipitation. In: PhD thesis, Delft University of Technology, Delft (2009)

Verma, A., Pruess, K.: Thermohydrological conditions and silica redistribution near high-level nuclear wastes emplaced in saturated geological formations. J. Geophys. Res. **93**(B2), 1159–1173 (1988). https://doi.org/10.1029/JB093iB02p01159

von Wolff, L., Weinhardt, F., Class, H., Hommel, J., Rohde, C.: Investigation of crystal growth in enzymatically induced calcite precipitation by micro-fluidic experimental methods and comparison with mathematical modeling. Transp. Porous Media **137**(2), 327–343 (2021). https://doi.org/10.1007/s11242-021-01560-y

Wang, Y., Soga, K., Dejong, J.T., Kabla, A.J.: A microfluidic chip and its use in characterising the particle-scale behaviour of microbial-induced calcium carbonate precipitation (MICP). Geotechnique **69**(12), 1086–1094 (2019). https://doi.org/10.1680/jgeot.18.P.031

Wang, Y., Soga, K., DeJong, J.T., Kabla, A.J.: Microscale visualization of microbial-induced calcium carbonate precipitation processes. J. Geotech. Geoenviron. Eng. **145**(9), 04019045 (2019). https://doi.org/10.1061/(asce)gt.1943-5606.0002079

Wang, Y., Soga, K., DeJong, J.T., Kabla, A.J.: Effects of bacterial density on growth rate and characteristics of microbial-induced $CaCO_3$ precipitates: Particle-scale experimental study. J. Geotech. Geoenviron. Eng. **147**(6), 04021036 (2021). https://doi.org/10.1061/(asce)gt.1943-5606.0002509

Weinhardt, F., Class, H., Vahid Dastjerdi, S., Karadimitriou, N., Lee, D., Steeb, H.: Optical Microscopy and Pressure Measurements of Enzymatically Induced Calcite Precipitation (EICP) in a Microfluidic Cell, V1 DaRUS (2021b). https://doi.org/10.18419/darus-818

Weinhardt, F., Deng, J., Steeb, H., Class, H.: Optical Microscopy and Log Data of Enzymatically Induced Calcite Precipitation (EICP) in Microfluidic Cells (Quasi-2D-structure), V1, DaRUS (2022). https://doi.org/10.18419/darus-1799

Weinhardt, F., Class, H., Vahid Dastjerdi, S., Karadimitriou, N., Lee, D., Steeb, H.: Experimental methods and imaging for enzymatically induced calcite precipitation in a microfluidic cell. Water Resour. Res. (2021a). https://doi.org/10.1029/2020WR029361

Xia, Y., Whitesides, G.M.: Soft lithography. Angew. Chem. Int. Ed. **37**(5), 550–575 (1998)

Zambare, N.M., Naser, N.Y., Gerlach, R., Chang, C.B.: Mineralogy of microbially induced calcium carbonate precipitates formed using single cell drop-based microfluidics. Sci. Rep. **10**, 17535 (2020). https://doi.org/10.1038/s41598-020-73870-y

Zhang, T., Klapper, I.: Critical occlusion via biofilm induced calcite precipitation in porous media. N. J. Phys. (2014). https://doi.org/10.1088/1367-2630/16/5/055009

Authors and Affiliations

Felix Weinhardt[1] · Jingxuan Deng[2] · Johannes Hommel[1] · Samaneh Vahid Dastjerdi[4] · Robin Gerlach[3] · Holger Steeb[4] · Holger Class[1]

[1] Department of Hydromechanics and Modelling of Hydrosystems, University of Stuttgart, Pfaffenwaldring 61, 70569 Stuttgart, Germany

[2] Department of Earth and Environmental Sciences, University of Minnesota, 116 Church Street Se Minneapolis, Minneapolis, MN 55455, USA

[3] Department of Chemical and Biological Engineering, Center for Biofilm Engineering, Montana State University, 366 Barnard Hall Bozeman, Bozeman, MT 59717-3980, USA

[4] Institute of Applied Mechanics, University of Stuttgart, Pfaffenwaldring 7, 70569 Stuttgart, Germany

Institut für Wasser- und Umweltsystemmodellierung
Universität Stuttgart

Pfaffenwaldring 61
70569 Stuttgart (Vaihingen)
Telefon (0711) 685 - 60156
Telefax (0711) 685 - 51073
E-Mail: iws@iws.uni-stuttgart.de
http://www.iws.uni-stuttgart.de

Verzeichnis der Mitteilungshefte

5 Plate, Erich: *Beitrag zur Bestimmung der Windgeschwindigkeitsverteilung in der durch eine Wand gestörten bodennahen Luftschicht*, und Röhnisch, Arthur; Marotz, Günter: *Neue Baustoffe und Bauausführungen für den Schutz der Böschungen und der Sohle von Kanälen, Flüssen und Häfen; Gestehungskosten und jeweilige Vorteile*, sowie Unny, T.E.: *Schwingungsuntersuchungen am Kegelstrahlschieber*, 1967

6 Seiler, Erich: *Die Ermittlung des Anlagenwertes der bundeseigenen Binnenschiffahrtsstraßen und Talsperren und des Anteils der Binnenschiffahrt an diesem Wert*, 1967

7 *Sonderheft anläßlich des 65. Geburtstages von Prof. Arthur Röhnisch mit Beiträgen von* Benk, Dieter; Breitling, J.; Gurr, Siegfried; Haberhauer, Robert; Honekamp, Hermann; Kuz, Klaus Dieter; Marotz, Günter; Mayer-Vorfelder, Hans-Jörg; Miller, Rudolf; Plate, Erich J.; Radomski, Helge; Schwarz, Helmut; Vollmer, Ernst; Wildenhahn, Eberhard; 1967

8 Jumikis, Alfred: *Beitrag zur experimentellen Untersuchung des Wassernachschubs in einem gefrierenden Boden und die Beurteilung der Ergebnisse*, 1968

9 Marotz, Günter: *Technische Grundlagen einer Wasserspeicherung im natürlichen Untergrund*, 1968

10 Radomski, Helge: *Untersuchungen über den Einfluß der Querschnittsform wellenförmiger Spundwände auf die statischen und rammtechnischen Eigenschaften*, 1968

11 Schwarz, Helmut: *Die Grenztragfähigkeit des Baugrundes bei Einwirkung vertikal gezogener Ankerplatten als zweidimensionales Bruchproblem*, 1969

12 Erbel, Klaus: *Ein Beitrag zur Untersuchung der Metamorphose von Mittelgebirgsschneedecken unter besonderer Berücksichtigung eines Verfahrens zur Bestimmung der thermischen Schneequalität*, 1969

13 Westhaus, Karl-Heinz: *Der Strukturwandel in der Binnenschiffahrt und sein Einfluß auf den Ausbau der Binnenschiffskanäle*, 1969

14 Mayer-Vorfelder, Hans-Jörg: *Ein Beitrag zur Berechnung des Erdwiderstandes unter Ansatz der logarithmischen Spirale als Gleitflächenfunktion*, 1970

15 Schulz, Manfred: *Berechnung des räumlichen Erddruckes auf die Wandung kreiszylindrischer Körper*, 1970

16 Mobasseri, Manoutschehr: *Die Rippenstützmauer. Konstruktion und Grenzen ihrer Standsicherheit*, 1970

17 Benk, Dieter: *Ein Beitrag zum Betrieb und zur Bemessung von Hochwasserrückhaltebecken*, 1970

18 Gàl, Attila: *Bestimmung der mitschwingenden Wassermasse bei überströmten Fischbauchklappen mit kreiszylindrischem Staublech*, 1971, *vergriffen*

19 Kuz, Klaus Dieter: *Ein Beitrag zur Frage des Einsetzens von Kavitationserscheinungen in einer Düsenströmung bei Berücksichtigung der im Wasser gelösten Gase*, 1971, *vergriffen*

20 Schaak, Hartmut: *Verteilleitungen von Wasserkraftanlagen*, 1971

21 *Sonderheft zur Eröffnung der neuen Versuchsanstalt des Instituts für Wasserbau der Universität Stuttgart mit Beiträgen von* Brombach, Hansjörg; Dirksen, Wolfram; Gàl, Attila; Gerlach, Reinhard; Giesecke, Jürgen; Holthoff, Franz-Josef; Kuz, Klaus Dieter; Marotz, Günter; Minor, Hans-Erwin; Petrikat, Kurt; Röhnisch, Arthur; Rueff, Helge; Schwarz, Helmut; Vollmer, Ernst; Wildenhahn, Eberhard; 1972

22 Wang, Chung-su: *Ein Beitrag zur Berechnung der Schwingungen an Kegelstrahlschiebern*, 1972

23 Mayer-Vorfelder, Hans-Jörg: *Erdwiderstandsbeiwerte nach dem Ohde-Variationsverfahren*, 1972

24 Minor, Hans-Erwin: *Beitrag zur Bestimmung der Schwingungsanfachungsfunktionen überströmter Stauklappen*, 1972, *vergriffen*

25 Brombach, Hansjörg: *Untersuchung strömungsmechanischer Elemente (Fluidik) und die Möglichkeit der Anwendung von Wirbelkammerelementen im Wasserbau*, 1972, *vergriffen*

26 Wildenhahn, Eberhard: *Beitrag zur Berechnung von Horizontalfilterbrunnen*, 1972

27 Steinlein, Helmut: *Die Eliminierung der Schwebstoffe aus Flußwasser zum Zweck der unterirdischen Wasserspeicherung, gezeigt am Beispiel der Iller*, 1972

28 Holthoff, Franz Josef: *Die Überwindung großer Hubhöhen in der Binnenschiffahrt durch Schwimmerhebewerke*, 1973

29 Röder, Karl: *Einwirkungen aus Baugrundbewegungen auf trog- und kastenförmige Konstruktionen des Wasser- und Tunnelbaues*, 1973

30 Kretschmer, Heinz: *Die Bemessung von Bogenstaumauern in Abhängigkeit von der Talform*, 1973

31 Honekamp, Hermann: *Beitrag zur Berechnung der Montage von Unterwasserpipelines*, 1973

32 Giesecke, Jürgen: *Die Wirbelkammertriode als neuartiges Steuerorgan im Wasserbau*, und Brombach, Hansjörg: *Entwicklung, Bauformen, Wirkungsweise und Steuereigenschaften von Wirbelkammerverstärkern*, 1974

33 Rueff, Helge: *Untersuchung der schwingungserregenden Kräfte an zwei hintereinander angeordneten Tiefschützen unter besonderer Berücksichtigung von Kavitation*, 1974

34 Röhnisch, Arthur: *Einpreßversuche mit Zementmörtel für Spannbeton - Vergleich der Ergebnisse von Modellversuchen mit Ausführungen in Hüllwellrohren*, 1975

35 *Sonderheft anläßlich des 65. Geburtstages von Prof. Dr.-Ing. Kurt Petrikat mit Beiträgen von*: Brombach, Hansjörg; Erbel, Klaus; Flinspach, Dieter; Fischer jr., Richard; Gàl, Attila; Gerlach, Reinhard; Giesecke, Jürgen; Haberhauer, Robert; Hafner Edzard; Hausenblas, Bernhard; Horlacher, Hans-Burkhard; Hutarew, Andreas; Knoll, Manfred; Krummet, Ralph; Marotz, Günter; Merkle, Theodor; Miller, Christoph; Minor, Hans-Erwin; Neumayer, Hans; Rao, Syamala; Rath, Paul; Rueff, Helge; Ruppert, Jürgen; Schwarz, Wolfgang; Topal-Gökceli, Mehmet; Vollmer, Ernst; Wang, Chung-su; Weber, Hans-Georg; 1975

36 Berger, Jochum: *Beitrag zur Berechnung des Spannungszustandes in rotationssymmetrisch belasteten Kugelschalen veränderlicher Wandstärke unter Gas- und Flüssigkeitsdruck durch Integration schwach singulärer Differentialgleichungen*, 1975

37 Dirksen, Wolfram: *Berechnung instationärer Abflußvorgänge in gestauten Gerinnen mittels Differenzenverfahren und die Anwendung auf Hochwasserrückhaltebecken*, 1976

38 Horlacher, Hans-Burkhard: *Berechnung instationärer Temperatur- und Wärmespannungsfelder in langen mehrschichtigen Hohlzylindern*, 1976

39 Hafner, Edzard: *Untersuchung der hydrodynamischen Kräfte auf Baukörper im Tiefwasserbereich des Meeres*, 1977, ISBN 3-921694-39-6

40 Ruppert, Jürgen: *Über den Axialwirbelkammerverstärker für den Einsatz im Wasserbau*, 1977, ISBN 3-921694-40-X

41 Hutarew, Andreas: *Beitrag zur Beeinflußbarkeit des Sauerstoffgehalts in Fließgewässern an Abstürzen und Wehren*, 1977, ISBN 3-921694-41-8, *vergriffen*

42 Miller, Christoph: *Ein Beitrag zur Bestimmung der schwingungserregenden Kräfte an unterströmten Wehren*, 1977, ISBN 3-921694-42-6

43 Schwarz, Wolfgang: *Druckstoßberechnung unter Berücksichtigung der Radial- und Längsverschiebungen der Rohrwandung*, 1978, ISBN 3-921694-43-4

44 Kinzelbach, Wolfgang: *Numerische Untersuchungen über den optimalen Einsatz variabler Kühlsysteme einer Kraftwerkskette am Beispiel Oberrhein*, 1978, ISBN 3-921694-44-2

45 Barczewski, Baldur: *Neue Meßmethoden für Wasser-Luftgemische und deren Anwendung auf zweiphasige Auftriebsstrahlen*, 1979, ISBN 3-921694-45-0

46 Neumayer, Hans: *Untersuchung der Strömungsvorgänge in radialen Wirbelkammerverstärkern*, 1979, ISBN 3-921694-46-9

47 Elalfy, Youssef-Elhassan: *Untersuchung der Strömungsvorgänge in Wirbelkammerdioden und -drosseln*, 1979, ISBN 3-921694-47-7

48 Brombach, Hansjörg: *Automatisierung der Bewirtschaftung von Wasserspeichern*, 1981, ISBN 3-921694-48-5

49 Geldner, Peter: *Deterministische und stochastische Methoden zur Bestimmung der Selbstdichtung von Gewässern*, 1981, ISBN 3-921694-49-3, *vergriffen*

50 Mehlhorn, Hans: *Temperaturveränderungen im Grundwasser durch Brauchwassereinleitungen*, 1982, ISBN 3-921694-50-7, *vergriffen*

51 Hafner, Edzard: *Rohrleitungen und Behälter im Meer*, 1983, ISBN 3-921694-51-5

52 Rinnert, Bernd: *Hydrodynamische Dispersion in porösen Medien: Einfluß von Dichteunterschieden auf die Vertikalvermischung in horizontaler Strömung*, 1983, ISBN 3-921694-52-3, *vergriffen*

53 Lindner, Wulf: *Steuerung von Grundwasserentnahmen unter Einhaltung ökologischer Kriterien*, 1983, ISBN 3-921694-53-1, *vergriffen*

54 Herr, Michael; Herzer, Jörg; Kinzelbach, Wolfgang; Kobus, Helmut; Rinnert, Bernd: *Methoden zur rechnerischen Erfassung und hydraulischen Sanierung von Grundwasserkontaminationen*, 1983, ISBN 3-921694-54-X

55 Schmitt, Paul: *Wege zur Automatisierung der Niederschlagsermittlung*, 1984, ISBN 3-921694-55-8, *vergriffen*

56 Müller, Peter: *Transport und selektive Sedimentation von Schwebstoffen bei gestautem Abfluß*, 1985, ISBN 3-921694-56-6

57 El-Qawasmeh, Fuad: *Möglichkeiten und Grenzen der Tropfbewässerung unter besonderer Berücksichtigung der Verstopfungsanfälligkeit der Tropfelemente*, 1985, ISBN 3-921694-57-4, *vergriffen*

58 Kirchenbaur, Klaus: *Mikroprozessorgesteuerte Erfassung instationärer Druckfelder am Beispiel seegangsbelasteter Baukörper*, 1985, ISBN 3-921694-58-2

59 Kobus, Helmut (Hrsg.): *Modellierung des großräumigen Wärme- und Schadstofftransports im Grundwasser*, Tätigkeitsbericht 1984/85 (DFG-Forschergruppe an den Universitäten Hohenheim, Karlsruhe und Stuttgart), 1985, ISBN 3-921694-59-0, *vergriffen*

60 Spitz, Karlheinz: *Dispersion in porösen Medien: Einfluß von Inhomogenitäten und Dichteunterschieden*, 1985, ISBN 3-921694-60-4, *vergriffen*

61 Kobus, Helmut: *An Introduction to Air-Water Flows in Hydraulics*, 1985, ISBN 3-921694-61-2

62 Kaleris, Vassilios: *Erfassung des Austausches von Oberflächen- und Grundwasser in horizontalebenen Grundwassermodellen*, 1986, ISBN 3-921694-62-0

63 Herr, Michael: *Grundlagen der hydraulischen Sanierung verunreinigter Porengrundwasserleiter*, 1987, ISBN 3-921694-63-9

64 Marx, Walter: *Berechnung von Temperatur und Spannung in Massenbeton infolge Hydratation*, 1987, ISBN 3-921694-64-7

65 Koschitzky, Hans-Peter: *Dimensionierungskonzept für Sohlbelüfter in Schußrinnen zur Vermeidung von Kavitationsschäden*, 1987, ISBN 3-921694-65-5

66 Kobus, Helmut (Hrsg.): *Modellierung des großräumigen Wärme- und Schadstofftransports im Grundwasser*, Tätigkeitsbericht 1986/87 (DFG-Forschergruppe an den Universitäten Hohenheim, Karlsruhe und Stuttgart) 1987, ISBN 3-921694-66-3

67 Söll, Thomas: *Berechnungsverfahren zur Abschätzung anthropogener Temperaturanomalien im Grundwasser*, 1988, ISBN 3-921694-67-1

68 Dittrich, Andreas; Westrich, Bernd: *Bodenseeufererosion, Bestandsaufnahme und Bewertung*, 1988, ISBN 3-921694-68-X, *vergriffen*

69 Huwe, Bernd; van der Ploeg, Rienk R.: *Modelle zur Simulation des Stickstoffhaushaltes von Standorten mit unterschiedlicher landwirtschaftlicher Nutzung*, 1988, ISBN 3-921694-69-8, *vergriffen*

70 Stephan, Karl: *Integration elliptischer Funktionen*, 1988, ISBN 3-921694-70-1

71 Kobus, Helmut; Zilliox, Lothaire (Hrsg.): *Nitratbelastung des Grundwassers, Auswirkungen der Landwirtschaft auf die Grundwasser- und Rohwasserbeschaffenheit und Maßnahmen zum Schutz des Grundwassers*. Vorträge des deutsch-französischen Kolloquiums am 6. Oktober 1988, Universitäten Stuttgart und Louis Pasteur Strasbourg (Vorträge in deutsch oder französisch, Kurzfassungen zweisprachig), 1988, ISBN 3-921694-71-X

72 Soyeaux, Renald: *Unterströmung von Stauanlagen auf klüftigem Untergrund unter Berücksichtigung laminarer und turbulenter Fließzustände*,1991, ISBN 3-921694-72-8

73 Kohane, Roberto: *Berechnungsmethoden für Hochwasserabfluß in Fließgewässern mit überströmten Vorländern*, 1991, ISBN 3-921694-73-6

74 Hassinger, Reinhard: *Beitrag zur Hydraulik und Bemessung von Blocksteinrampen in flexibler Bauweise*, 1991, ISBN 3-921694-74-4, *vergriffen*

75 Schäfer, Gerhard: *Einfluß von Schichtenstrukturen und lokalen Einlagerungen auf die Längsdispersion in Porengrundwasserleitern*, 1991, ISBN 3-921694-75-2

76 Giesecke, Jürgen: *Vorträge, Wasserwirtschaft in stark besiedelten Regionen; Umweltforschung mit Schwerpunkt Wasserwirtschaft*, 1991, ISBN 3-921694-76-0

77 Huwe, Bernd: *Deterministische und stochastische Ansätze zur Modellierung des Stickstoffhaushalts landwirtschaftlich genutzter Flächen auf unterschiedlichem Skalenniveau*, 1992, ISBN 3-921694-77-9, *vergriffen*

78 Rommel, Michael: *Verwendung von Kluftdaten zur realitätsnahen Generierung von Kluftnetzen mit anschließender laminar-turbulenter Strömungsberechnung*, 1993, ISBN 3-92 1694-78-7

79 Marschall, Paul: *Die Ermittlung lokaler Stofffrachten im Grundwasser mit Hilfe von Einbohrloch-Meßverfahren*, 1993, ISBN 3-921694-79-5, *vergriffen*

80 Ptak, Thomas: *Stofftransport in heterogenen Porenaquiferen: Felduntersuchungen und stochastische Modellierung*, 1993, ISBN 3-921694-80-9, *vergriffen*

81 Haakh, Frieder: *Transientes Strömungsverhalten in Wirbelkammern,* 1993, ISBN 3-921694-81-7

82 Kobus, Helmut; Cirpka, Olaf; Barczewski, Baldur; Koschitzky, Hans-Peter: *Versuchseinrichtung zur Grundwasser- und Altlastensanierung VEGAS, Konzeption und Programmrahmen*, 1993, ISBN 3-921694-82-5

83 Zang, Weidong: *Optimaler Echtzeit-Betrieb eines Speichers mit aktueller Abflußregenerierung*, 1994, ISBN 3-921694-83-3, *vergriffen*

84 Franke, Hans-Jörg: *Stochastische Modellierung eines flächenhaften Stoffeintrages und Transports in Grundwasser am Beispiel der Pflanzenschutzmittelproblematik*, 1995, ISBN 3-921694-84-1

85 Lang, Ulrich: *Simulation regionaler Strömungs- und Transportvorgänge in Karstaquiferen mit Hilfe des Doppelkontinuum-Ansatzes: Methodenentwicklung und Parameteridenti-fikation*, 1995, ISBN 3-921694-85-X, *vergriffen*

86 Helmig, Rainer: *Einführung in die Numerischen Methoden der Hydromechanik*, 1996, ISBN 3-921694-86-8, *vergriffen*

87 Cirpka, Olaf: *CONTRACT: A Numerical Tool for Contaminant Transport and Chemical Transformations - Theory and Program Documentation -*, 1996, ISBN 3-921694-87-6

88 Haberlandt, Uwe: *Stochastische Synthese und Regionalisierung des Niederschlages für Schmutzfrachtberechnungen*, 1996, ISBN 3-921694-88-4

89 Croisé, Jean: *Extraktion von flüchtigen Chemikalien aus natürlichen Lockergesteinen mittels erzwungener Luftströmung*, 1996, ISBN 3-921694-89-2, *vergriffen*

90 Jorde, Klaus: *Ökologisch begründete, dynamische Mindestwasserregelungen bei Ausleitungskraftwerken*, 1997, ISBN 3-921694-90-6, *vergriffen*

91 Helmig, Rainer: *Gekoppelte Strömungs- und Transportprozesse im Untergrund - Ein Beitrag zur Hydrosystemmodellierung-*, 1998, ISBN 3-921694-91-4, *vergriffen*

92 Emmert, Martin: *Numerische Modellierung nichtisothermer Gas-Wasser Systeme in porösen Medien,* 1997, ISBN 3-921694-92-2

93 Kern, Ulrich: *Transport von Schweb- und Schadstoffen in staugeregelten Fließgewässern am Beispiel des Neckars*, 1997, ISBN 3-921694-93-0, *vergriffen*

94 Förster, Georg: *Druckstoßdämpfung durch große Luftblasen in Hochpunkten von Rohrleitungen 1997*, ISBN 3-921694-94-9

95 Cirpka, Olaf: *Numerische Methoden zur Simulation des reaktiven Mehrkomponententransports im Grundwasser*, 1997, ISBN 3-921694-95-7, *vergriffen*

96 Färber, Arne: *Wärmetransport in der ungesättigten Bodenzone: Entwicklung einer thermischen In-situ-Sanierungstechnologie*, 1997, ISBN 3-921694-96-5

97 Betz, Christoph: *Wasserdampfdestillation von Schadstoffen im porösen Medium: Entwicklung einer thermischen In-situ-Sanierungstechnologie*, 1998, SBN 3-921694-97-3

98 Xu, Yichun: *Numerical Modeling of Suspended Sediment Transport in Rivers*, 1998, ISBN 3-921694-98-1, *vergriffen*

99 Wüst, Wolfgang: *Geochemische Untersuchungen zur Sanierung CKW-kontaminierter Aquifere mit Fe(0)-Reaktionswänden,* 2000, ISBN 3-933761-02-2

100 Sheta, Hussam: *Simulation von Mehrphasenvorgängen in porösen Medien unter Einbeziehung von Hysterese-Effekten*, 2000, ISBN 3-933761-03-4

101 Ayros, Edwin: *Regionalisierung extremer Abflüsse auf der Grundlage statistischer Verfahren*, 2000, ISBN 3-933761-04-2, *vergriffen*

102 Huber, Ralf: *Compositional Multiphase Flow and Transport in Heterogeneous Porous Media*, 2000, ISBN 3-933761-05-0

103 Braun, Christopherus: *Ein Upscaling-Verfahren für Mehrphasenströmungen in porösen Medien*, 2000, ISBN 3-933761-06-9

104 Hofmann, Bernd: *Entwicklung eines rechnergestützten Managementsystems zur Beurteilung von Grundwasserschadensfällen*, 2000, ISBN 3-933761-07-7

105 Class, Holger: *Theorie und numerische Modellierung nichtisothermer Mehrphasenprozesse in NAPL-kontaminierten porösen Medien,* 2001, ISBN 3-933761-08-5

106 Schmidt, Reinhard: *Wasserdampf- und Heißluftinjektion zur thermischen Sanierung kontaminierter Standorte*, 2001, ISBN 3-933761-09-3

107 Josef, Reinhold: *Schadstoffextraktion mit hydraulischen Sanierungsverfahren unter Anwendung von grenzflächenaktiven Stoffen*, 2001, ISBN 3-933761-10-7

108 Schneider, Matthias: *Habitat- und Abflussmodellierung für Fließgewässer mit unscharfen Berechnungsansätzen*, 2001, ISBN 3-933761-11-5

109 Rathgeb, Andreas: *Hydrodynamische Bemessungsgrundlagen für Lockerdeckwerke an überströmbaren Erddämmen*, 2001, ISBN 3-933761-12-3

110 Lang, Stefan: *Parallele numerische Simulation instätionärer Probleme mit adaptiven Methoden auf unstrukturierten Gittern*, 2001, ISBN 3-933761-13-1

111 Appt, Jochen; Stumpp Simone: *Die Bodensee-Messkampagne 2001, IWS/CWR Lake Constance Measurement Program 2001*, 2002, ISBN 3-933761-14-X

112 Heimerl, Stephan: *Systematische Beurteilung von Wasserkraftprojekten,* 2002, ISBN 3-933761-15-8, *vergriffen*

113 Iqbal, Amin: *On the Management and Salinity Control of Drip Irrigation,* 2002, ISBN 3-933761-16-6

114 Silberhorn-Hemminger, Annette: *Modellierung von Kluftaquifersystemen: Geostatistische Analyse und deterministisch-stochastische Kluftgenerierung,* 2002, ISBN 3-933761-17-4

115 Winkler, Angela: *Prozesse des Wärme- und Stofftransports bei der In-situ-Sanierung mit festen Wärmequellen,* 2003, ISBN 3-933761-18-2

116 Marx, Walter: *Wasserkraft, Bewässerung, Umwelt - Planungs- und Bewertungsschwerpunkte der Wasserbewirtschaftung,* 2003, ISBN 3-933761-19-0

117 Hinkelmann, Reinhard: *Efficient Numerical Methods and Information-Processing Techniques in Environment Water,* 2003, ISBN 3-933761-20-4

118 Samaniego-Eguiguren, Luis Eduardo: *Hydrological Consequences of Land Use / Land Cover and Climatic Changes in Mesoscale Catchments*, 2003, ISBN 3-933761-21-2

119 Neunhäuserer, Lina: *Diskretisierungsansätze zur Modellierung von Strömungs- und Transportprozessen in geklüftet-porösen Medien*, 2003, ISBN 3-933761-22-0

120 Paul, Maren: *Simulation of Two-Phase Flow in Heterogeneous Poros Media with Adaptive Methods*, 2003, ISBN 3-933761-23-9

121 Ehret, Uwe: *Rainfall and Flood Nowcasting in Small Catchments using Weather Radar*, 2003, ISBN 3-933761-24-7

122 Haag, Ingo: *Der Sauerstoffhaushalt staugeregelter Flüsse am Beispiel des Neckars - Analysen, Experimente, Simulationen -,* 2003, ISBN 3-933761-25-5

123 Appt, Jochen: *Analysis of Basin-Scale Internal Waves in Upper Lake Constance,* 2003, ISBN 3-933761-26-3

124 Hrsg.: Schrenk, Volker; Batereau, Katrin; Barczewski, Baldur; Weber, Karolin und Koschitzky, Hans-Peter: *Symposium Ressource Fläche und VEGAS - Statuskolloquium 2003, 30. September und 1. Oktober 2003,* 2003, ISBN 3-933761-27-1

125 Omar Khalil Ouda: *Optimisation of Agricultural Water Use: A Decision Support System for the Gaza Strip,* 2003, ISBN 3-933761-28-0

126 Batereau, Katrin: *Sensorbasierte Bodenluftmessung zur Vor-Ort-Erkundung von Schadensherden im Untergrund*, 2004, ISBN 3-933761-29-8

127 Witt, Oliver: *Erosionsstabilität von Gewässersedimenten mit Auswirkung auf den Stofftransport bei Hochwasser am Beispiel ausgewählter Stauhaltungen des Oberrheins*, 2004, ISBN 3-933761-30-1

128 Jakobs, Hartmut: *Simulation nicht-isothermer Gas-Wasser-Prozesse in komplexen Kluft-Matrix-Systemen*, 2004, ISBN 3-933761-31-X

129 Li, Chen-Chien: *Deterministisch-stochastisches Berechnungskonzept zur Beurteilung der Auswirkungen erosiver Hochwasserereignisse in Flussstauhaltungen,* 2004, ISBN 3-933761-32-8

130 Reichenberger, Volker; Helmig, Rainer; Jakobs, Hartmut; Bastian, Peter; Niessner, Jennifer: *Complex Gas-Water Processes in Discrete Fracture-Matrix Systems: Up-scaling, Mass-Conservative Discretization and Efficient Multilevel Solution,* 2004, ISBN 3-933761-33-6

131 Hrsg.: Barczewski, Baldur; Koschitzky, Hans-Peter; Weber, Karolin; Wege, Ralf: *VEGAS - Statuskolloquium 2004,* Tagungsband zur Veranstaltung am 05. Oktober 2004 an der Universität Stuttgart, Campus Stuttgart-Vaihingen, 2004, ISBN 3-933761-34-4

132 Asie, Kemal Jabir: *Finite Volume Models for Multiphase Multicomponent Flow through Porous Media*. 2005, ISBN 3-933761-35-2

133 Jacoub, George: *Development of a 2-D Numerical Module for Particulate Contaminant Transport in Flood Retention Reservoirs and Impounded Rivers,* 2004, ISBN 3-933761-36-0

134 Nowak, Wolfgang: *Geostatistical Methods for the Identification of Flow and Transport Parameters in the Subsurface,* 2005, ISBN 3-933761-37-9

135 Süß, Mia: *Analysis of the influence of structures and boundaries on flow and transport processes in fractured porous media*, 2005, ISBN 3-933761-38-7

136 Jose, Surabhin Chackiath: *Experimental Investigations on Longitudinal Dispersive Mixing in Heterogeneous Aquifers,* 2005, ISBN: 3-933761-39-5

137 Filiz, Fulya: *Linking Large-Scale Meteorological Conditions to Floods in Mesoscale Catchments,* 2005, ISBN 3-933761-40-9

138 Qin, Minghao: *Wirklichkeitsnahe und recheneffiziente Ermittlung von Temperatur und Spannungen bei großen RCC-Staumauern*, 2005, ISBN 3-933761-41-7

139 Kobayashi, Kenichiro: *Optimization Methods for Multiphase Systems in the Subsurface - Application to Methane Migration in Coal Mining Areas*, 2005, ISBN 3-933761-42-5

140 Rahman, Md. Arifur: *Experimental Investigations on Transverse Dispersive Mixing in Heterogeneous Porous Media,* 2005, ISBN 3-933761-43-3

141 Schrenk, Volker: *Ökobilanzen zur Bewertung von Altlastensanierungsmaßnahmen,* 2005, ISBN 3-933761-44-1

142 Hundecha, Hirpa Yeshewatesfa: *Regionalization of Parameters of a Conceptual Rainfall-Runoff Model*, 2005, ISBN: 3-933761-45-X

143 Wege, Ralf: *Untersuchungs- und Überwachungsmethoden für die Beurteilung natürlicher Selbstreinigungsprozesse im Grundwasser,* 2005, ISBN 3-933761-46-8

144 Breiting, Thomas: *Techniken und Methoden der Hydroinformatik - Modellierung von komplexen Hydrosystemen im Untergrund*, 2006, ISBN 3-933761-47-6

145 Hrsg.: Braun, Jürgen; Koschitzky, Hans-Peter; Müller, Martin: *Ressource Untergrund: 10 Jahre VEGAS: Forschung und Technologieentwicklung zum Schutz von Grundwasser und Boden,* Tagungsband zur Veranstaltung am 28. und 29. September 2005 an der Universität Stuttgart, Campus Stuttgart-Vaihingen, 2005, ISBN 3-933761-48-4

146 Rojanschi, Vlad: *Abflusskonzentration in mesoskaligen Einzugsgebieten unter Berücksichtigung des Sickerraumes,* 2006, ISBN 3-933761-49-2

147 Winkler, Nina Simone: *Optimierung der Steuerung von Hochwasserrückhaltebeckensystemen,* 2006, ISBN 3-933761-50-6

148 Wolf, Jens: *Räumlich differenzierte Modellierung der Grundwasserströmung alluvialer Aquifere für mesoskalige Einzugsgebiete*, 2006, ISBN: 3-933761-51-4

149 Kohler, Beate: *Externe Effekte der Laufwasserkraftnutzung*, 2006, ISBN 3-933761-52-2

150 Hrsg.: Braun, Jürgen; Koschitzky, Hans-Peter; Stuhrmann, Matthias: *VEGAS-Statuskolloquium 2006,* Tagungsband zur Veranstaltung am 28. September 2006 an der Universität Stuttgart, Campus Stuttgart-Vaihingen, 2006, ISBN 3-933761-53-0

151 Niessner, Jennifer: *Multi-Scale Modeling of Multi-Phase - Multi-Component Processes in Heterogeneous Porous Media*, 2006, ISBN 3-933761-54-9

152 Fischer, Markus: *Beanspruchung eingeerdeter Rohrleitungen infolge Austrocknung bindiger Böden,* 2006, ISBN 3-933761-55-7

153 Schneck, Alexander: *Optimierung der Grundwasserbewirtschaftung unter Berücksichtigung der Belange der Wasserversorgung, der Landwirtschaft und des Naturschutzes*, 2006, ISBN 3-933761-56-5

154 Das, Tapash: *The Impact of Spatial Variability of Precipitation on the Predictive Uncertainty of Hydrological Models,* 2006, ISBN 3-33761-57-3

155 Bielinski, Andreas: *Numerical Simulation of CO_2 sequestration in geological formations*, 2007, ISBN 3-933761-58-1

156 Mödinger, Jens: *Entwicklung eines Bewertungs- und Entscheidungsunterstützungssystems für eine nachhaltige regionale Grundwasserbewirtschaftung*, 2006, ISBN 3-933761-60-3

157 Manthey, Sabine: *Two-phase flow processes with dynamic effects in porous media - parameter estimation and simulation,* 2007, ISBN 3-933761-61-1

158 Pozos Estrada, Oscar: *Investigation on the Effects of Entrained Air in Pipelines,* 2007, ISBN 3-933761-62-X

159 Ochs, Steffen Oliver: *Steam injection into saturated porous media – process analysis including experimental and numerical investigations*, 2007, ISBN 3-933761-63-8

160 Marx, Andreas: *Einsatz gekoppelter Modelle und Wetterradar zur Abschätzung von Niederschlagsintensitäten und zur Abflussvorhersage, 2007,* ISBN 3-933761-64-6

161 Hartmann, Gabriele Maria: *Investigation of Evapotranspiration Concepts in Hydrological Modelling for Climate Change Impact Assessment*, 2007, ISBN 3-933761-65-4

162 Kebede Gurmessa, Tesfaye: *Numerical Investigation on Flow and Transport Characteristics to Improve Long-Term Simulation of Reservoir Sedimentation*, 2007, ISBN 3-933761-66-2

163 Trifković, Aleksandar: *Multi-objective and Risk-based Modelling Methodology for Planning, Design and Operation of Water Supply Systems*, 2007, ISBN 3-933761-67-0

164 Götzinger, Jens: *Distributed Conceptual Hydrological Modelling - Simulation of Climate, Land Use Change Impact and Uncertainty Analysis*, 2007, ISBN 3-933761-68-9

165 Hrsg.: Braun, Jürgen; Koschitzky, Hans-Peter; Stuhrmann, Matthias: *VEGAS – Kolloquium 2007,* Tagungsband zur Veranstaltung am 26. September 2007 an der Universität Stuttgart, Campus Stuttgart-Vaihingen, 2007, ISBN 3-933761-69-7

166 Freeman, Beau: *Modernization Criteria Assessment for Water Resources Planning; Klamath Irrigation Project, U.S.*, 2008, ISBN 3-933761-70-0

167 Dreher, Thomas: *Selektive Sedimentation von Feinstschwebstoffen in Wechselwirkung mit wandnahen turbulenten Strömungsbedingungen*, 2008, ISBN 3-933761-71-9

168 Yang, Wei: *Discrete-Continuous Downscaling Model for Generating Daily Precipitation Time Series*, 2008, ISBN 3-933761-72-7

169 Kopecki, Ianina: *Calculational Approach to FST-Hemispheres for Multiparametrical Benthos Habitat Modelling,* 2008*,* ISBN 3-933761-73-5

170 Brommundt, Jürgen: *Stochastische Generierung räumlich zusammenhängender Niederschlagszeitreihen*, 2008, ISBN 3-933761-74-3

171 Papafotiou, *Alexandros: Numerical Investigations of the Role of Hysteresis in Heterogeneous Two-Phase Flow Systems*, 2008, ISBN 3-933761-75-1

172 He, Yi: *Application of a Non-Parametric Classification Scheme to Catchment Hydrology*, 2008, ISBN 978-3-933761-76-7

173 Wagner, Sven: *Water Balance in a Poorly Gauged Basin in West Africa Using Atmospheric Modelling and Remote Sensing Information*, 2008, ISBN 978-3-933761-77-4

174 Hrsg.: Braun, Jürgen; Koschitzky, Hans-Peter; Stuhrmann, Matthias; Schrenk, Volker: *VEGAS-Kolloquium 2008 Ressource Fläche III*, Tagungsband zur Veranstaltung am 01. Oktober 2008 an der Universität Stuttgart, Campus Stuttgart-Vaihingen, 2008, ISBN 978-3-933761-78-1

175 Patil, Sachin: *Regionalization of an Event Based Nash Cascade Model for Flood Predictions in Ungauged Basins*, 2008, ISBN 978-3-933761-79-8

176 Assteerawatt, Anongnart: *Flow and Transport Modelling of Fractured Aquifers based on a Geostatistical Approach,* 2008, ISBN 978-3-933761-80-4

177 Karnahl, Joachim Alexander: *2D numerische Modellierung von multifraktionalem Schwebstoff- und Schadstofftransport in Flüssen*, 2008, ISBN 978-3-933761-81-1

178 Hiester, Uwe: *Technologieentwicklung zur In-situ-Sanierung der ungesättigten Bodenzone mit festen Wärmequellen,* 2009, ISBN 978-3-933761-82-8

179 Laux, Patrick: *Statistical Modeling of Precipitation for Agricultural Planning in the Volta Basin of West Africa,* 2009, ISBN 978-3-933761-83-5

180 Ehsan, Saqib: *Evaluation of Life Safety Risks Related to Severe Flooding,* 2009, ISBN 978-3-933761-84-2

181 Prohaska, Sandra: *Development and Application of a 1D Multi-Strip Fine Sediment Transport Model for Regulated Rivers,* 2009, ISBN 978-3-933761-85-9

182 Kopp, Andreas: *Evaluation of CO_2 Injection Processes in Geological Formations for Site Screening,* 2009, ISBN 978-3-933761-86-6

183 Ebigbo, Anozie: *Modelling of biofilm growth and its influence on CO_2 and water (two-phase) flow in porous media,* 2009, ISBN 978-3-933761-87-3

184 Freiboth, Sandra: *A phenomenological model for the numerical simulation of multiphase multicomponent processes considering structural alterations of porous media*, 2009, ISBN 978-3-933761-88-0

185 Zöllner, Frank: *Implementierung und Anwendung netzfreier Methoden im Konstruktiven Wasserbau und in der Hydromechanik*, 2009, ISBN 978-3-933761-89-7

186 Vasin, Milos: *Influence of the soil structure and property contrast on flow and transport in the unsaturated zone*, 2010, ISBN 978-3-933761-90-3

187 Li, Jing: *Application of Copulas as a New Geostatistical Tool*, 2010, ISBN 978-3-933761-91-0

188 AghaKouchak, Amir: *Simulation of Remotely Sensed Rainfall Fields Using Copulas*, 2010, ISBN 978-3-933761-92-7

189 Thapa, Pawan Kumar: *Physically-based spatially distributed rainfall runoff modelling for soil erosion estimation*, 2010, ISBN 978-3-933761-93-4

190 Wurms, Sven: *Numerische Modellierung der Sedimentationsprozesse in Retentionsanlagen zur Steuerung von Stoffströmen bei extremen Hochwasserabflussereignissen*, 2011, ISBN 978-3-933761-94-1

191 Merkel, Uwe: *Unsicherheitsanalyse hydraulischer Einwirkungen auf Hochwasserschutzdeiche und Steigerung der Leistungsfähigkeit durch adaptive Strömungsmodellierung*, 2011, ISBN 978-3-933761-95-8

192 Fritz, Jochen: *A Decoupled Model for Compositional Non-Isothermal Multiphase Flow in Porous Media and Multiphysics Approaches for Two-Phase Flow*, 2010, ISBN 978-3-933761-96-5

193 Weber, Karolin (Hrsg.): *12. Treffen junger WissenschaftlerInnen an Wasserbauinstituten*, 2010, ISBN 978-3-933761-97-2

194 Bliefernicht, Jan-Geert: *Probability Forecasts of Daily Areal Precipitation for Small River Basins,* 2011, ISBN 978-3-933761-98-9

195 Hrsg.: Koschitzky, Hans-Peter; Braun, Jürgen: *VEGAS-Kolloquium 2010 In-situ-Sanierung - Stand und Entwicklung Nano und ISCO -,* Tagungsband zur Veranstaltung am 07. Oktober 2010 an der Universität Stuttgart, Campus Stuttgart-Vaihingen*,* 2010*,* ISBN 978-3-933761-99-6

196 Gafurov, Abror: *Water Balance Modeling Using Remote Sensing Information - Focus on Central Asia,* 2010, ISBN 978-3-942036-00-9

197 Mackenberg, Sylvia: *Die Quellstärke in der Sickerwasserprognose: Möglichkeiten und Grenzen von Labor- und Freilanduntersuchungen,* 2010, ISBN 978-3-942036-01-6

198 Singh, Shailesh Kumar: *Robust Parameter Estimation in Gauged and Ungauged Basins,* 2010, ISBN 978-3-942036-02-3

199 Doğan, Mehmet Onur: *Coupling of porous media flow with pipe flow,* 2011, ISBN 978-3-942036-03-0

200 Liu, Min: *Study of Topographic Effects on Hydrological Patterns and the Implication on Hydrological Modeling and Data Interpolation,* 2011, ISBN 978-3-942036-04-7

201 Geleta, Habtamu Itefa: *Watershed Sediment Yield Modeling for Data Scarce Areas,* 2011, ISBN 978-3-942036-05-4

202 Franke, Jörg: *Einfluss der Überwachung auf die Versagenswahrscheinlichkeit von Staustufen,* 2011, ISBN 978-3-942036-06-1

203 Bakimchandra, Oinam: *Integrated Fuzzy-GIS approach for assessing regional soil erosion risks,* 2011, ISBN 978-3-942036-07-8

204 Alam, Muhammad Mahboob: *Statistical Downscaling of Extremes of Precipitation in Mesoscale Catchments from Different RCMs and Their Effects on Local Hydrology,* 2011, ISBN 978-3-942036-08-5

205 Hrsg.: Koschitzky, Hans-Peter; Braun, Jürgen: *VEGAS-Kolloquium 2011 Flache Geothermie - Perspektiven und Risiken,* Tagungsband zur Veranstaltung am 06. Oktober 2011 an der Universität Stuttgart, Campus Stuttgart-Vaihingen*,* 2011*,* ISBN 978-3-933761-09-2

206 Haslauer, Claus: *Analysis of Real-World Spatial Dependence of Subsurface Hydraulic Properties Using Copulas with a Focus on Solute Transport Behaviour,* 2011, ISBN 978-3-942036-10-8

207 Dung, Nguyen Viet: *Multi-objective automatic calibration of hydrodynamic models – development of the concept and an application in the Mekong Delta,* 2011, ISBN 978-3-942036-11-5

208 Hung, Nguyen Nghia: *Sediment dynamics in the floodplain of the Mekong Delta, Vietnam,* 2011, ISBN 978-3-942036-12-2

209 Kuhlmann, Anna: *Influence of soil structure and root water uptake on flow in the unsaturated zone,* 2012, ISBN 978-3-942036-13-9

210 Tuhtan, Jeffrey Andrew: *Including the Second Law Inequality in Aquatic Ecodynamics: A Modeling Approach for Alpine Rivers Impacted by Hydropeaking,* 2012, ISBN 978-3-942036-14-6

211 Tolossa, Habtamu: *Sediment Transport Computation Using a Data-Driven Adaptive Neuro-Fuzzy Modelling Approach,* 2012, ISBN 978-3-942036-15-3

212 Tatomir, Alexandru-Bodgan: *From Discrete to Continuum Concepts of Flow in Fractured Porous Media,* 2012, ISBN 978-3-942036-16-0

213 Erbertseder, Karin: *A Multi-Scale Model for Describing Cancer-Therapeutic Transport in the Human Lung,* 2012, ISBN 978-3-942036-17-7

214 Noack, Markus: *Modelling Approach for Interstitial Sediment Dynamics and Reproduction of Gravel Spawning Fish,* 2012, ISBN 978-3-942036-18-4

215 De Boer, Cjestmir Volkert: *Transport of Nano Sized Zero Valent Iron Colloids during Injection into the Subsurface*, 2012, ISBN 978-3-942036-19-1

216 Pfaff, Thomas: *Processing and Analysis of Weather Radar Data for Use in Hydrology*, 2013, ISBN 978-3-942036-20-7

217 Lebrenz, Hans-Henning: *Addressing the Input Uncertainty for Hydrological Modeling by a New Geostatistical Method*, 2013, ISBN 978-3-942036-21-4

218 Darcis, Melanie Yvonne: *Coupling Models of Different Complexity for the Simulation of CO_2 Storage in Deep Saline Aquifers*, 2013, ISBN 978-3-942036-22-1

219 Beck, Ferdinand: *Generation of Spatially Correlated Synthetic Rainfall Time Series in High Temporal Resolution - A Data Driven Approach*, 2013, ISBN 978-3-942036-23-8

220 Guthke, Philipp: *Non-multi-Gaussian spatial structures: Process-driven natural genesis, manifestation, modeling approaches, and influences on dependent processes*, 2013, ISBN 978-3-942036-24-5

221 Walter, Lena: *Uncertainty studies and risk assessment for CO_2 storage in geological formations*, 2013, ISBN 978-3-942036-25-2

222 Wolff, Markus: *Multi-scale modeling of two-phase flow in porous media including capillary pressure effects,* 2013, ISBN 978-3-942036-26-9

223 Mosthaf, Klaus Roland: *Modeling and analysis of coupled porous-medium and free flow with application to evaporation processes,* 2014, ISBN 978-3-942036-27-6

224 Leube, Philipp Christoph: *Methods for Physically-Based Model Reduction in Time: Analysis, Comparison of Methods and Application*, 2013, ISBN 978-3-942036-28-3

225 Rodríguez Fernández, Jhan Ignacio: *High Order Interactions among environmental variables: Diagnostics and initial steps towards modeling*, 2013, ISBN 978-3-942036-29-0

226 Eder, Maria Magdalena: *Climate Sensitivity of a Large Lake*, 2013, ISBN 978-3-942036-30-6

227 Greiner, Philipp: *Alkoholinjektion zur In-situ-Sanierung von CKW Schadensherden in Grundwasserleitern: Charakterisierung der relevanten Prozesse auf unterschiedlichen Skalen*, 2014, ISBN 978-3-942036-31-3

228 Lauser, Andreas: *Theory and Numerical Applications of Compositional Multi-Phase Flow in Porous Media*, 2014, ISBN 978-3-942036-32-0

229 Enzenhöfer, Rainer: *Risk Quantification and Management in Water Production and Supply Systems*, 2014, ISBN 978-3-942036-33-7

230 Faigle, Benjamin: *Adaptive modelling of compositional multi-phase flow with capillary pressure*, 2014, ISBN 978-3-942036-34-4

231 Oladyshkin, Sergey: *Efficient modeling of environmental systems in the face of complexity and uncertainty*, 2014, ISBN 978-3-942036-35-1

232 Sugimoto, Takayuki: *Copula based Stochastic Analysis of Discharge Time Series*, 2014, ISBN 978-3-942036-36-8

233 Koch, Jonas: *Simulation, Identification and Characterization of Contaminant Source Architectures in the Subsurface*, 2014, ISBN 978-3-942036-37-5

234 Zhang, Jin: *Investigations on Urban River Regulation and Ecological Rehabilitation Measures, Case of Shenzhen in China*, 2014, ISBN 978-3-942036-38-2

235 Siebel, Rüdiger: *Experimentelle Untersuchungen zur hydrodynamischen Belastung und Standsicherheit von Deckwerken an überströmbaren Erddämmen,* 2014, ISBN 978-3-942036-39-9

236 Baber, Katherina: *Coupling free flow and flow in porous media in biological and technical applications: From a simple to a complex interface description,* 2014, ISBN 978-3-942036-40-5

237 Nuske, Klaus Philipp: *Beyond Local Equilibrium — Relaxing local equilibrium assumptions in multiphase flow in porous media,* 2014, ISBN 978-3-942036-41-2

238 Geiges, Andreas: *Efficient concepts for optimal experimental design in nonlinear environmental systems*, 2014, ISBN 978-3-942036-42-9

239 Schwenck, Nicolas: *An XFEM-Based Model for Fluid Flow in Fractured Porous Media*, 2014, ISBN 978-3-942036-43-6

240 Chamorro Chávez, Alejandro: *Stochastic and hydrological modelling for climate change prediction in the Lima region, Peru*, 2015, ISBN 978-3-942036-44-3

241 Yulizar: *Investigation of Changes in Hydro-Meteorological Time Series Using a Depth-Based Approach*, 2015, ISBN 978-3-942036-45-0

242 Kretschmer, Nicole: *Impacts of the existing water allocation scheme on the Limarí watershed – Chile, an integrative approach*, 2015, ISBN 978-3-942036-46-7

243 Kramer, Matthias: *Luftbedarf von Freistrahlturbinen im Gegendruckbetrieb*, 2015, ISBN 978-3-942036-47-4

244 Hommel, Johannes: *Modeling biogeochemical and mass transport processes in the subsurface: Investigation of microbially induced calcite precipitation*, 2016, ISBN 978-3-942036-48-1

245 Germer, Kai: *Wasserinfiltration in die ungesättigte Zone eines makroporösen Hanges und deren Einfluss auf die Hangstabilität*, 2016, ISBN 978-3-942036-49-8

246 Hörning, Sebastian: *Process-oriented modeling of spatial random fields using copulas*, 2016, ISBN 978-3-942036-50-4

247 Jambhekar, Vishal: *Numerical modeling and analysis of evaporative salinization in a coupled free-flow porous-media system,* 2016, ISBN 978-3-942036-51-1

248 Huang, Yingchun: *Study on the spatial and temporal transferability of conceptual hydrological models*, 2016, ISBN 978-3-942036-52-8

249 Kleinknecht, Simon Matthias: *Migration and retention of a heavy NAPL vapor and remediation of the unsaturated zone*, 2016, ISBN 978-3-942036-53-5

250 Kwakye, Stephen Oppong: *Study on the effects of climate change on the hydrology of the West African sub-region*, 2016, ISBN 978-3-942036-54-2

251 Kissinger, Alexander: *Basin-Scale Site Screening and Investigation of Possible Impacts of CO_2 Storage on Subsurface Hydrosystems*, 2016, ISBN 978-3-942036-55-9

252 Müller, Thomas: *Generation of a Realistic Temporal Structure of Synthetic Precipitation Time Series for Sewer Applications*, 2017, ISBN 978-3-942036-56-6

253 Grüninger, Christoph: *Numerical Coupling of Navier-Stokes and Darcy Flow for Soil-Water Evaporation*, 2017, ISBN 978-3-942036-57-3

254 Suroso: *Asymmetric Dependence Based Spatial Copula Models: Empirical Investigations and Consequences on Precipitation Fields*, 2017, ISBN 978-3-942036-58-0

255 Müller, Thomas; Mosthaf, Tobias; Gunzenhauser, Sarah; Seidel, Jochen; Bárdossy, András: *Grundlagenbericht Niederschlags-Simulator (NiedSim3)*, 2017, ISBN 978-3-942036-59-7

256 Mosthaf, Tobias: *New Concepts for Regionalizing Temporal Distributions of Precipitation and for its Application in Spatial Rainfall Simulation,* 2017, ISBN 978-3-942036-60-3

257 Fenrich, Eva Katrin: *Entwicklung eines ökologisch-ökonomischen Vernetzungsmodells für Wasserkraftanlagen und Mehrzweckspeicher,* 2018, ISBN 978-3-942036-61-0

258 Schmidt, Holger: *Microbial stabilization of lotic fine sediments*, 2018, ISBN 978-3-942036-62-7

259 Fetzer, Thomas: *Coupled Free and Porous-Medium Flow Processes Affected by Turbulence and Roughness – Models, Concepts and Analysis*, 2018, ISBN 978-3-942036-63-4

260 Schröder, Hans Christoph: *Large-scale High Head Pico Hydropower Potential Assessment*, 2018, ISBN 978-3-942036-64-1

261 Bode, Felix: *Early-Warning Monitoring Systems for Improved Drinking Water Resource Protection*, 2018, ISBN 978-3-942036-65-8

262 Gebler, Tobias: *Statistische Auswertung von simulierten Talsperrenüberwachungsdaten zur Identifikation von Schadensprozessen an Gewichtsstaumauern*, 2018, ISBN 978-3-942036-66-5

263 Harten, Matthias von: *Analyse des Zuppinger-Wasserrades – Hydraulische Optimierungen unter Berücksichtigung ökologischer Aspekte*, 2018, ISBN 978-3-942036-67-2

264 Yan, Jieru: *Nonlinear estimation of short time precipitation using weather radar and surface observations*, 2018, ISBN 978-3-942036-68-9

265 Beck, Martin: *Conceptual approaches for the analysis of coupled hydraulic and geomechanical processes*, 2019, ISBN 978-3-942036-69-6

266 Haas, Jannik: *Optimal planning of hydropower and energy storage technologies for fully renewable power systems*, 2019, ISBN 978-3-942036-70-2

267 Schneider, Martin: *Nonlinear Finite Volume Schemes for Complex Flow Processes and Challenging Grids*, 2019, ISBN 978-3-942036-71-9

268 Most, Sebastian Christopher: *Analysis and Simulation of Anomalous Transport in Porous Media*, 2019, ISBN 978-3-942036-72-6

269 Buchta, Rocco: *Entwicklung eines Ziel- und Bewertungssystems zur Schaffung nachhaltiger naturnaher Strukturen in großen sandgeprägten Flüssen des norddeutschen Tieflandes*, 2019, ISBN 978-3-942036-73-3

270 Thom, Moritz: *Towards a Better Understanding of the Biostabilization Mechanisms of Sediment Beds*, 2019, ISBN 978-3-942036-74-0

271 Stolz, Daniel: *Die Nullspannungstemperatur in Gewichtsstaumauern unter Berücksichtigung der Festigkeitsentwicklung des Betons*, 2019, ISBN 978-3-942036-75-7

272 Rodriguez Pretelin, Abelardo: *Integrating transient flow conditions into groundwater well protection*, 2020, ISBN: 978-3-942036-76-4

273 Weishaupt, Kilian: *Model Concepts for Coupling Free Flow with Porous Medium Flow at the Pore-Network Scale: From Single-Phase Flow to Compositional Non-Isothermal Two-Phase Flow*, 2020, ISBN: 978-3-942036-77-1

274 Koch, Timo: *Mixed-dimension models for flow and transport processes in porous media with embedded tubular network systems*, 2020, ISBN: 978-3-942036-78-8

275 Gläser, Dennis: *Discrete fracture modeling of multi-phase flow and deformation in fractured poroelastic media*, 2020, ISBN: 978-3-942036-79-5

276 Seitz, Lydia: *Development of new methods to apply a multi-parameter approach – A first step towards the determination of colmation*, 2020, ISBN: 978-3-942036-80-1

277 Ebrahim Bakhshipour, Amin: *Optimizing hybrid decentralized systems for sustainable ur-ban drainage infrastructures planning*, 2021, ISBN: 978-3-942036-81-8

278 Seitz, Gabriele: *Modeling Fixed-Bed Reactors for Thermochemical Heat Storage with the Reaction System CaO/Ca(OH)$_2$*, 2021, ISBN: 978-3-942036-82-5

279 Emmert, Simon: *Developing and Calibrating a Numerical Model for Microbially Enhanced Coal-Bed Methane Production*, 2021, ISBN: 978-3-942036-83-2

280 Heck, Katharina Klara: *Modelling and analysis of multicomponent transport at the interface between free- and porous-medium flow - influenced by radiation and roughness*, 2021, ISBN: 978-3-942036-84-9

281 Ackermann, Sina: *A multi-scale approach for drop/porous-medium interaction*, 2021, ISBN: 978-3-942036-85-6

282 Beckers, Felix: *Investigations on Functional Relationships between Cohesive Sediment Erosion and Sediment Characteristics*, 2021, ISBN: 978-3-942036-86-3

283 Schlabing, Dirk: *Generating Weather for Climate Impact Assessment on Lakes*, 2021, ISBN: 978-3-942036-87-0

284 Becker, Beatrix: *Efficient multiscale multiphysics models accounting for reversible flow at various subsurface energy storage sites*, 2021, ISBN: 978-3-942036-88-7

285 Reuschen, Sebastian: *Bayesian Inversion and Model Selection of Heterogeneities in Geo-statistical Subsurface Modeling*, 2021, ISBN: 978-3-942036-89-4

286 Michalkowski, Cynthia: *Modeling water transport at the interface between porous GDL and gas distributor of a PEM fuel cell cathode*, 2022, ISBN: 978-3-942036-90-0

287 Koca, Kaan: *Advanced experimental methods for investigating flow-biofilm-sediment interactions*, 2022, ISBN: 978-3-942036-91-7

288 Modiri, Ehsan: *Clustering simultaneous occurrences of extreme floods in the Neckar catchment*, 2022, ISBN: 978-3-942036-92-4

289 Mayar, Mohammad Assem: *High-resolution spatio-temporal measurements of the colmation phenomenon under laboratory conditions*, 2022, ISBN: 978-3-942036-93-1

290 Schäfer Rodrigues Silva, Aline: *Quantifying and Visualizing Model Similarities for Multi-Model Methods*, 2022, ISBN: 978-3-942036-94-8

291 Moreno Leiva, Simón: *Optimal planning of water and renewable energy systems for copper production processes with sector coupling and demand flexibility*, 2022, ISBN 978-3-942036-95-5

292 Schönau, Steffen: *Modellierung von Bodenerosion und Sedimentaustrag bei Hochwasserereignissen am Beispiel des Einzugsgebiets der Rems*, 2022, ISBN 978-3-942036-96-2

293 Glatz, Kumiko: *Upscaling of Nanoparticle Transport in Porous Media,* 2022, ISBN 978-3-942036-97-9

294 Pavía Santolamazza, Daniela: *Event-based flood estimation using a random forest algorithm for the regionalization in small catchments*, 2022, ISBN 978-3-942036-98-6

295 Haun, Stefan: *Advanced Methods for a Sustainable Sediment Management of Reservoirs*, 2022, ISBN 978-3-942036-99-3

296 Herma, Felix: *Data Processing and Model Choice for Flood Prediction*, 2022, ISBN 978-3-910293-00-7

297 Weinhardt, Felix: *Porosity and permeability alterations in processes of biomineralization in porous media - microfluidic investigations and their interpretation*, 2022, ISBN 978-3-910293-01-4

Die Mitteilungshefte ab der Nr. 134 (Jg. 2005) stehen als pdf-Datei über die Homepage des Instituts: www.iws.uni-stuttgart.de zur Verfügung.